



## **SeaWiFS Postlaunch Technical Report Series**

Stanford B. Hooker, Editor  
*Goddard Space Flight Center, Greenbelt, Maryland*

Elaine R. Firestone, Senior Technical Editor  
*SAIC General Sciences Corporation, Laurel, Maryland*

## **Volume 1, The SeaWiFS Transfer Radiometer (SXR)**

B. Carol Johnson  
J.B. Fowler  
*National Institute of Standards and Technology, Gaithersburg, Maryland*

Christopher L. Cromer  
*National Institute of Standards and Technology, Boulder, Colorado*

National Aeronautics and  
Space Administration

**Goddard Space Flight Center**  
Greenbelt, Maryland 20771

---

**Available from:**

**NASA Center for AeroSpace Information**  
7121 Standard Drive  
Hanover, MD 21076-1320  
Price Code: A17

**National Technical Information Service**  
5285 Port Royal Road  
Springfield, VA 22161  
Price Code: A10

PREFACE

From the inception of the SeaWiFS Project, there has been a commitment to documenting the work undertaken by the Project. This philosophy was driven by a number of considerations including the needs to:

- 1) Inform the science community of the wide variety of technical issues that must be addressed in deriving science quality products from satellite measurements,
- 2) Provide to NASA management tangible evidence of the work being undertaken and a reasonable justification for the level of effort being requested,
- 3) Consolidate into a single document series a reference set that includes most of the relevant information related to satellite ocean color remote sensing, and
- 4) Ensure that the SeaWiFS data set can be easily understood by future researchers long after the SeaWiFS mission is over.

To my knowledge, no other NASA project has exerted as much effort as the SeaWiFS Project has in providing such information to its constituency. Indeed, the (Prelaunch) *SeaWiFS Technical Report Series* of 43 volumes required much effort, diligence, and patience, but I believe the series has served the community well and that the time and energy exerted were worth the effort. Indeed, were it not for these technical reports, little of the information would be available, as much would be judged inappropriate for peer-reviewed journals. I want to congratulate all those who contributed to the series as I believe the series will stand as a hallmark in Earth remote sensing.

At this time, SeaWiFS has been operational for over a year. During this time, the Project has continued to refine its capabilities and has undertaken two complete reprocessings in February and August 1998. Simultaneously, the SeaWiFS staff and our collaborators have continued to document their work as the Project has determined to initiate the so-called *Postlaunch Series*. This volume on the SeaWiFS Transfer Radiometer (SXR) is the first in the series. Several other volumes are already near completion including descriptions of the fifth Atlantic Meridional Transect (AMT-5) cruise, the final analysis of the prelaunch SeaWiFS recalibration data collected in early 1997, and the results for the fifth SeaWiFS Intercalibration Round-Robin Experiment (SIRREX-5).

The SXR development was undertaken early in the SeaWiFS program to facilitate the calibration round-robin activity (Mueller 1993, Mueller et al. 1994 and 1996, and Johnson et al. 1996—Volumes 14, 16, 34, and 37, respectively, of the Prelaunch Series). The SXR has been used in SIRREX-3, -4, and -5, in an examination of the sphere used for the prelaunch calibration of the OCTS (Johnson, et al. 1997), for the recalibration of the GSFC sphere (Yeh et al. 1997) and in the SeaWiFS prelaunch recalibration. The SXR also served as a prototype for similar transfer radiometers designed for other EOS instruments. As a result of the success of the SXR development and its use in subsequent experiments, a second generation SXR is being built for the SIMBIOS Project which is continuing the ocean color calibration round robin.

Greenbelt, Maryland  
August 1998

—C.R. McClain  
SeaWiFS Project Manager



## ABSTRACT

The SeaWiFS Transfer Radiometer (SXR) was built for the Sea-viewing Wide Field-of-view Sensor (SeaWiFS) Project as part of an Interagency Agreement with the National Aeronautics and Space Administration (NASA). The SXR is a multichannel radiometer designed to verify and compare measurements of spectral radiance at six discrete wavelengths in the visible and near infrared for various calibration sources in the SeaWiFS Project. In addition, the SXR is used to compare these sources to standards of spectral radiance maintained at the National Institute of Standards and Technology (NIST). The SXR was designed, built, and thoroughly characterized in the Optical Technology Division at NIST. A unique optical design provides six independent optical paths, each equipped with a temperature stabilized interference filter and silicon photodiode. A separate beam path through the input lens is used to visually align the SXR. The entrance windows for each channel overlap at the source, with each channel sampling a unique solid angle within the field of view of the SXR; this allows for simultaneous sampling of all channels. The combined standard relative uncertainty of spectral radiance measurements with the SXR is estimated to be between 0.6% and 1.3%. This report describes the design and construction of the SXR in detail, and gives the results of the optical characterization and calibrations done at NIST. The SXR has been used for several intercomparisons which include several SeaWiFS Intercalibration Round-Robin Experiments (SIRREXs); those done at the Marine Optical Buoy (MOBY) laboratories in Honolulu, Hawaii; at the NEC Corporation in Yokohama, Japan; and Orbital Sciences Corporation (OSC) in Germantown, Maryland. Thorough optical characterization and calibration of the SXR was essential to the successful application of the radiometer for these measurements.

## 1. INTRODUCTION

The SeaWiFS Transfer Radiometer (SXR) was designed and built by the Optical Technology Division at the National Institute of Standards and Technology (NIST) as part of an Interagency Agreement with the Sea-viewing Wide Field-of-view Sensor (SeaWiFS) Project Office at the National Aeronautics and Space Administration's (NASA) Goddard Space Flight Center (GSFC). SeaWiFS is a radiometer used for determining pigment concentrations in the oceans; these data will be used to improve the understanding of the carbon cycle and biogeochemistry (Hooker et al. 1993).

The SeaWiFS instrument was characterized and calibrated by the manufacturer (Barnes et al. 1994); with the launch of SeaWiFS, the radiometric measurements are being assessed, monitored, and verified using solar and lunar observations, as well as being compared to *in situ* optical measurements of the ocean and atmosphere. Ocean color scientists estimate that SeaWiFS must determine the water-leaving radiance with a relative standard uncertainty of 5% to satisfy the scientific goals of the mission (Mueller and Austin 1995). In order to provide useful information on the performance of the satellite, the field measurements of water-leaving radiance should result in a relative standard uncertainty of about 1%.

These challenging *in situ* measurements will be acquired with various field instruments over the five-year mission interval. Because of this, it was clear that a measurement assurance program was required. This program consists of several elements: clearly defined protocols (Mueller and

Austin 1992 and 1995); annual intercomparison and training exercises (Mueller 1993, Mueller et al. 1994, Mueller et al. 1996, and Johnson et al. 1996); direct comparison to a national standard laboratory (hence the SXR); and a portable field source, called the SeaWiFS Quality Monitor (SQM), for monitoring the temporal stability of the calibration of field instruments (Johnson et al. 1998). This report documents the SXR in detail—its design, calibration, characterization, uncertainties, conclusions, and recommendations.

### 1.1 General Description

The SXR is a multichannel imaging radiometer which uses interference filters for spectral selection. The radiometer is portable, stable, and provides a detector-based verification of the spectral radiance of integrating sphere sources and illuminated diffuse plaques at six wavelengths from 412–775 nm. Custom electronic circuits are used to provide a direct current (DC) voltage that is related to the spectral radiance of the source according to the measurement equation (Sect. 3); remote control of the channel (i.e., measurement wavelength) and gain using digital logic is possible.

The requirements for the SXR were finalized during the First SeaWiFS Intercalibration Round-Robin Experiment (SIRREX-1) (Mueller 1993). It was decided at that time to compare the predicted voltage from the SXR for a given source of spectral radiance, which can be calculated from the known spectral radiance of the source and the spectral radiance responsivity of the SXR, to that measured by the

**Table 1.** SXR design specifications. The given wavelengths for the radiances are in nanometers and the initial specifications for the spectral radiances were based on the radiance of a diffuse plaque illuminated by a typical standard irradiance lamp (Mueller and Austin 1992).

Quantity	Initial Specification	Final Value
$L(410)$	$0.6 \mu\text{W cm}^{-2} \text{sr}^{-1} \text{nm}^{-1}$	$\leq 10 \mu\text{W cm}^{-2} \text{sr}^{-1} \text{nm}^{-1}$
$L(488)$	$1.5 \mu\text{W cm}^{-2} \text{sr}^{-1} \text{nm}^{-1}$	$\leq 48 \mu\text{W cm}^{-2} \text{sr}^{-1} \text{nm}^{-1}$
$L(665)$	$4.5 \mu\text{W cm}^{-2} \text{sr}^{-1} \text{nm}^{-1}$	$\leq 46 \mu\text{W cm}^{-2} \text{sr}^{-1} \text{nm}^{-1}$
Spectral Coverage	400–900 nm	411–775 nm (6 bands)
Spectral Bandpass	$\approx 10$ nm	10–12 nm
Field of View	$< 5^\circ$	$2.4^\circ$
Object Distance	1 m to infinity	85 cm to infinity
Noise-Equivalent Radiance	$\approx 0.3 \text{ nW cm}^{-2} \text{sr}^{-1} \text{nm}^{-1}$	$1.1 \text{ nW cm}^{-2} \text{sr}^{-1} \text{nm}^{-1}$ at 410 nm
Dynamic Range	$\approx 5,000$	10,000
Out of Band	$< 0.01\%$ of the total	$< 0.4\%$ of the total
Absolute Calibration	0.99	$> 0.987$ (GSFC sphere, 16 lamps)
Long Term Stability	$\leq 1\%$	0.3%
Polarization Sensitivity	$< 1\%$	Not Measured

SXR. Because the spectral radiance of the source would be determined from independent measurements (which may be traceable to NIST), this type of comparison should agree within the combined uncertainties assigned to the SXR and the source. Thus, the SXR was designed to verify the spectral radiance of the calibration sources which are used in the Project. In most cases, however, the SXR has been used to measure the spectral radiance of a source, because the results in this mode of operation are sufficiently accurate. The initial specifications consisted of a list of parameters corresponding to an optical performance that matched the types of sources to be studied. As is shown, the measured performance satisfies these initial requirements, although the sensitivity to polarization was not measured (Table 1).

The unique optical design of the SXR provides six optical paths, each equipped with an interference filter and a silicon photodiode detector. A separate optical path through the input lens is used for aligning and focusing the SXR. Each of these optical paths measures or views the same area on the source, but the solid angle is sampled differently. This design will produce good results for sources that are spatially uniform and lambertian. The convenient feature of the design is that all channels are sampled without moving a mechanical component, such as a filter wheel. The disadvantage of the design is that the throughput for any single channel is decreased compared to what would result if a single on-axis scheme was used.

## 1.2 General Approach

A mathematical relationship, known as the “measurement equation,” is used to describe the relationship between the radiant flux through the entrance pupil of the radiometer and the voltage generated by the electronics (Kostkowski and Nicodemus 1978). In particular, the measurement equation describes how the radiometer responds

to radiant flux as a function of time, state of polarization, wavelength, spatial and angular coordinates, and the magnitude of the radiant flux (Nicodemus 1978 and Wyatt 1978).

It is usually assumed that the total response function can be written as a product of individual, independent functions which greatly simplifies the characterization and calibration of the radiometer, and this approach was followed for the SXR. This assumption, however, may not be true for any number of reasons; a common example is the effect of scattered light.

The SXR was characterized for relative spectral response using the NIST Spectral Comparator Facility (Larson et al. 1996), for field-of-view response using a small lamp mounted on a dual-axis translation stage, and linearity of response with respect to incident flux using the NIST beamcombiner (Thompson and Chen 1994). No measurements were made of the temporal response (in the sense of using a pulsed input), but information was obtained on the short and long term stability of the SXR. No measurements were made of the polarization response of the SXR, as it will always compare sources that should have negligible or at least similar, polarization.

To determine the SXR's absolute spectral radiance responsivity, the SXR was used to measure a sphere source calibrated at the Facility for Automated Spectroradiometric Calibrations (FASCAL) (Walker et al. 1987a). The SXR measurement wavelengths, calibration factors, and uncertainties for the calibration factors are given in Table 2.

## 2. INSTRUMENT DESIGN

The SXR is approximately 160 mm in diameter and 300 mm in length (Fig. 1). The instrument mounts to a standard tripod stand with a 1/4-20 Unified Coarse (UNC)

**Table 2.** The SXR measurement wavelength,  $\lambda_m$ ; the calibration coefficient,  $\langle D_{cs} \rangle$  (for unity gain on the SXR amplifier); and the relative standard uncertainty,  $u_D$ , for  $\langle D_{cs} \rangle$  are given here. The calibration coefficient is negative because the output voltage from the SXR is negative for measurements of optical sources if the bayonet nut connector (BNC) cable is connected with the ground shield to the common input of the DMM.

Channel	$\lambda_m$ [nm]	$\langle D_{cs} \rangle$ [V cm <sup>2</sup> sr nm $\mu$ W <sup>-1</sup> ]	$u_D$ [%]
1	411.222	-1.101185	0.88
2	441.495	-1.468061	1.12
3	486.938	-0.2442614	0.54
4	547.873	-0.2425734	0.63
5	661.718	-0.2604715	0.49
6	774.767	-0.03013285	0.64

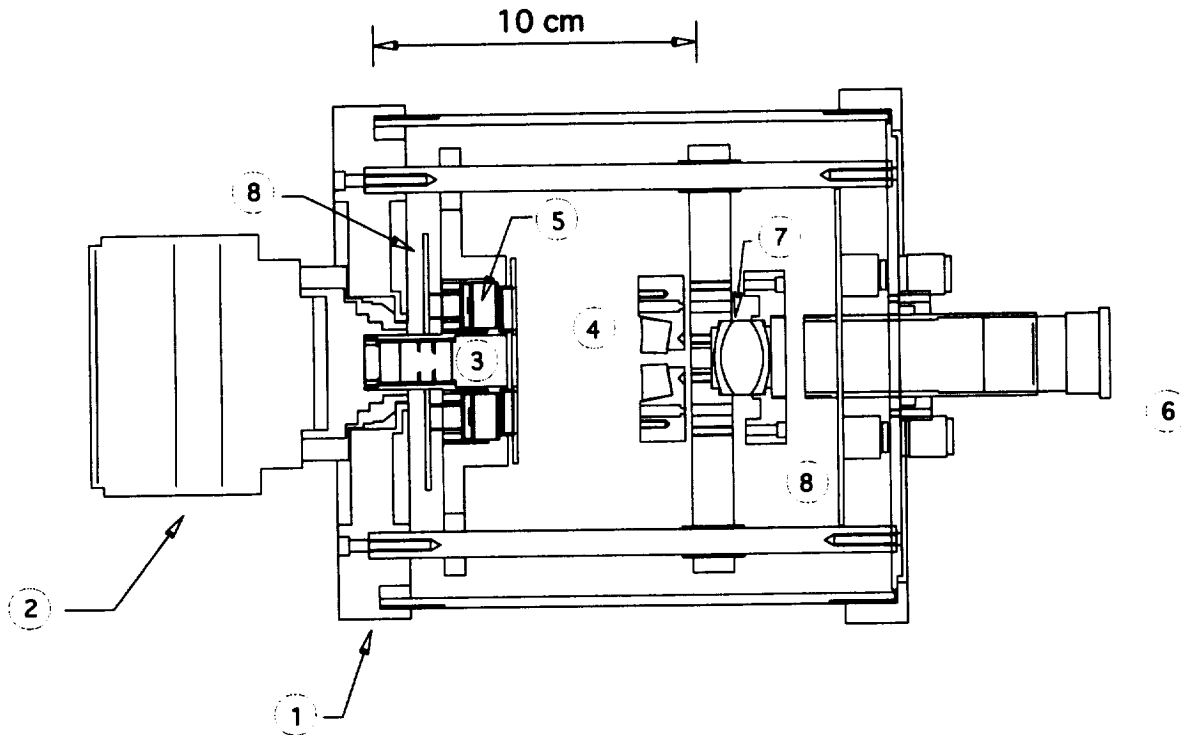


**Fig. 1.** Cut away schematic of the SXR includes the 1) mounting point for the tripod; 2) 85 mm focal length objective lens; 3) precision field stop aperture; 4) six, wedge-shaped fold mirrors; 5) six interference filter and detector assemblies; 6) optical alignment eyepiece; 7) optical alignment relay lens; 8) circuit boards.

thread; there are four equally spaced mounting orientations that rotate the SXR about the optical axis. A power supply, temperature controller, digital multimeter (DMM), computer, and a working draft of the user manual accompany the radiometer for field work. The interference filters, detectors, and the precision aperture (which functions as the field stop) are maintained at 26°C using thermoelectric cooler (TEC) elements powered by the temperature control unit. The optical, mechanical, electrical, and thermal sub-

systems are described below, followed by a brief summary of the data acquisition protocols and requirements.

## 2.1 Optical

The optical path for each measurement channel consists of the objective lens; the field stop; an off-axis, wedged-shaped section of a spherical mirror; an interference filter; and a silicon photodiode detector. There is an aperture

stop, but as described below, it is not located in the ideal location, and this causes vignetting within the field of view. The optical path for the alignment of the SXR consists of the objective lens, the field stop, a relay lens, and an eyepiece.

### 2.1.1 Measurement Channels

Radiant flux is imaged from the source onto six separate silicon photodiode detectors, using an objective lens to form an intermediate image at the field stop, and six separate wedge-shaped sections of a spherical mirror to image the field stop onto the active area of the detectors. The mirror sections each sample a different portion of the solid angle of the flux transmitted by the field stop. The center of curvature for each mirror section is displaced radially from the mechanical axis of the SXR by rotating the mirror wedges, so that the six images of the field stop are equally spaced on a circle, 32 mm in diameter. Different interference filters are placed in front of each detector to define the measurement wavelengths of the SXR.

Sources at different distances from the SXR can be imaged onto the detectors by focusing the objective lens, which is a Nikkor 85 mm  $f/1.4$  camera lens (Nikon model number 1450).<sup>†</sup> When the lens is focused on an object at infinity, the back principal plane is separated from the field stop by 85 mm. When the lens is focused on an object at the minimum distance of 85 cm, the components of the lens are translated along the optical axis so that the back principal plane is 94.44 mm from the field stop.

The aperture ratio of the lens,  $f/1.4$ , refers to the position of the lens components at a focus of infinity; at the minimum focus, the aperture ratio is  $f/1.54$ , because the lens is displaced from the field stop (image plane) by 9.44 mm. If the aperture stop contained in the objective lens was used to control the aperture ratio, the radiance responsivity of the SXR would decrease by as much as 83% when used with sources at the minimum distance instead of sources farther away. An aperture behind the objective lens and before the field stop was designed to be the limiting aperture stop, with an effective aperture ratio that is slower than  $f/1.54$ , so the radiance responsivity of the SXR would be independent of the distance between the source and the SXR.

Projected ray traces of one measurement channel are shown in two orthogonal views in Fig. 2, and the critical components are identified. The nickel-copper electroformed field stop aperture has an inside diameter (ID) of 3.5682 mm (area of  $0.1 \text{ cm}^2$ ) and an edge thickness of 0.2 mm (Buckbee-Mears model number SK-030483-1072).

<sup>†</sup> Certain commercial equipment, instruments, or materials are identified in this technical memorandum to foster understanding. Such identification does not imply recommendation or endorsement by NASA or NIST, nor does it imply that the materials or equipment identified are necessarily the best available for the purpose.

The wedge-shaped spherical mirror sections were made by drilling a tapered hole in the center of a plano-concave spherical mirror blank with a 50 mm radius of curvature and a diameter of 25.4 mm (Virgo Optics part number 13100) and then cutting the mirror into six equal wedges ( $60^\circ$  sections). After beveling the sides of the mirror sections, they were coated with aluminum. A single layer silicon dioxide overcoat was also applied.

The mirror sections image the field stop with slight demagnification (0.75 neglecting aberrations), and can be individually rotated and translated (hence the bevels and taper) so that each channel is aligned and focused on the detector assemblies. Each of these assemblies consists of an additional  $0.1 \text{ cm}^2$  area electroformed aperture; a multilayer interference filter made using the technique of ion-assisted beam deposition (IAD), for enhanced stability and lifetime, from Barr Associates; and a Hamamatsu silicon photodiode. The common specifications for the interference filters include the diameter (14 mm), the maximum thickness (7 mm), and the out-of-band spectral transmittance ( $10^{-6}$  from 200–1,200 nm). The individual specifications included the center wavelength, the full-width at half-maximum transmittance, and a minimum value for the maximum transmittance. The silicon photodiodes have a square active area of 5.8 mm on a side. A Hamamatsu (model number S1337-66BQ) photodiode was used for the channel at 775 nm and the S1227-66BQ photodiode was used for the other five channels.

An earlier design of the SXR, which was the configuration used at SIRREX-2 (Mueller et al. 1994), used an electroformed aperture,  $0.5 \text{ cm}^2$  in area, located 22 mm in front of the field stop (equivalent to  $f/2.8$ ). It was later determined that the cylindrical tube used to mount this aperture was imaging flux from an annular region, well outside the geometric field of view, onto the detectors via a single reflection from the inside of the cylindrical tube. Rather than completely disassemble the SXR and modify the mechanical components, a set of baffles was designed according to the procedures outlined in Wyatt (1987). The baffles solved the scattered light problem, and resulted in the front of the cylindrical tube acting as the aperture stop for the objective lens and the field stop for the system, resulting in an increased throughput (about  $f/2.5$ ).

Much later, after thorough testing of the point-spread response of the SXR (Sect. 3.2.3) and more consideration of the ray traces, two things were clear:

- a) The wedge mirrors were functioning as the aperture stop for most rays and it was a design error to consider an aperture between the objective lens and the field stop as the aperture stop; and
- b) The front of the cylindrical tube caused vignetting.

Because the mirror elements are wedge-shaped and off-axis, it is not possible to describe a measurement channel of the SXR in terms of a single marginal and chief ray (O'Shea 1985).



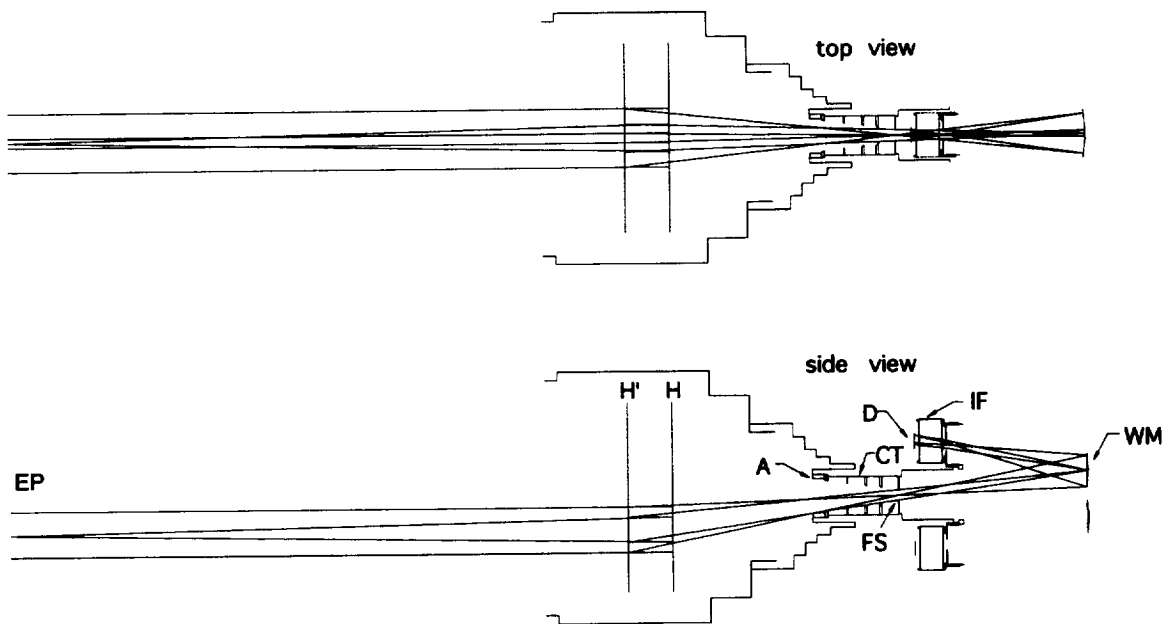


**Fig. 2a.** Tracings for marginal and chief rays for an SXR measurement channel plus the critical optical components: EP is the entrance pupil; H and H' are the front and back principal planes of the objective lens, respectively; CT is the cylindrical tube; FS is the field stop; WM is the spherical mirror wedge section; A is the aperture at the end of the CT; IF is the interference filter; and D is the detector. The side view projection shows the plane that bisects the mirror wedge in the center, and is perpendicular to the axis of rotation of the mirror wedge. The top view is orthogonal to the side view, with the detector and filter assembly shown dashed; only rays that strike one of the mirrors are shown. The principal planes of the objective lens are indicated by the fine dashed line.

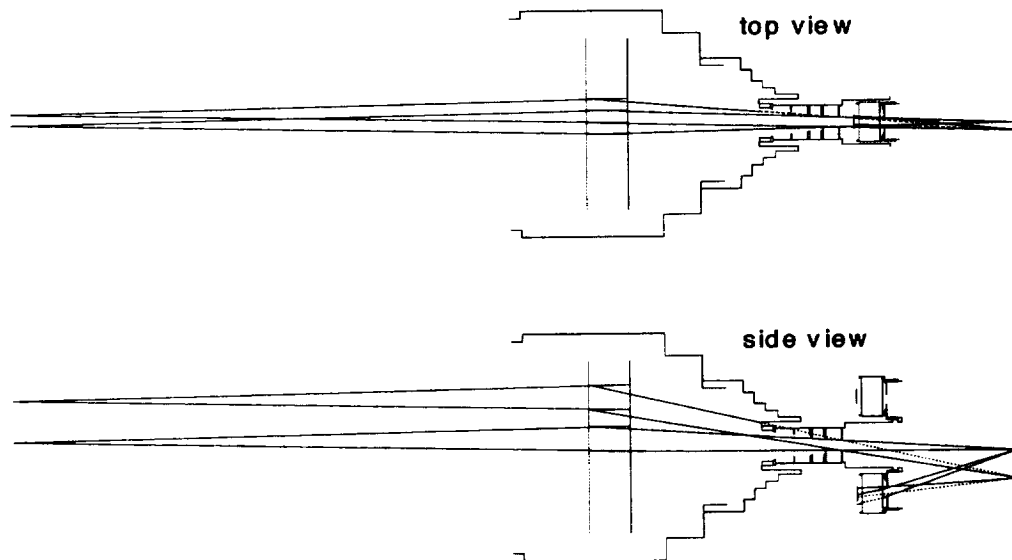


**Fig. 2b.** Tracings for extreme rays for an SXR measurement channel. The side and top views are as in Fig. 2a, as are the dashed lines.

The aperture stop is identified by tracing rays that come from the center of the source and increasing the slope of the ray until it is obscured by the edge of an optic or baffle. Often, there is azimuthal symmetry, but this is not the case for the SXR. For a particular measurement channel, these marginal rays encounter the inner or outer edge of the mirror, the sides of the mirror, and in some cases, the threaded retaining ring at the front of the cylindrical tube. These marginal rays are indicated in Fig. 2a for the situation where the focus is at infinity; these are the rays with zero slope between the entrance pupil and the front principal plane. Rays that pass through the center of the aperture stop and the edge of the field stop determine the geometric field of view of the SXR. These chief rays are also shown in Fig. 2a.

The image of the aperture stop, as viewed from object space, defines the entrance pupil, which is the effective aperture on any radiometer that must be filled during radiometric characterization, calibration, and measurement. The geometric area on the source measured by the radiometer is subtended by the solid angle field of view from the entrance pupil. The entrance pupil indicated in Fig. 2a is based on the wedge mirror as the aperture stop, neglecting the small obstruction caused by the cylindrical tube. All ray traces were determined by treating the objective as an ideal lens (described by the location of the principal planes) and using Beam 4 (commercial software from Stellar Software). The interference filter was modeled as a lens with plane surfaces and an index of refraction of 1.47. The placement of the wedge mirror was determined by the optimization feature in Beam 4 using a subset of possible rays.

Figure 2b indicates rays that originate at specific edges of the entrance pupil. The projections indicate four extreme rays for one measurement channel. Two rays are indicated for each location in the entrance pupil; these rays intercept opposite edges of the field stop. Rays are shown dashed after striking the obscuration of the cylindrical tube or the secondary electroformed aperture which is just in front of the interference filter. Based on the extreme rays shown in the side view projection, the response of the SXR should be uniform for point sources located within the entrance window and below the optical axis, with a decreased response for point sources that are within the entrance window and above the optical axis. The vignetting function should behave as the intersection of a circle and a 60° wedge. Actual measurements of the point-spread response of the SXR are reported in Sect. 3.2.3.

### 2.1.2 Alignment Channel

The optical elements for the alignment optical path are shown in Fig. 3. A Steinheil achromatic triplet relay lens (40 mm focal length, Melles Griot part number 01 LAT 007/078) reimages the field stop with slight demagnification (approximately 0.84) at the front focal plane of

a Ramsden eyepiece (Melles Griot part number 04 ERA 002). The eyepiece, which has a focal length of 25 mm and a power of 10, generates an image at infinity so the field stop can be viewed by a human observer. The SXR is aligned by illuminating the instrument in the near field with a bright source (a flashlight is sufficient) so that the field stop is well defined. The eyepiece is adjusted until the edges of the field stop are in focus. Then, the SXR is focused on the desired target by viewing the field stop through the eyepiece and adjusting the focus of the objective lens until the target is also in focus.

## 2.2 Mechanical

The SXR was designed using a modular approach to facilitate assembly, optical alignment, and repair. Computer software (AutoCAD, a product of Autodesk) was used for generating the engineering drawings, and in many cases the files were transferred directly to the computers that control automated milling machines in the NIST Fabrication Division. This resulted in fast and accurate production of the various parts. Four mechanical subassemblies were used; these were attached to four precision-ground, steel support rods that serve as the structural frame for the SXR.

The complete assembly drawing is shown in Fig. 4.† Figure 5 details the switches and connectors used for control and data acquisition of the SXR. The detector plate assembly (DPA), Fig. 6, is attached to the rest of the unit in a fashion that allows the temperature to be maintained at a value above or below ambient. The field stop, interference filters, and silicon detectors are contained in the DPA. The ambient temperature plate assembly (ATA) serves as the baseplate for the SXR. The support rods are mounted to the ATA, as is the objective lens and the DPA. The amplifier circuit board, which converts photocurrent to voltage using six independent amplifiers, is mounted between the DPA and the ATA. The ATA is shown in Fig. 7 along with the DPA.

The mirror mount assembly (MMA) and the back plate assembly (BPA) are shown in Fig. 8. The MMA holds the six wedge-shaped mirrors and the relay lens, and it can be translated along the optical axis during initial alignment. The BPA holds the control circuit board, the eyepiece, and the electrical connections to the SXR. The SXR was assembled by completing the subassemblies and then attaching the amplifier circuit board to the DPA, the support rods to the ATA, and then the DPA and MMA to the support rods. Then, the control circuit board was attached to the back plate and the BPA was attached to the support rods.

† Notations, such as "6-32×12 mm" in reference to fasteners in the figure captions and elsewhere in the text, refer to the diameter, the number of threads per inch and the overall length. Notations, such as "6-32" or "M15×1" designates screw threads; here, the second example is metric and has a nominal diameter of 15 mm with a thread spacing (pitch) of 1 mm.

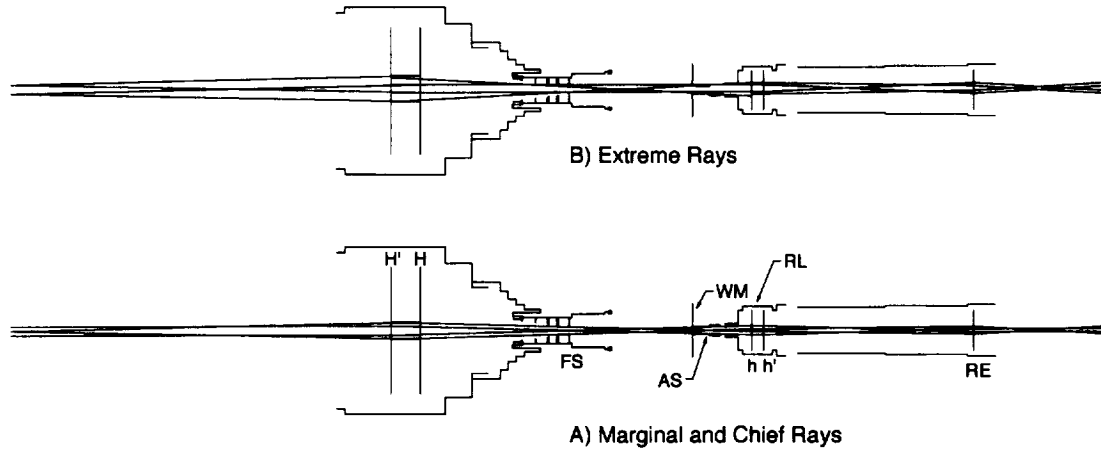


**Fig. 3.** Tracings for the a) marginal and chief rays, and b) extreme rays along with critical optical components for the SXR alignment channel:  $h$  is the front principal plane of the relay lens (RL),  $h'$  is the back principal plane of the RL, and RE is the Ramsden eyepiece (the other symbols are as in Fig. 2.)

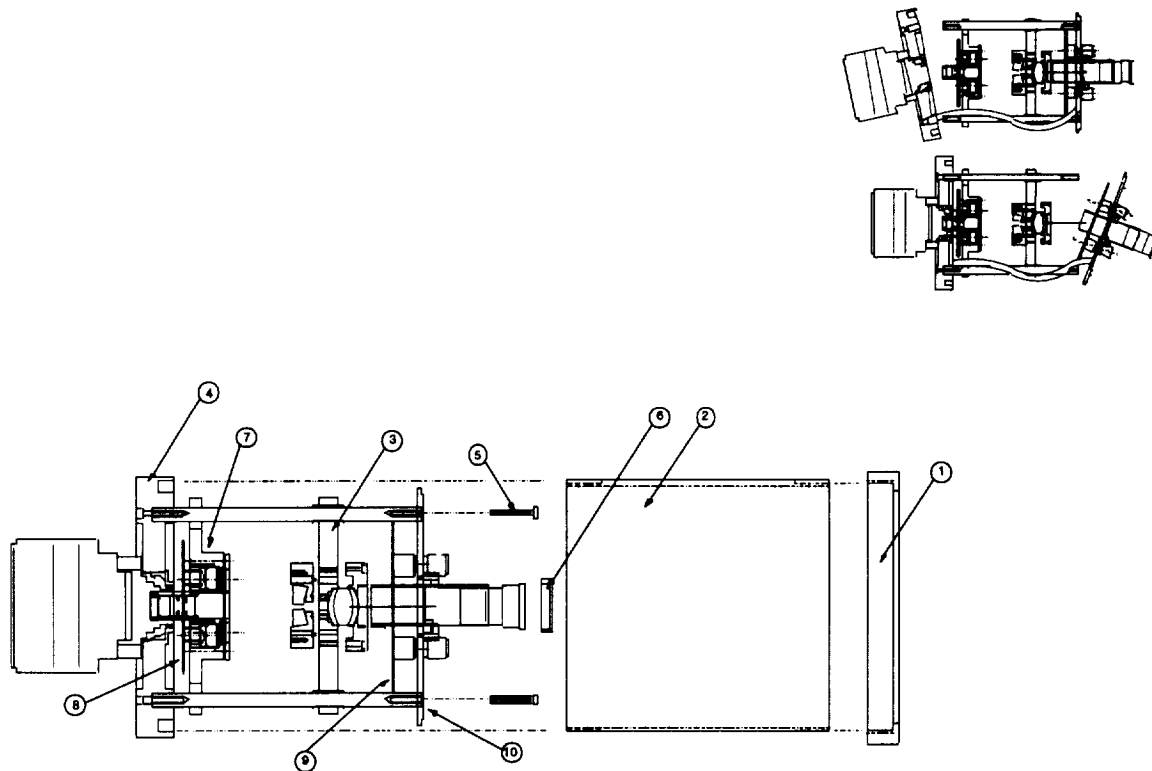


**Fig. 4.** Engineering assembly drawing of the SXR. The parts labeled 1–10 correspond to the 1) outer housing end cap, 2) outer housing, 3) mirror mount assembly, 4) ambient temperature plate assembly, 5) 6-32×12 mm fasteners, 6) eyepiece cap, 7) detector plate assembly, 8) amplifier circuit board, 9) control circuit board, and 10) back plate assembly. The insert (upper right) demonstrates how the unit can be opened while maintaining electrical continuity.

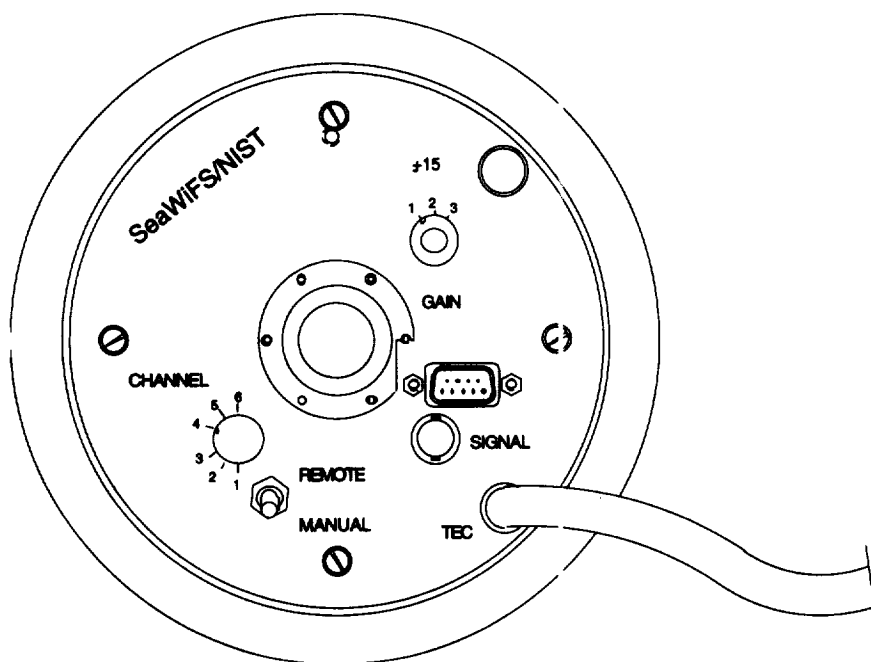


**Fig. 5.** A rear view of the SXR showing the switches and cable connectors used for control and data acquisition.

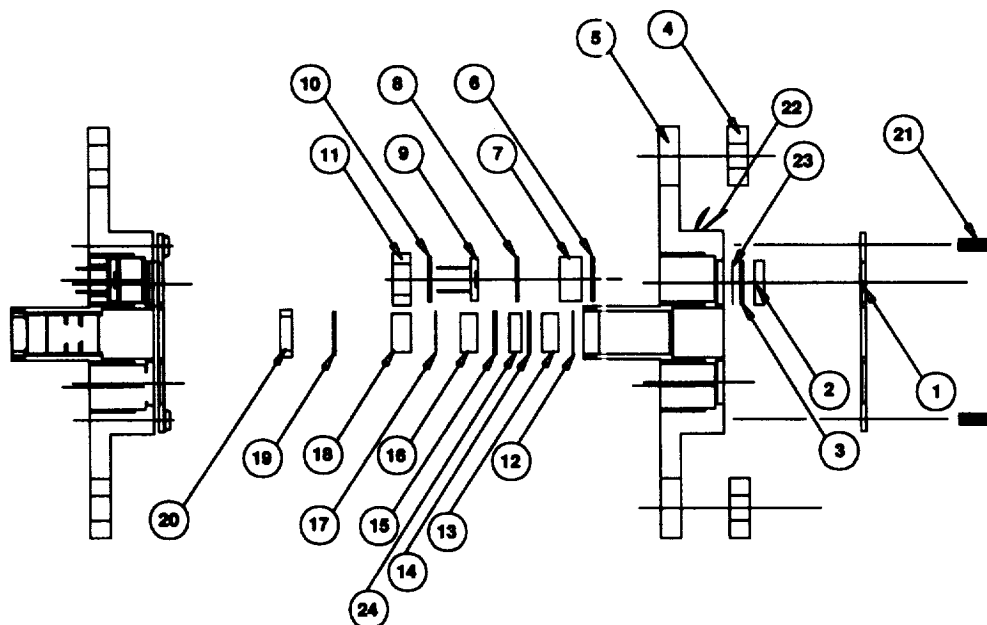


**Fig. 6.** Engineering assembly drawing of the DPA of the SXR. The parts labeled 1–24 correspond to the 1) filter aperture retainer; 2) filter spacer; 3), 6), and 8) are filter washers; 4) plastic spacer; 5) detector plate; 7) interference filter; 9) silicon photodiode; 10) detector back plate; 11) retaining ring; 12) and 23) are electroformed apertures, 3.57 mm ID; 13) aperture spacer, 5.1 mm long; 14) aperture, 5.0 mm ID; 15) aperture, 6.3 mm ID; 16) aperture spacer, 5.4 mm long; 17) electroformed aperture, 7.98 mm ID; 18) aperture spacer, 6.1 mm long; 19) aperture, 9.8 mm ID; 20) retaining ring; 21) 6-32×9 mm fasteners; 22) bead thermistor; and 24) aperture spacer, 3.7 mm long.

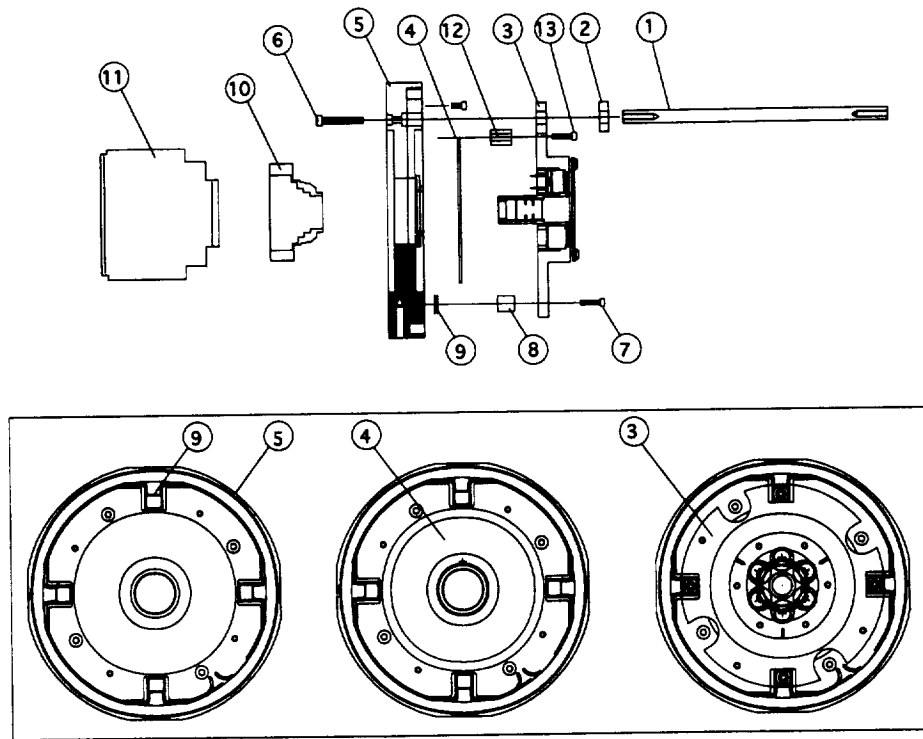


**Fig. 7.** Engineering assembly drawing of the ATA. The parts labeled 1-13 correspond to the 1) support rod, 2) plastic spacer, 3) DPA, 4) amplifier circuit board, 5) ambient temperature plate, 6) 6-32×19 mm fasteners, 7) 6-32×12 mm fasteners, 8) thermal conductors, 9) TEC, 10) F-to-C mount adaptor, 11) objective lens, 12) Delrin spacer, and 13) 6-32×25 mm fasteners (nylon). The bottom three smaller drawings indicate some of the interior components in greater detail.

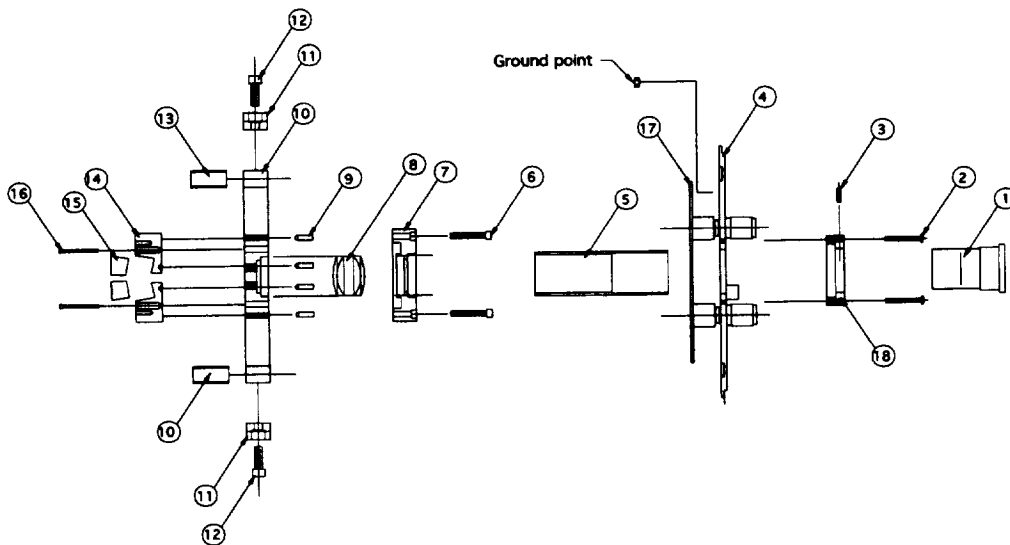


**Fig. 8.** Engineering assembly drawing of the MMA and the BPA of the SXR. The parts labeled 1-18 correspond to the 1) Ramsden eyepiece, 2) 2-56×12 mm long fastener, 3) 2-56×5 mm long nylon tipped set screw, 4) back plate, 5) eyepiece holder, 6) 4-40×19 mm long fastener, 7) lens retainer cap, 8) relay lens, 9) 4-40×19 mm long fastener (modified), 10) mirror mounting plate, 11) clamp, 12) 8-32×12 mm long fastener, 13) brass split ring, 14) mirror cell, 15) mirror segment, 16) 0-80×19 mm long fastener (modified), 17) control circuit board, and 18) eyepiece collar.

The outer housing (Fig. 4) slides over the entire instrument and screws into the ATA. The outer housing end cap (Fig. 4) screws onto the outer housing and is flush against the BPA. For the purpose of troubleshooting, alignment, or repair, the SXR can be operated by qualified personnel either without the outer housing, or with the ATA or BPA hinged open (Fig. 4), because the wiring harness has adequate flexibility. This feature proved invaluable during the development of the SXR. The majority of the parts of the SXR are made from aluminum (alloy 6061). A few parts are made from copper or stainless steel. The aluminum and copper parts were black-anodized after a trial assembly of the SXR. The stainless steel parts, including fasteners, were made black using an oxide finish.

The ATA has four threaded holes for attaching the SXR to a mounting plate, so that the SXR can be rotated 90° about the optical axis. The four orientations are distinguished by the location of the cable for the temperature control system (TEC and thermistor). A convention based on compass values was adopted. When viewing the SXR from the rear towards the source, the location of the TEC cable is *north* (N) when it is farthest from the floor, *south* (S) when it is closest, *east* (E) when it is on the right hand side of the optical axis, and *west* (W) when on the left hand side. The six measurement channels have a six-fold symmetry about the optical axis, with channel 3 and 6 co-linear with the TEC E-W axis. Again viewing the SXR from the rear, starting with the TEC cable (E position) and moving clockwise, the detectors for each channel are arranged symmetrically around the optical axis in this order: detector 3 (E), 4, 5, 6 (W), 1, 2.

### 2.2.1 Detector Plate Assembly

The DPA consists of the detector plate and associated components (Fig. 6). The copper detector plate is 125 mm in diameter and 20 mm thick in the central region, with a 24 mm long cylindrical extension tube. The detector plate is mounted on the four support rods using Delrin (plastic) spacers for thermal isolation. The ID of these spacers is slightly larger than the outside diameter (OD) of the support rods, and the OD of the spacers is made to fit snugly in the detector plate. This arrangement provides excellent mechanical support while maintaining thermal isolation.

To secure the DPA to the ATA, four nylon screws are used. Specially-machined Delrin spacers, shown in Fig. 7, are used as standoffs and along with the screws, attach the DPA to the ATA. Thermal contact between these two assemblies is through four TECs. Four copper spacers, labeled "thermal conductor" in Fig. 7, are screwed to the DPA at four equally spaced locations on a 113 mm diameter bolt circle. On the ATA, four slots the size of the TECs were milled and spot-relieved at the edges so that the TECs could be fixed into the slots without creating a thermal short between the top and bottom of the TEC junctions. With the DPA and the ATA assembled using

the nylon screws, the thermal conductors are flush with the top side of the TECs, thus closing the thermal circuit.

Several mounting holes are used in the DPA to hold the other components. The 24 mm long cylindrical tube is threaded (M15×1) on the inside and holds the field stop and several apertures, which serve as baffles. These parts are inserted in the tube and then held in place with a retaining ring. A set of six equally-spaced threaded holes, M16×1.5 (fine) on a 34.4 mm diameter circle hold the interference filters and silicon photodiodes. Delrin washers are used to cushion these optical components from the copper. To assemble, the parts are inserted from the side of the DPA that is next to the amplifier circuit board and held in place with a threaded retaining ring. The rectangular-shaped ceramic package of the silicon photodiodes was chosen because this design is thinner than the other choice of photodiode packaging (the TO-8), and space along the optical axis is limited. The use of the plastic washers and the ceramic package probably increased the thermal equilibration time for these components; several hours should be allowed for thermal stabilization prior to measurements with the SXR.

With the detectors and interference filters held loosely in place with the retaining rings, the amplifier circuit board was attached to the detectors. Twelve integrated circuit (IC) pin sockets were fixed to the board so they align to the pins of the six detectors when they are centered in the M16 holes. The board was screwed into the DPA using nylon washers as standoffs, and then the retaining rings in the M16 holes were made tight. This arrangement required clipping the leads of the detectors to the correct length; also pieces of Teflon insulation from 22 gauge wire were placed over the leads, thereby eliminating electrical contact between the leads and the detector plate.

Great care was taken to prevent dirt, oil, salt, or other contaminants from accumulating on the components or circuit boards during assembly, as stray capacitance degrades the performance at high amplifier gain. Finally, care was taken so that all six detectors were in the same electrical orientation with respect to the anode of the photodiode and the input to the operational amplifiers. A second set of six mounting holes, aligned to the detector set but on a circle of 32 mm in diameter, hold the electroformed apertures. Provisions were made for adding heat absorbing glass filters in the event that the interference filters were found to have unacceptable spectral transmittance at longer wavelengths. This was not necessary, however, and filter washers of the same thickness as the glass filters were used. The electroformed aperture and the filter washers were held on the DPA with a retainer piece.

### 2.2.2 Ambient Temperature Plate Assembly

The ATA serves as the mechanical baseplate and heat sink for the SXR. It is also the assembly that mounts to the tripod, or other fixture, during measurements. An inside

thread on the side of the ATA, which is next to the amplifier circuit board, is used to capture the outer housing (Fig. 7). The overall dimensions are 159 mm (diameter) by 22 mm (thick). During assembly, the four TEC units were fixed in the milled slots using a thermally-conducting, silver-filled epoxy. The TECs were then connected as described in Sect. 2.3. The F-to-C mount adaptor was attached to the ATA with the C-mount thread, and then the 85 mm  $f/1.4$  objective lens was mounted to the F-to-C mount adaptor with the standard bayonet-type mount found in 35 mm Nikon cameras. Black felt cloth was epoxied behind the lens, on the inside of the F-to-C mount adaptor, in order to reduce the effect of scattered light on the spatial responsivity function of the SXR at the longer wavelength measurement channels.

### 2.2.3 Mirror Mount Assembly

The MMA holds the six wedge-shaped relay mirrors (part of the measurement optics), as well as the relay lens (part of the alignment optics). The MMA is designed to slide on the support rods using a clamp and split-washer ring design (Fig. 8) so that the optical components can be placed the optimum distance from the field stop. The MMA is an octagonal-shaped plate with the overall dimensions of 113 mm (width) by 12.7 mm (thickness). To assemble the MMA, the mirror segments were fixed to the mirror cells using epoxy. The mirror cell was designed so that the mirror segments, which must be tilted to satisfy the off-axis design, are in the proper orientation when the back of the mirror cell is flush with the mirror-mounting plate.

Since slight adjustment in each of the six optical systems was desired, the mirror cells were mounted to the mirror mounting plate so that kinematic adjustments with three degrees of freedom are possible (two rotation and one translation). The back of each mirror cell is designed for three-point contact with the tip of three 4-40 set screws. One contact point is flat; the other is a conical, V-shaped hole; and the third is a V-shaped slot. The mirror cell is held to the mirror mounting plate using a 0-80 screw; the head of the screw is on the mirror side of the MMA and the washer and nut are on the back side of the mirror mounting plate. The underside of the head of the 0-80 screws was machined to a radius of 0.51 mm so the screw will pivot in its mounting hole as the mirror cell is adjusted using the three set screws. The tip of these set screws was machined to a radius of 1.42 mm.

The assembly of the MMA was completed by attaching the mirror cells to the mirror mounting plate and then sliding the MMA over the support rods. The distance between the MMA and the DPA was set to the design value and the MMA was clamped to the support rods. The mirror cells were aligned flush to the mirror mounting plate, but the 0-80 screws were not fully tightened. A uniform source of radiance was used to illuminate the optics of the SXR

and the 4-40 set screws were adjusted until the image of the field stop for each measurement channel was centered in the electroformed aperture, which is in front of each interference filter; the 0-80 screw was made tight. Once the alignment of the mirror segments was finished, the relay lens was attached to the back of the MMA.

### 2.2.4 Back Plate Assembly

The BPA holds the control circuit board, the electrical connections, and the eyepiece assembly. The circuit board is attached to the back plate using the connectors associated with the various switches and connectors. The eyepiece tube is held in the eyepiece collar using two nylon-tipped set screws. The eyepiece collar is attached to the back plate using six 2-56 fasteners. The eyepiece slides inside the eyepiece tube and can be removed if necessary. The eyepiece cap is made from Delrin and is used to block radiant flux from entering the SXR housing during measurements. Prior to assembly, the back plate was engraved with a number of labels. Because the amplifier and control circuit boards were modified (Sect. 2.3), not all of the labels line up with the switch positions.

## 2.3 Electrical

The electrical subsystems in the SXR consist of the amplifier and control circuit boards and a triple output DC power supply (Multiproducts part number T515750/1). The purpose of the amplifier board is to convert photocurrent to voltage using a fixed value for the transimpedance gain for each measurement channel. Channels corresponding to the shorter measurement wavelengths, where the minimum spectral radiances for a source generally occur, have higher gain than the channels at the redder measurement wavelengths (Table 3). The purpose of the control circuit board is to vary the gain of a voltage amplifier that is in series with output from an individual transimpedance amplifier. The voltage board also selects the amplifier corresponding to the desired channel.

The SXR can be operated in a local mode, with manual control of the gain and channel settings, or in a remote mode, with parallel interface to a transistor-transistor logic (TTL) digital input-output (DIO) card, such as the NB-DIO-96 card from National Instruments. The DIO interface was a modification to the SXR, and the addition of the 9-pin connector on the BPA required material to be removed from the eyepiece collar. Also, the rotary switches (below) for the revised control circuit board are different than the original ones, and the labels on the BPA do not line up with the switch positions. The amount of angular rotation per switch position is smaller for the present switches, otherwise they operate as the labels on the BPA would indicate.

A schematic that illustrates both circuits is shown in Fig. 9. The design of the individual transimpedance amplifiers is based on standard operation amplifier circuitry

**Table 3.** Values of the feedback resistor,  $R_F$ , and the damping capacitor,  $C_F$ , for the six measurement channels of the SXR.

Channel	$\lambda_m$ [nm]	Photodiode Model Number	$R_F$ [M $\Omega$ ]	$C_F$ [pF]
1	411.222	S1227-66BQ	1,000	10
2	441.495	S1227-66BQ	1,000	10
3	486.938	S1227-66BQ	100	100
4	547.873	S1227-66BQ	100	100
5	661.718	S1227-66BQ	100	100
6	774.767	S1337-66BQ	10	1,000

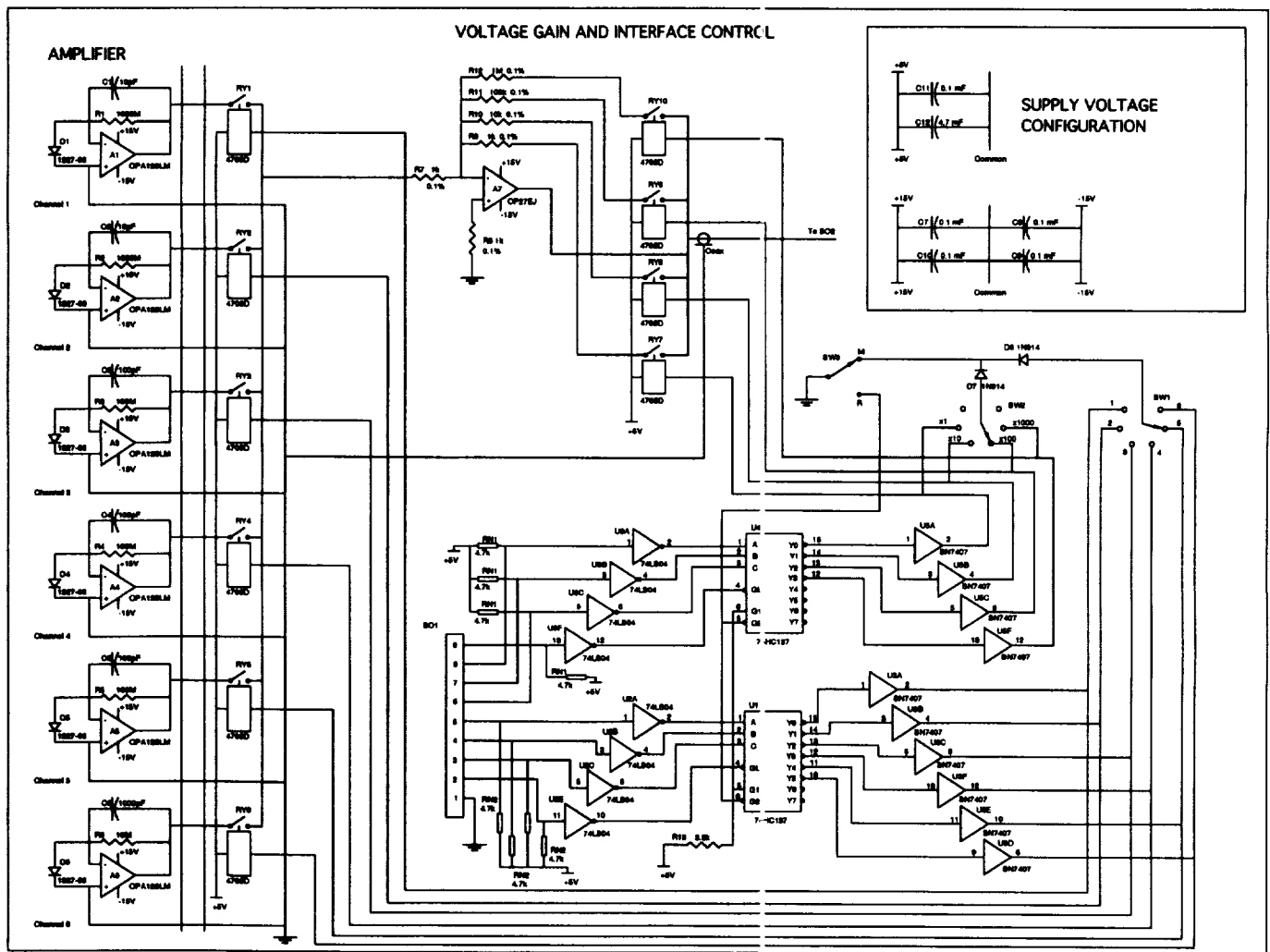


**Fig. 9.** Circuit diagram for the amplifier and control circuit in the SXR. Refer to Table A1 in Appendix A for an itemized list of the parts used.



(Graeme 1995 and Stout 1976), using configurations similar to designs used at NIST for silicon detector radiometers and photometers (Fowler 1977, Eppeldauer 1991, and Eppeldauer and Hardis 1991). An operational amplifier with low bias current, the OPA128LM from Burr-Brown, has the anode and the cathode of the silicon photodiode connected to its isolated field-effect transistor (FET) input (A1–A6 in Fig. 9). A feedback resistor, which has a small temperature coefficient, sets the transimpedance gain. A capacitor, in parallel with the feedback resistor, provides the high frequency roll-off, and sets the time constant to 10 ms. A variable resistor, Bourns part number 3266W, is used to trim the input offset voltage of each OPA128LM to a small value, typically less than 1 mV referenced to the output (the variable resistor is not shown in Fig. 9). The actual items that correspond to the numbers given in the figure are listed in Appendix A.

Shielded, coaxial cable is used to bring the output of each amplifier to the control circuit board. Depending on the state of a set of six relays (Gordos reed relays, model 4705D), the output of one of the six transimpedance amplifiers is connected to the input of the voltage amplifier. This amplifier circuit, which has selectable gain from unity to 1,000 by factors of 10, uses the OP27EJ low noise precision operational amplifier from Precision Monolithics Incorporated (A7 in Fig. 9). The 0.1% feedback resistors, from 1 k $\Omega$  to 1 M $\Omega$ , are selectable using additional relays. The same variable resistor (Bourns part number 3266W), is used to trim the input offset voltage of A7. The resistor is accessible from the outside of the SXR if a small set screw in the BPA is removed. When the SW3 toggle switch is in the manual position, the output of the demultiplexers are logic high (the 74HC137 IC from Texas Instruments is used for the demultiplexer), and the reed relays are set manually using rotary switches SW1 (channel) and SW2 (gain). When SW3 is in the remote position and there is no input on pins 2–9 of SO1, the SXR is automatically placed in the configuration to output the signal at 411.5 nm (channel 1) with unity gain on the voltage amplifier. BNC connector SO2, which is on the BPA, provides external access to the output of the voltage amplifier.

In the remote mode, the configurations of the SXR are programmed using TTL logic to a 9-pin connector, SO1; the parallel input is buffered and inverted using SN74LS04 digital logic ICs, and is then decoded by the two demultiplexers: one for the gain and the other for the channel. The output of the demultiplexers are the input to two SN7407 ICs, which function as a buffer for the Gordos relays. One of the pins in SO1 is used for the ground, four are used for the gain demultiplexer and four are used for the channel demultiplexer. In each set of four signals, three are data lines and the fourth is used to strobe the demultiplexer. The data lines to the SXR use binary coded decimal (BCD) encoding. The input lines to the SXR (connector SO1) use true low logic. “Low” is defined as any voltage below 0.8 V DC and “high” is defined as any voltage above

2 V DC. Socket assignments for the channel and gain are shown in Table 4, and the control logic states are given in Table 5. Initially, the data lines must be set high and the strobe lines low. Then the channel and gain may be selected. For example, to select channel 2 with a gain of 1,000, pins 5, 7, and 8 in SO1 would be taken low, then the strobe lines, pins 2 and 9, would be taken high and then low. The channels and the gain may be changed independently using only the appropriate data and strobe lines. The gain and channel selection will remain fixed as long as the strobe lines are held high. The SXR may also be used in a *pass-through* mode by leaving the strobe lines in a low state. The data lines must then be latched with the external drive circuitry. There is no way to read the state of the channel or gain settings of the SXR.

**Table 4.** The function of the 9-pin connector SO1 for parallel interface to the SXR.

Pin Number SO1 Socket	Function	BCD Assignment
5	Channel Data	1 (LSB)†
4	Channel Data	2
3	Channel Data	4 (MSB)‡
2	Channel Strobe	
1	Common	
9	Gain Strobe	
8	Gain Data	1 (LSB)
7	Gain Data	2
6	Gain Data	4 (MSB)

† LSB = least significant bit.

‡ MSB = most significant bit.

**Table 5.** Interface control logic states for the SXR.

Channel	Pin 3 (MSB)	Pin 4	Pin 5 (LSB)
1	High	High	High
2	High	High	Low
3	High	Low	High
4	High	Low	Low
5	Low	High	High
6	Low	High	Low
Gain	Pin 6 (MSB)	Pin 7	Pin 8 (LSB)
×1	High	High	High
×10	High	High	Low
×100	High	Low	High
×1,000	High	Low	Low

The circuit boards were designed at NIST using Protel software; the boards were made from Rexolite 2200 and were printed to NIST's specifications using a commercial vendor. The boards were assembled, cleaned, baked at approximately 50°C for about 24 hours, and then tested, with the two boards connected as shown in Fig. 9. After assembling these circuit boards into the SXR (Sect. 2.2)

**Table 6.** Details of the electrical wiring for the SXR.

Conductor	Function	Connector or Location	Pin Number
Blue	+15 V DC	SO3 and Wiring Harness	5
Yellow	-15 V DC	SO3 and Wiring Harness	4
Red	+5 V DC	SO3 and Wiring Harness	3
Green	Ground (power supply)	SO3	1
Brown	Common (pre-amplifier)	Wiring Harness	N/A
N/A	Shield	SO4	N/A
Green	Thermistor	SO4 and Wiring Harness	N/A
White	Thermistor	SO4 and Wiring Harness	N/A
Red	TEC Devices	SO4 and Wiring Harness	N/A
Black	TEC Devices	SO4 and Wiring Harness	N/A
Black (coax)	A1 Output	Wiring Harness	N/A
Black (coax)	A2 Output	Wiring Harness	N/A
Black (coax)	A3 Output	Wiring Harness	N/A
Black (coax)	A4 Output	Wiring Harness	N/A
Black (coax)	A5 Output	Wiring Harness	N/A
Black (coax)	A6 Output	Wiring Harness	N/A
N/A	A7 Output	SO2	N/A
N/A	Channel Data LSB	SO1	5
N/A	Channel Data	SO1	4
N/A	Channel Data MSB	SO1	3
N/A	Channel Strobe	SO1	2
N/A	DIO Common	SO1	1
N/A	Gain Strobe	SO1	9
N/A	Gain Data LSB	SO1	8
N/A	Gain Data	SO1	7
N/A	Gain Data MSB	SO1	6

and completing the thermal circuit (Sect. 2.4), the amplifier common, the power supply common, the TEC cable shield, the DPA, BPA, and the ATA were grounded at a common location at the DC power connection to reduce the sensitivity to noise caused by the 60 Hz frequency of the power grid, as well as to prevent ground loops. Table 6 summarizes the wiring configurations in the SXR. The offset voltages on the OPA128LM operational amplifiers were set to small values by eliminating all radiant flux and monitoring the output of each amplifier in turn, using a DMM. Then, the trimpots were locked in position using a drop of Glyptol. (Possibly a better procedure would have been to trim the offset voltages before the photodiodes were attached to the circuit, while electrically shorting the input of the OPA128LMs.) Next, the trimpot on the OP27EJ was adjusted in a similar fashion. Unfortunately, the ratio of the resistances of the feedback resistors for the OP27EJ was not measured using a high precision, accurate current source. As in the trimming of the offset voltages, this should have been done before the photodiodes were attached to their respective transimpedance amplifiers. Instead of repeating the delicate and difficult assembly process, these gain ratios were measured radio-metrically (Sect. 3.2.1).

## 2.4 Thermal

The thermal circuit maintains the DPA at 26°C using the TECs and a bipolar commercial temperature controller (ILX Lightwave model LDT-5910B). Because the amplifier circuit board is adjacent to the DPA, to some extent the circuit board is held at a fixed temperature, although the value reached in equilibrium may depend on the ambient temperature. For this reason, the SXR should be used for radiance measurements in a stable thermal environment after the unit has reached thermal equilibrium. For most operations, the SXR is left on and at temperature.

The TECs (part number I1025T from Marlow Industries, Inc.) are made from a set of thermoelectric junctions, which consist of p- and n-type semiconductor material. These junctions are connected in series for the electrical circuit, and current of either polarity is sent through the device to heat or cool the DPA. The junctions are connected in parallel for the thermal circuit, and the two sides of this circuit are mated to square, thin, ceramic pieces. The same ceramic side for the four TECs was epoxied to the ATA as described in Sect. 2.2. Because the electrical leads to the TECs are very delicate, the electrical conductors were fixed to the ATA using room temperature vulcanizing (RTV) silicone rubber. Each of these TECs

can sustain a temperature difference of 67°C in a vacuum, has the greatest cooling at 1.8 A, and if there is no heat load, produces a voltage of 4.4 V DC at 1.8 A. At 1.8 A, a heat load of 5.0 W will result in zero temperature difference across the thermal circuit of the TEC. The resistance of these units is very sensitive to temperature, and although it is difficult to measure a DC resistance at room temperature, it is approximately a few ohms.

The four TECs were connected as two sets of two in parallel, and then the two sets were connected in series. This electrical combination results in an input impedance equivalent to a single TEC. The four TECs could not be connected in series because the ILX Lightwave LDT-5910B thermoelectric temperature controller was not designed for loads with the combined resistance of four TECs. A bead thermistor, model 1T1002-5 from ILX Lightwave, was fixed in a small hole in the DPA using silver-filled epoxy. The four electrical connections of the thermal circuit, two connected to the TEC combination and two connected to the thermistor (about 10 k $\Omega$  at ambient temperatures), are brought to the BPA using shielded cable. The cable extends about 2 m to a 15-pin subminiature D connector, where it is attached to the LDT-5910B controller. In retrospect, a connector should have been used on the BPA, so that no cables are attached to the SXR during shipment or transport.

When the TEC system and the thermistor are connected properly, the LDT-5910B is set to maintain the DPA at 26°C. The controller uses the following interpolating equation as part of the proportional, integral, differential (PID) control of the temperature,  $T$ , of the DPA:

$$\frac{1}{T} = C_1 10^{-3} + C_2 10^{-4} \ln \mathfrak{R} + C_3 10^{-7} (\ln \mathfrak{R})^3, \quad (1)$$

where  $C_1$ ,  $C_2$ , and  $C_3$  are constants supplied with the thermistor and are programmed into the LDT-5910B using the front panel controls, and  $\mathfrak{R}$  is the value of the resistance of the thermistor, typically 10–15 k $\Omega$  at room temperature. Unfortunately, the calibrated thermistor supplied with the unit was damaged when it was placed in the DPA, and an uncalibrated thermistor was mounted in one of the extra thermistor mounting holes. The constants  $C_1$ ,  $C_2$ , and  $C_3$  were determined by operating the thermal circuit of the SXR and measuring the temperature of the DPA using a commercial thermocouple; the values for these constants are given in Table 7. Therefore, the temperature of the DPA is maintained with a precision of 0.1°C, but the uncertainty in the actual value is probably about 0.5°C. This is not important as long as the SXR is operated in a consistent manner.

**Table 7.** Parameters for the ILX controller for SXR operation at 26°C.

Parameter	Value
$C_1$	1.052 [K <sup>-1</sup> ]
$C_2$	2.490 [K <sup>-1</sup> (ln V/A) <sup>-1</sup> ]
$C_3$	0.000 [K <sup>-1</sup> (ln V/A) <sup>-3</sup> ]

Four TECs were used in the SXR because of the large mass of the DPA and the desire to achieve small and symmetrical thermal gradients at the locations of the critical components. Using more than one TEC element, however, can result in failure modes that are not present when only one element is used. In the case of a single TEC, the functions of the LDT-5910B controller, a 16 W unit, would maintain the current to 1.8 A or less. In the case of the SXR, if poor thermal contact at one of the TECs results in a hot spot, the resistance can increase so that the maximum voltage is exceeded even if the LDT-5910B is set to source less than 1.8 A. This will result in a step-wise failure of all of the TECs. In order to prevent this mode of failure, a paste designed to minimize thermal resistance between mechanical parts was used between the copper thermal conductors, the DPA, and the top of the TECs. If the thermal resistance is too large for safe operation, the front of the ATA may feel warm to the touch, particularly at four equally spaced locations corresponding to the TECs. This should not occur, however, unless the ATA and the DPA are disassembled and reassembled in an improper fashion.

## 2.5 Data Acquisition

The voltages from the SXR are measured using a calibrated DMM. Even though radiant flux reaches all six detectors simultaneously, only one channel can be read at any particular time (Sect. 2.3). In all cases where computer-archived results are desired, a General Purpose Interface Bus (GPIB)-programmable DMM is used to measure the voltages. Depending on the type of test at NIST, which included the radiometric characterization of the SXR (Sect. 3), a particular data acquisition program was used to control the DMM. These programs were developed by NIST using Visual Basic (Microsoft Corporation) and LabVIEW (National Instruments) application software; in most cases, the development of these applications preceded the development of the SXR.

When the SXR is used with a white light source, large volumes of data must be recorded, some of which are associated with a particular voltage reading and some of which are the same for the entire experiment. The organization of the desired file structure is given in Hooker et al. (1994), and computer software was developed according to these recommendations.

For the initial deployments of the SXR (e.g., the Honolulu measurements in February 1994), a data acquisition program using Visual Basic was developed by NIST and used on a portable personal computer (PC) which was equipped with an expansion chassis. Later, after the parallel interface was implemented, the SeaWiFS Project developed a data acquisition program using LabVIEW and installed this program on a Macintosh IIfx computer. The complete, field-deployable system consists of the SXR, a Hewlett-Packard (HP) 34401A DMM, an LDT-5910B thermoelectric temperature controller, a Macintosh IIfx, and

associated cables and instruction manuals for the equipment. The field-deployable system is shipped using four sturdy equipment cases with a total weight of 96 kg.

Information on the SXR system and the data acquisition software is provided in the SXR operating manual which is now being written; the general features are summarized here. The program, SXR VI-Final, is menu based and it is to be operated in concert with the SXR Log Sheets, which are used to describe the experiment. The date, file name, experimental parameters, and other general data are entered into the program, which writes a header block in the data file. The particular channels to be measured, the gain to be used, the number of samples to be recorded, the type of measurement, text comments (if any), and the delay between trigger signals to the DMM are entered.

Once all of the desired parameters are satisfactory, the computer program executes the corresponding events and writes the results in a single tab-delimited record of the data file. This record represents a set of SXR data. The average and standard deviation are recorded in one file, and the individual voltages in a separate file. A portion of the results is also displayed on the computer screen.

Individual measurements can be repeated for as long as the experiment continues. Using an existing file name gives concatenated results, with header data located between the records representing individual measurements. Several important parameters are associated with the DMM, some of which are set by the computer program. If operation is required for configurations other than the default state of the DMM, it must be changed to *local mode* and adjusted before operating SXR VI-Final. Some of these may be altered by the program, for example the autoranging function is under computer control. In order to maximize the resolution of the measurement for each data record, five preliminary readings are taken with the autoranging feature on, then the range is set to what appears to be a reasonable value and the required number of samples are recorded. If the DMM over ranges during one of the final readings, the maximum voltage is increased by a factor of three and the entire sequence is repeated.

### 3. PERFORMANCE ANALYSIS

#### 3.1 Measurement Equation

Developing a measurement equation is absolutely essential in measurement science. First, the relationship among all the factors that affect the instrument response are clearly identified and parameters such as "calibration coefficients" are assigned physical meaning. Second, even when the measurement equation must be approximated, it serves as a useful basis for the uncertainty analysis. Without uncertainties, the measurement itself conveys no information. In Appendix C of Johnson et al. (1996), a simple

measurement equation is described for a filter radiometer, such as the SXR, observing a source of spectral radiance:

$$S = \int L(\lambda)R(\lambda) d\lambda, \quad (2)$$

where  $S$  is the net measured signal,  $L(\lambda)$  is the spectral radiance of the source, and  $R(\lambda)$  is the absolute spectral responsivity function of the radiometer.

For the SXR, there are six versions of (2), one for each channel; (2) is a simple form of the measurement equation because it does not consider the dependence on the spatial and angular coordinates of the spectral radiance. The state of polarization, the magnitude, and the temporal behavior of the spectral radiance may also be important, but are not included in (2). Also not included in (2) is the dependence on the value of the amplifier gain setting, and for radiometers without temperature stabilization, the effect of variations in ambient temperature. Note that the properties of the source must be known to fully describe the relationship between the output signal of the radiometer and the spectral radiance of the source. By using specialized sources, portions of the relationship were measured for the SXR, and suitable measurement equations were necessary to describe these measurements and estimate the uncertainties.

In Sect. 3.1.1, (2), which accounts for the spectral responsivity, is generalized to include spatial responsivity and the dependence on amplifier gain, resulting in a fundamental SXR measurement equation (and definition of the calibration coefficients). Linearity studies were performed and the results are described in Sect. 3.2.4. Because the SXR is very linear, no modification of the measurement equation was required.

##### 3.1.1 Spatial and Spectral

Kostkowski and Nicodemus (1978) show that if the polarization state and temporal fluctuations of the source can be neglected, the responsivity of the radiometer is independent of time, and nonlinear effects are negligible, then

$$S = \int_{\lambda} \int_{x,y} \int_{\omega} L(x,y,\theta,\phi,\lambda) \times D(x,y,\theta,\phi,\lambda) \cos \theta d\omega dx dy d\lambda. \quad (3)$$

In (3),  $D(x,y,\theta,\phi,\lambda)$  is the spectral-ray flux responsivity for the flux element  $L(x,y,\theta,\phi,\lambda) \cos \theta d\omega dx dy d\lambda$ . Here,  $\lambda$  is the wavelength,  $x$  and  $y$  are coordinates describing a location in the entrance window of the radiometer (the plane containing the source), and  $\omega$  is a solid angle. The coordinates  $\theta$  and  $\phi$  are the polar and azimuthal angles describing the direction of the ray relative to the ray that is perpendicular to the source plane, and  $d\omega$  is the solid angle subtended at  $x,y$  by a differential area in the entrance pupil. The above, (3), depends on the actual properties of

the radiometer and the source under study. As in Johnson et al. (1996), a second equation that describes the relationship between the spectral radiance of the source and the properties of the radiometer is used to describe the spectral radiance to be measured,  $L(\lambda_m)$ , where  $\lambda_m$  is the measurement wavelength and  $m$  denotes measurement;  $\delta(x - x_m)$ ,  $\delta(y - y_m)$ ,  $\delta(\theta - \theta_m)$ ,  $\delta(\phi - \phi_m)$ , and  $\delta(\lambda - \lambda_m)$  are the Dirac delta functions for the variables  $x$ ,  $y$ ,  $\theta$ ,  $\phi$ , and  $\lambda$ , respectively:

$$\begin{aligned} L(\lambda_m) &\equiv L(x_m, y_m, \theta_m, \phi_m, \lambda_m) \\ &= \int_{\lambda} \int_{x,y} \int_{\omega} L(x, y, \theta, \phi, \lambda) \\ &\times \delta(x - x_m) \delta(y - y_m) \delta(\theta - \theta_m) \\ &\times \delta(\phi - \phi_m) \delta(\lambda - \lambda_m) \cos \theta d\omega dx dy d\lambda. \end{aligned} \quad (4)$$

This equation describes an ideal measurement of spectral radiance, with the radiometer sampling infinitesimal spatial, angular, and spectral coordinates.

For the types of sources considered here, a simplifying assumption is made that the spectral and spatial properties of the source are separable. Then,  $L(x, y, \theta, \phi, \lambda)$  is equal to  $L(\lambda)l(x, y, \theta, \phi)$ , where  $l(x, y, \theta, \phi)$  is a relative spatial distribution function that is normalized to unity. Furthermore, it is assumed that for all sources of interest, the sources are uniform within the source aperture and lambertian within the field of view of the radiometer, so that the factor  $l(x, y, \theta, \phi)$  is independent of  $x$ ,  $y$ ,  $\theta$ , and  $\phi$ .

The factor  $S/L(\lambda_m)$  is the average spectral radiance responsivity, or spectral radiance calibration factor,  $\langle D \rangle$ . This factor is a function of the spectral radiance of the source being measured, as well as the properties of the SXR. The calibration correction factor,  $k(\lambda_m)$ , of the SXR is the ratio of the average spectral radiance responsivities determined from the measurements of a source of known spectral radiance (the calibration source, hereafter denoted with a subscript "cs") and a test source under study (the measured source, hereafter denoted with a subscript "ms"):

$$\begin{aligned} L_{ms}(\lambda_m) &= \frac{S_{ms}}{S_{cs}} L_{cs}(\lambda_m) k(\lambda_m) \\ &= \frac{S_{ms}}{\langle D_{cs} \rangle} k(\lambda_m), \end{aligned} \quad (5)$$

where

$$k(\lambda_m) = \frac{\langle D_{cs} \rangle}{\langle D_{ms} \rangle}. \quad (6)$$

The calibration correction factor characterizes the difference between the response of the SXR to the measured source and the calibration source, and should be close to unity for similar sources. For each measurement, the calibration correction factor should be calculated by evaluating the integrals in (3); however, this requires a priori knowledge of the spectral radiance of the measured source.

If these data are available, then  $k(\lambda_m)$  can be determined, and the SXR data can be used to verify the spectral radiance of the measured source. That is,  $L_{ms}(\lambda_m)$  can be compared to the value predicted from independent calibration data. If the measured source has not been calibrated by other means, and the spectral radiance is unknown, then assumptions can be made about  $k(\lambda_m)$  (for example, that the correction factor is unity), and then the SXR can be used to measure the spectral radiance of the test source.<sup>†</sup>

For the SXR, (3) was simplified further by assuming that the spectral and spatial properties of the spectral-ray flux responsivity are separable, and approximated by the product

$$D(x, y, \theta, \phi, \lambda) = G R_F \Psi h(x, y) \eta(\theta, \phi) \rho(\lambda), \quad (7)$$

where  $G$  is the gain of the voltage amplifier (dimensionless),  $R_F$  is the gain of the transimpedance amplifier (typical units are volts per ampere);  $\psi$  is a constant (typical units are amperes per watts); and  $h(x, y)$ ,  $\eta(\theta, \phi)$  and  $\rho(\lambda)$  are relative spatial, angular, and spectral response functions, respectively, which are normalized to unity. The function  $\rho(\lambda)$  accounts for the spectral dependence of the detector responsivity and the transmittance and reflectance of the optics, including interreflections. The product of the function  $h(x, y)$  and  $\eta(\theta, \phi)$  account for vignetting, scattered light, and uniformity. The gain  $R_F$  is the value of the feedback resistor (Fig. 9), and  $\psi$  is the product of the responsivity of the silicon photodiode detector and the transmittance and reflectance of the optics in the measurement channel at a particular wavelength. Then

$$k(\lambda_m) = k_G k_{\lambda} k_a, \quad (8)$$

where  $k_G$ ,  $k_{\lambda}$ , and  $k_a$  are the gain, spectral, and spatial calibration correction factors, respectively. These factors are determined as:

$$k_G = \frac{G_{cs}}{G_{ms}}, \quad (9)$$

$$k_{\lambda} = \frac{\int L_{cs}(\lambda) \rho(\lambda) d\lambda}{\int L_{cs}(\lambda) \delta(\lambda - \lambda_m) d\lambda} \frac{\int L_{ms}(\lambda) \delta(\lambda - \lambda_m) d\lambda}{\int L_{ms}(\lambda) \rho(\lambda) d\lambda}, \quad (10)$$

and

$$k_a = \frac{\int_{A_{cs}} h(x, y) dx dy}{\int_{A_{ms}} h(x, y) dx dy}, \quad (11)$$

where  $A$  is the source area,  $A_{cs}$  is the calibration source area, and  $A_{ms}$  is the measured source area. The integral over the angular coordinates is eliminated because in all

<sup>†</sup> In this case, an improved estimate for the spectral radiances at the measurement wavelengths could be determined by using the initial values to estimate  $L_{ms}(\lambda)$  and then determining the spectral contribution to the correction factor.

cases, the source is assumed to be lambertian and is assumed to overfill the field of view of the SXR. In fact, the spatial responsivity measurements were performed using a point source at  $x, y$  in the entrance window, averaging over any nonuniformities in the angular response of the SXR. Also, note that the parameters  $R_F$  and  $\psi$  are common to  $\langle D_{cs} \rangle$  and  $\langle D_{ms} \rangle$ , so that  $k(\lambda_m)$  is independent of these factors.

The measurement results for the characterization of the SXR for the factors in (9)–(11) are given in below: gain ratios (Sect. 3.2.1); spectral responsivity (Sect. 3.2.2); and spatial responsivity (Sect. 3.2.3). The absolute calibration is described in Sect. 3.2.6.

### 3.1.2 Linearity

Implicit in the definition of the spectral-ray flux responsivity,  $D(x, y, \theta, \phi, \lambda)$ , is that the response is independent of the magnitude of the spectral flux element  $L(x, y, \theta, \phi, \lambda) \cos \theta d\omega dx dy d\lambda$ , (3). If this is not the case, then a functional relationship between the spectral flux collected by the radiometer and the output signal exists, of the form  $S \propto \Xi(\Phi(\lambda))$ , where  $\Phi(\lambda)$  represents the input spectral flux and  $\Xi(\Phi(\lambda))$  is an arbitrary, nonlinear function. At high photocurrents (a few milliamperes), silicon photodiodes like those in the SXR will generate excess photoelectrons; but, the maximum photocurrent in the SXR is  $1.2 \mu A$  (channel 6); the amplifier saturates for greater currents. Effects, such as electrical crosstalk in amplifier circuit boards, however, can cause nonlinear behavior, so the SXR was characterized for linearity with input flux using an optical beamcombiner (Thompson and Chen 1994), and the results are described in Sect. 3.2.4.

### 3.1.3 Polarization and Time

If the polarization or temporal behavior are included in the measurement equation, then a procedure similar to that used to treat the spatial and spectral dependencies must be developed. Polarization responsivity functions are required when discussing polarimeters, and temporal functions are necessary if alternating current (AC) detectors are used, the source is moving, and so forth. In addition, if the source used to calibrate the radiometer and the test source are dissimilar in these parameters, it is generally the case that the measurement equation must include these factors as well. As mentioned in the introduction, the polarization responsivity was not measured for the SXR, because its planned use was only with integrating sphere sources. As for the temporal responsivity, the feedback capacitor and resistor set the time constant. To ensure full recovery, a 500 ms delay between readings of the DMM is the normal configuration in the SXR data acquisition software. The overall temporal stability of the SXR as a function of time is assessed in Sect. 3.2.5 by comparing results with the same source. Of course, the source must be stable over the measurement interval.

## 3.2 Characterization and Calibration

This section details the characterization and calibration of the SXR.

### 3.2.1 Gain Ratios

The gain part of the calibration correction factor, repeated from (9), is

$$k_G = \frac{G_{cs}}{G_{ms}}, \quad (12)$$

where the nominal values for  $G$  are 1, 10, 100, and 1,000. As explained in Sect. 2.3, these ratios could have been measured electrically, but were not because this would have required partial disassembly of the SXR. Instead, they were measured radiometrically, using a stable source of variable spectral radiance. The source consisted of an integrating sphere source that was 45.72 mm in diameter with an internal baffle and an external lamp which was enclosed in a housing. The source was from Optronic Laboratories, Incorporated (model number OL455). The exit aperture of the source was 15.24 cm in diameter. The radiance of this sphere source was varied by changing the diameter of an iris diaphragm that was located between the lamp and the entrance port of the sphere. The luminance of the sphere was measured with a built-in monitor photometer.

The sphere was operated at three radiance levels, and measurements were made for each SXR channel at two gain settings for each radiance level. One set of background signals was recorded at each sphere level and SXR gain setting by closing a shutter between the lamp and the entrance to the sphere. Each measurement consisted of 10 readings using an HP 3457A DMM, which was set to average over 10 power line cycles. At the brightest setting, corresponding to about  $1,660 \text{ cd m}^{-2}$ , three data sets at SXR gain 1 and one set at gain 10 were recorded along with the background sets for each of the two gain settings. At the next level, corresponding to about  $172.6 \text{ cd m}^{-2}$ , two data sets at gain 10 and one set at gain 100 were recorded along with the background at the two gain settings. At the lowest level, corresponding to about  $17.44 \text{ cd m}^{-2}$ , two sets at gain 1,000, and one set at gain 100, were recorded along with the background at the two gain settings.

The net signals were determined using the background signals acquired with the same sphere setting; the ratios of the net signal at one gain setting to the net signal at the next gain setting for each channel were averaged. The standard deviation of the ratios was used to estimate the relative standard uncertainty,  $u_G$ .<sup>†</sup> Finally, since the calibration coefficients for the SXR are for gain 1, the ratios of  $k_G$  were normalized to  $G_{cs} = 1$  ( $k_1 = 1$ ) and the results are given in Table 8.

<sup>†</sup> Uncertainties evaluated using statistical means are denoted Type A uncertainties (Taylor and Kuyatt 1994).

**Table 8.** Gain correction factors, and the relative standard uncertainties, as a function of the voltage gain for the SXR.

Gain Indicator	Voltage Gain Factor ( $G$ )	$k_G$	$u_G$ [%]
0	1	1.000000	N/A
1	10	0.1000351	0.0212
2	100	0.00999811	0.0349
3	1,000	0.001000143	0.0851

### 3.2.2 Relative Spectral Response

The spectral part of the calibration correction factor, repeated here from (10), is

$$k_\lambda = \frac{\int L_{cs}(\lambda) \rho(\lambda) d\lambda}{\int L_{cs}(\lambda) \delta(\lambda - \lambda_m) d\lambda} \frac{\int L_{ms}(\lambda) \delta(\lambda - \lambda_m) d\lambda}{\int L_{ms}(\lambda) \rho(\lambda) d\lambda}, \quad (13)$$

where the dependence of  $k_\lambda$  on  $\lambda_m$  and the radiance of the two sources are understood. The first goal is to define  $\lambda_m$ . Johnson et al. (1996) suggested several methods to choose  $\lambda_m$ , and it was shown that for the case where the spectral dependence of the spectral radiance could be approximated as a linear function of wavelength over the bandpass of the filter, then

$$\lambda_m = \frac{\int \lambda \rho(\lambda) d\lambda}{\int \rho(\lambda) d\lambda}. \quad (14)$$

Here, (14) is used, as it is consistent with a reasonable model for the relative spectral shape of the spectral radiance, and because this expression for  $\lambda_m$  is independent of the source radiance, which is convenient for subsequent analysis. Earlier results with the SXR were determined for measurement wavelengths that were calculated as in (14), but with the factor  $\rho(\lambda)$  replaced by the factor  $\rho(\lambda)L_{cs}(\lambda)$ .

The function  $\rho(\lambda)$  was determined from measurements of the SXR channels using the NIST Visible Spectral Comparator Facility (VisSCF) (Larason et al. 1996). The relative spectral responsivity of the SXR could not be determined from separate measurements of the:

- Transmittance of the interference filters and objective lens,
- Responsivity of the detectors, and
- Reflectivity of the wedge mirrors,

because the interference filters are illuminated off-axis, resulting in a shift of the wavelength. It would have been very difficult to measure transmittance and reflectance of these optical components using the same beam geometry and incidence angles as in the SXR. In addition, measuring the components separately and then combining the results to determine the overall relative spectral responsivity does not account for interreflections and scattering.

The primary purpose of the VisSCF is for measurements of the absolute spectral flux responsivity function of photodiodes from 350–1,800 nm. A continuum source

(a 100 W quartz-halogen lamp) is spectrally filtered using a prism-grating monochromator. For the absolute flux measurements, a circular aperture is placed at the exit slit of the monochromator and an image of this aperture is formed with unity magnification using spherical mirrors. Detectors to be calibrated, as well as the working standards, are mounted on translation stages so that the image of the circular aperture underfills the detectors. In addition, a portion of the output is directed to a monitor photodiode. The absolute spectral flux responsivity of the working standards is traceable to the detector standard which is the basis for NIST's radiometric scales, the High-Accuracy Cryogenic Radiometer (HACR, Gentile et al. 1996).

Because the VisSCF is designed for transferring spectral flux responsivity, and the entrance pupils of the detectors are underfilled, the spectral radiance of the VisSCF is not determined, only the radiant flux. In principle, a spatially uniform, lambertian, monochromatic source of known spectral radiance could be used to determine the absolute spectral radiance responsivity of an imaging radiometer, such as the SXR. For this to happen, not only must there be a way to measure the spectral radiance of the monochromatic source, but the entrance pupil of the radiometer must be filled by the source. In the case of the SXR, this would require a source of about 45 mm in diameter or greater, that is lambertian over a solid angle, corresponding to about  $f/2.5$ . With the circular aperture removed from the exit slit of the prism-grating monochromator, the image of the slit (in the plane of the working standards) is  $0.6 \times 0.8$  mm and fills an  $f/8 \times f/16$  solid angle; clearly a poor match for the SXR. This required a modification of the standard procedure at the VisSCF.

Three types of measurements for each channel of the SXR were made. For the first, the flux of the prism-grating monochromator was directed to a 50.8 cm diameter, pressed polytetrafluoroethylene (PTFE) plaque. The bandwidth of the monochromator was set to 1.0 nm and the plaque was located a sufficient distance from the translation stage containing the working standard so that the illuminated area of the plaque was greater than 45 mm in diameter. Then, the SXR was aligned to view the plaque from a distance of about 85 cm, so that the entrance pupil of the SXR was filled by this nearly uniform, lambertian, monochromatic source. The output of the monochromator illuminated the plaque at normal incidence and the SXR viewed the plaque at about  $30^\circ$ . These measurements filled the entrance pupil of the SXR, but resulted in poor signal-to-noise ratios, so that the spectral flux responsivity of only between approximately 10–100% of the maximum of  $\rho(\lambda)$  could be measured; these measurements were made every 0.5 nm.

In order to study the response well away from the peak, the signal-to-noise ratio was improved by increasing the bandwidth of the monochromator to 4 nm, removing the plaque, and aligning the SXR to image the intermediate



image of the exit slit of the prism-grating monochromator. This intermediate image is formed by the VisSCF aft optics. For these measurements, the SXR was located greater than approximately 85 cm from the image of the slit, the aperture stop was filled, but the field stop was underfilled by the beam from the monochromator. Preliminary measurements were made over the entire spectral region where the silicon photodiodes have finite responsivity (350–1,100 nm) and the final measurements were made every 1–2 nm for the region where the spectral responsivity was measurable. For channels 2–6, this wide bandwidth, direct-view configuration saturated the SXR near the maximum of  $\rho(\lambda)$  (the in-band region). Scans were also taken in the direct-view mode but with the bandwidth reduced to 1 nm and a step interval of 0.5 nm.

The original plan to determine  $\rho(\lambda)$  from these three data sets was to use the 1 nm bandwidth PTFE scans for the in-band regions, and the 4 nm bandwidth direct-view scans for the remaining spectral regions, or wings. The 1 nm bandwidth direct-view scans were taken in order to match these two measurements, because most of the 4 nm bandwidth measurements saturated the in-band regions. The poor signal-to-noise ratio of the in-band data acquired with the PTFE plaque resulted in relative standard deviations in  $\rho(\lambda)$  of the order of 1–10%, near the maximum value of  $\rho(\lambda)$ , compared to 0.05% or 0.03% for the direct-view measurements at the same bandwidth (1 nm). Because this measurement precision affects the overall uncertainty of the SXR, the plan was modified.

Conventional theory of interference filters predicts that as the angular extent of the incident flux changes from a collimated beam to one that contains a range of input angles (e.g., for an  $f/16$  beam to an  $f/2.5$  beam), the wavelength shifts to shorter values. Assuming that there is no change in the shape of  $\rho(\lambda)$ , then the ratio  $\rho(\lambda)_{\text{PTFE}}/\rho(\lambda - \delta\lambda)_{\text{dv}}$  (where  $\rho(\lambda)_{\text{PTFE}}$  is  $\rho(\lambda)$  measured with a diffuse plaque and  $\rho(\lambda)_{\text{dv}}$  is  $\rho(\lambda)$  measured with the field of view underfilled, i.e., the direct-view) for the two sets of 1 nm, bandwidth data in the in-band region should be a constant for the correct value for the wavelength shift,  $\delta\lambda$ . For each channel, the wavelength shift was determined using a weighted  $\chi^2$  variable determined using this ratio (Table 9). For the fitting routine, linear interpolation at the trial wavelength was used, but for the final value, a cubic spline interpolation was used. For channels 1–5,  $\delta\lambda$  was between 0.06–0.25 nm, positive as expected, but for channel 6,  $\delta\lambda$  was  $-0.30$  nm. The reason for this discrepancy is not understood, but it agrees with the actual measurements. The results are shown in part a of Figs. 10–15 and the values of  $\delta\lambda$  are given in Table 9.

Once the shifts were determined, the relative spectral response in the in-band region,  $\rho(\lambda - \delta\lambda)_{\text{dv}}$ , 1 nm scans were used for the spectral interval from about  $\pm 12$ –15 nm with respect to the maximum of  $\rho(\lambda)$ . The direct-view, 4 nm scans and their measurement uncertainties were used for the wings. Because the radiant flux from the VisSCF for

both the 1 nm and the 4 nm bandwidth direct-view scans was measured using the working standard detectors, the VisSCF data analysis algorithms result in data sets that can be compared directly. This is not possible for the scans using the plaque, because the working standard detectors do not measure the flux reflected from the plaque. Neglecting the effect of the different bandwidths,  $\rho(\lambda - \delta\lambda)_{\text{dv}}$  acquired using the 1 nm bandwidth should equal  $\rho(\lambda)_{\text{dv}}$  acquired using the 4 nm bandwidth at the same measurement wavelength. Compared to the original plan, this analysis is simpler, because a scale factor relating the plaque to the direct-view measurements does not have to be determined. As a test, and to provide additional data points in the matching regions, the 1 nm direct-view data were convolved with a triangular slit function with a full-width at half-maximum of 4 nm to make them compatible with the 4 nm direct-view data. The agreement was satisfactory, about  $\pm 20\%$ . The final results for  $\rho(\lambda)$  are shown in part b of Figs. 10–15. The location of the matching of the wing and the in-band data is evident from the discontinuities in the uncertainties as a function of wavelength.

Although not stated explicitly in the SXR measurement equations, it is useful to calculate the spectral bandwidth for comparing it to other instruments. Two methods were used to determine the SXR bandwidths, using the values for  $\rho(\lambda)$ . The bandwidth is defined as

$$\Delta\lambda_s = \frac{\int \lambda \rho(\lambda) d\lambda}{\rho(\lambda_m)}, \quad (15)$$

where the maximum value for  $\rho(\lambda_m)$  is unity, which makes  $\Delta\lambda_s$  equivalent to the width of a square wave relative spectral response

Assuming a Gaussian profile for  $\rho(\lambda_m)$ ,  $\Delta\lambda_g$ , the full-width at half-maximum is proportional to the square root of the second moment,

$$\Delta\lambda_g = 2.345 \left( \frac{\int \rho(\lambda) (\lambda - \lambda_m)^2 d\lambda}{\int \rho(\lambda) d\lambda} \right)^{1/2}. \quad (16)$$

The results are compared in Table 9.

The two methods for deriving  $\rho(\lambda_m)$ , using either the PTFE plaque data or the application of a wavelength shift to the direct view data, were compared as a verification of the latter method. The former method was used to determine the SXR parameters in earlier work (e.g., Johnson et al. 1997). Using (14), the values for  $\lambda_m$  (using the two methods) agreed to within  $\pm 0.015$  nm for channels 3, 4, and 5. For channels 1, 2, and 6, the final measurement wavelengths ( $\lambda_m$ ) are 0.03 nm, 0.10 nm, and 0.05 nm greater than those determined using the PTFE plaque data. For channel 2, the difference can be explained in terms of the improper matching of the wing data to the PTFE in-band data. The wavelength shift method resulted in an increase in the relative spectral responsivity in the



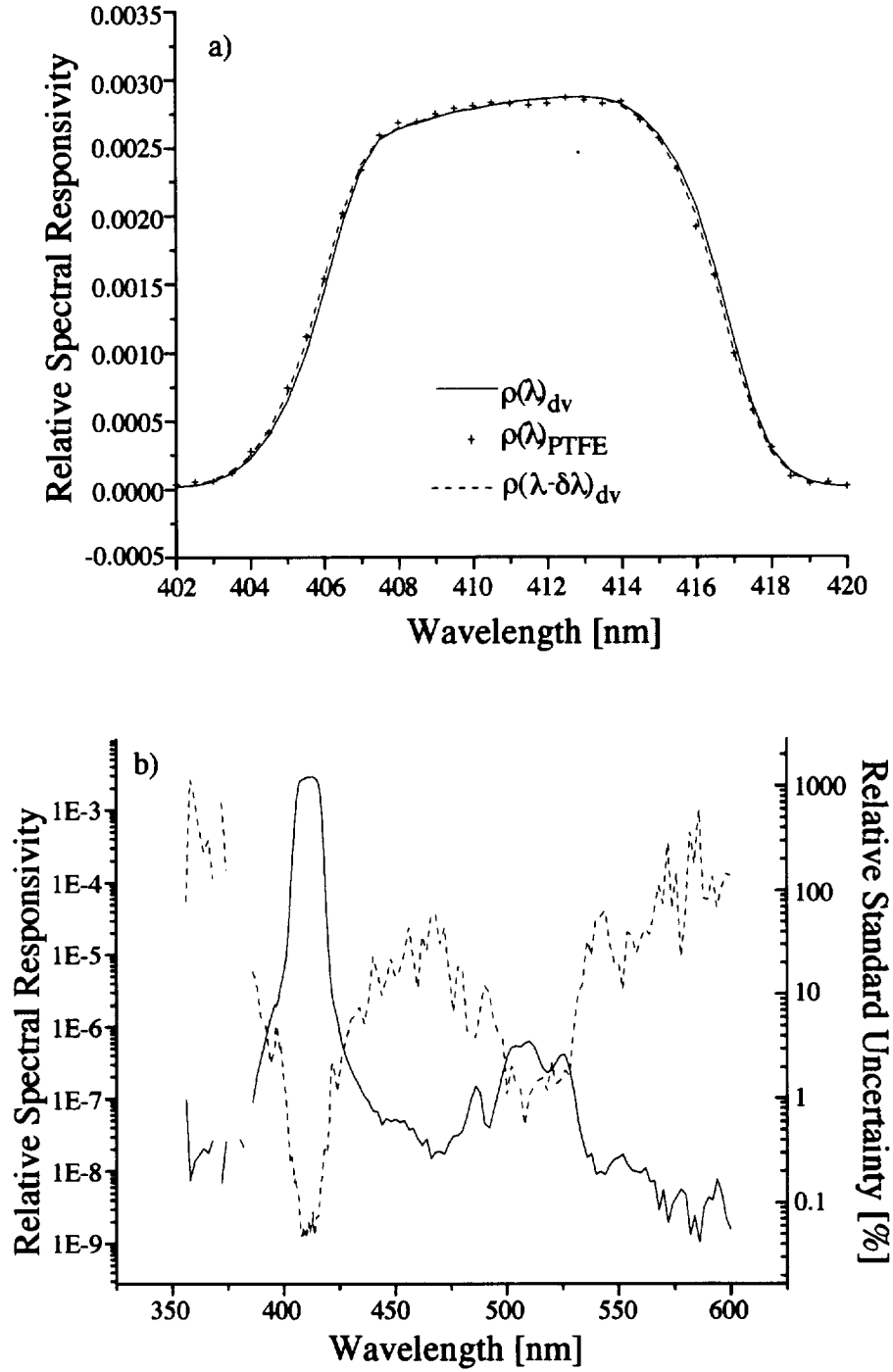


**Fig. 10.** Relative spectral responsivity,  $\rho(\lambda)$ , for channel 1 of the SXR. a) For the in-band spectral region,  $\rho(\lambda)_{dv}$  and  $\rho(\lambda)_{PTFE}$  are shown as a solid line and the cross symbol. The dashed line,  $\rho(\lambda - \delta\lambda)_{dv}$ , was used for the final values. b) The entire spectral region is shown where  $\rho(\lambda)$ , from 350–600 nm, is depicted with the solid line. Negative values are not plotted and occur at the location of the breaks in the solid line. The relative standard uncertainty,  $u_{\rho(\lambda)}/\rho(\lambda)$ , a Type A value, is shown as the dashed line in units of percent. The feature at about 510 nm is 0.045% of the value at 411.22 nm.

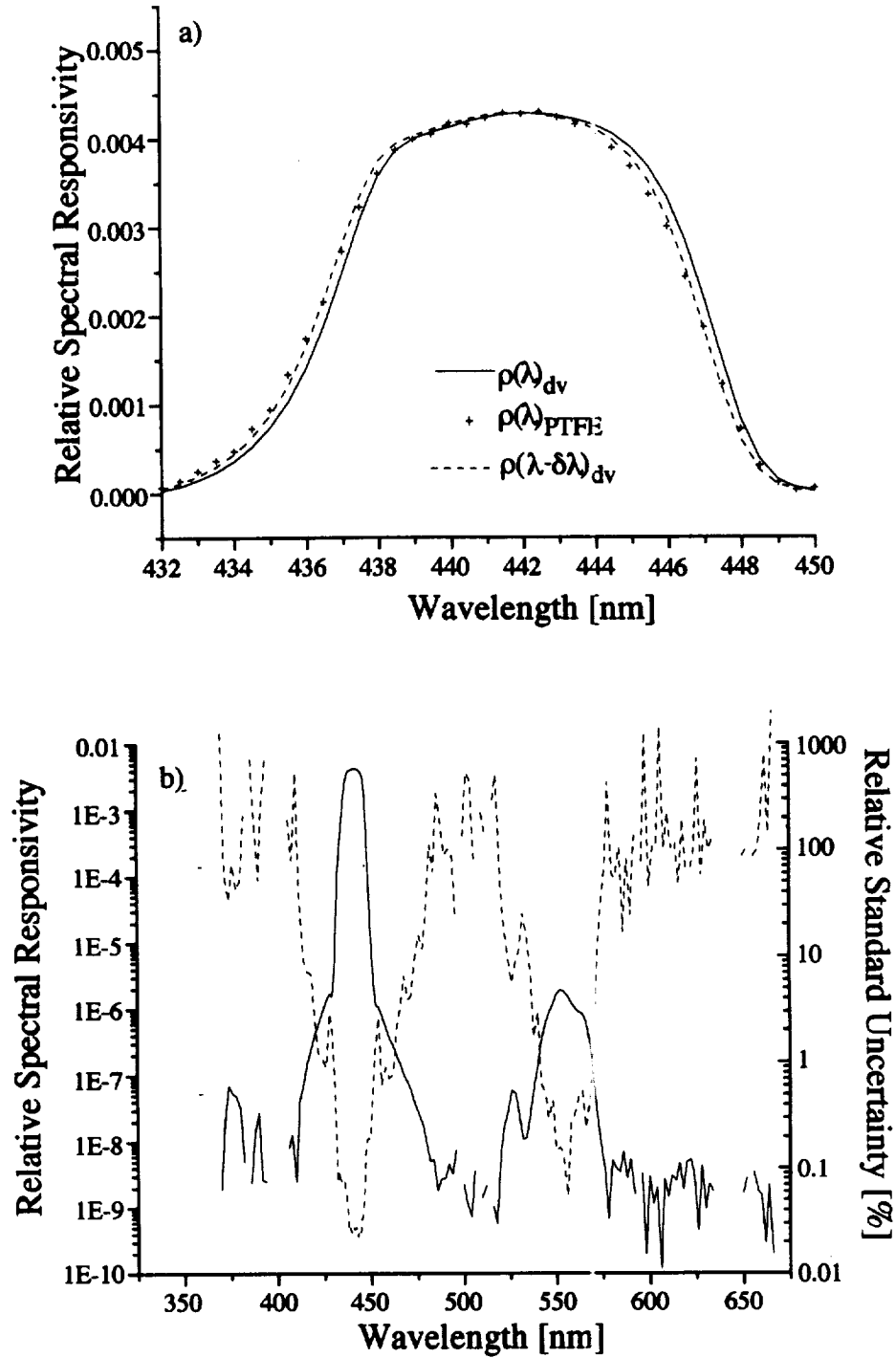


**Fig. 11.** Relative spectral responsivity,  $\rho(\lambda)$ , for channel 2 of the SXR. a) For the in-band spectral region,  $\rho(\lambda)_{dv}$  and  $\rho(\lambda)_{PTFE}$  are shown as a solid line and the cross symbol. The dashed line,  $\rho(\lambda - \delta\lambda)_{dv}$ , was used for the final values. b) The entire spectral region is shown where  $\rho(\lambda)$ , from 350–675 nm, is depicted with the solid line. Negative values are not plotted and occur at the location of the breaks in the solid line. The relative standard uncertainty,  $u_{\rho(\lambda)}/\rho(\lambda)$ , a Type A value, is shown as the dashed line in units of percent. The feature at about 552 nm is 0.046% of the value at 441.5 nm.

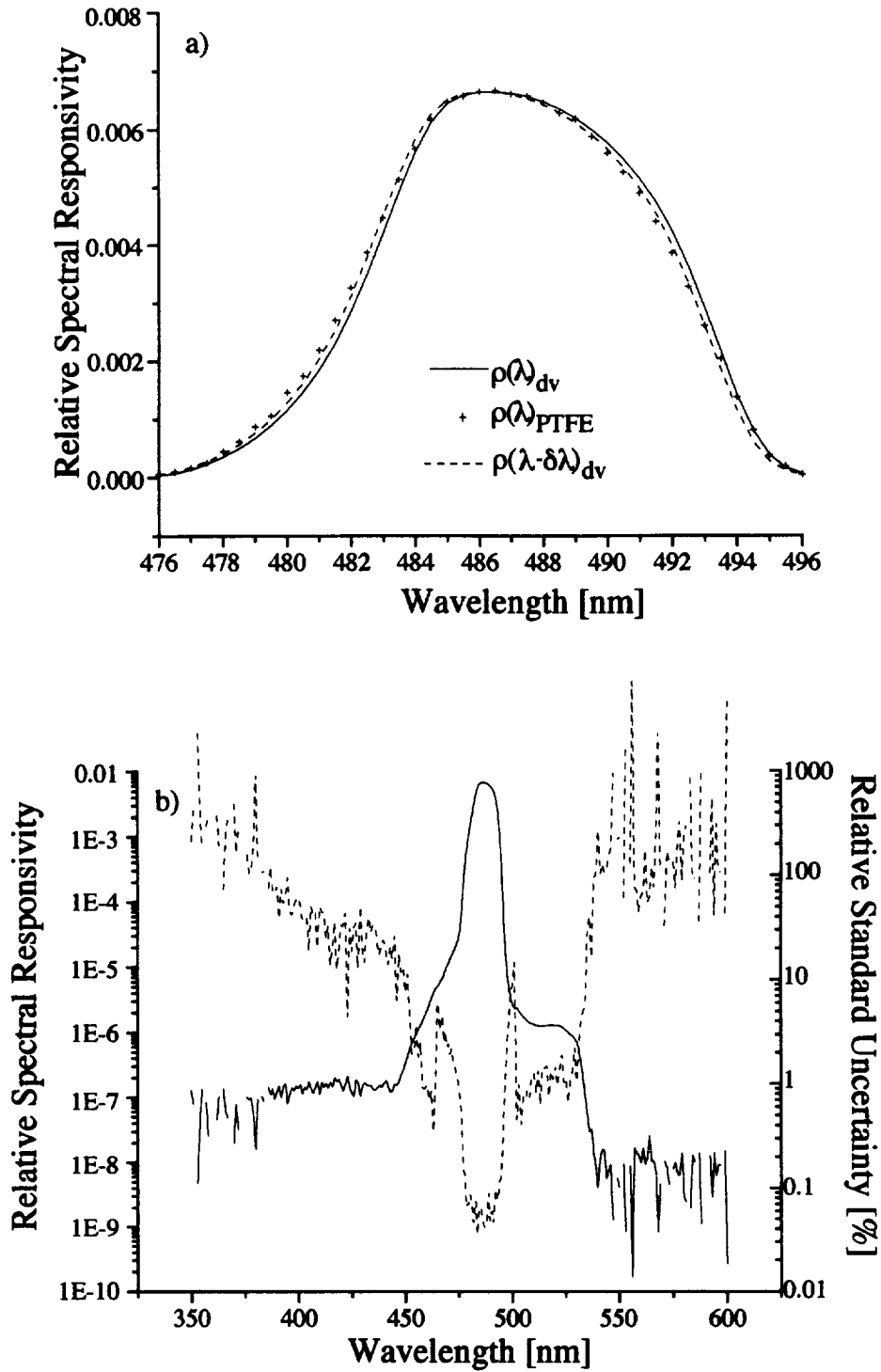


**Fig. 12.** Relative spectral responsivity,  $\rho(\lambda)$ , for channel 3 of the SXR. a) For the in-band spectral region,  $\rho(\lambda)_{dv}$  and  $\rho(\lambda)_{PTFE}$  are shown as a solid line and the cross symbol. The dashed line,  $\rho(\lambda - \delta\lambda)_{dv}$ , was used for the final values. b) The entire spectral region is shown where  $\rho(\lambda)$ , from 350–600 nm, is depicted with the solid line. Negative values are not plotted and occur at the location of the breaks in the solid line. The relative standard uncertainty,  $u_{\rho(\lambda)}/\rho(\lambda)$ , a Type A value, is shown as the dashed line in units of percent. The shoulder, at about 518 nm, is 0.02% of the value at 486.94 nm.

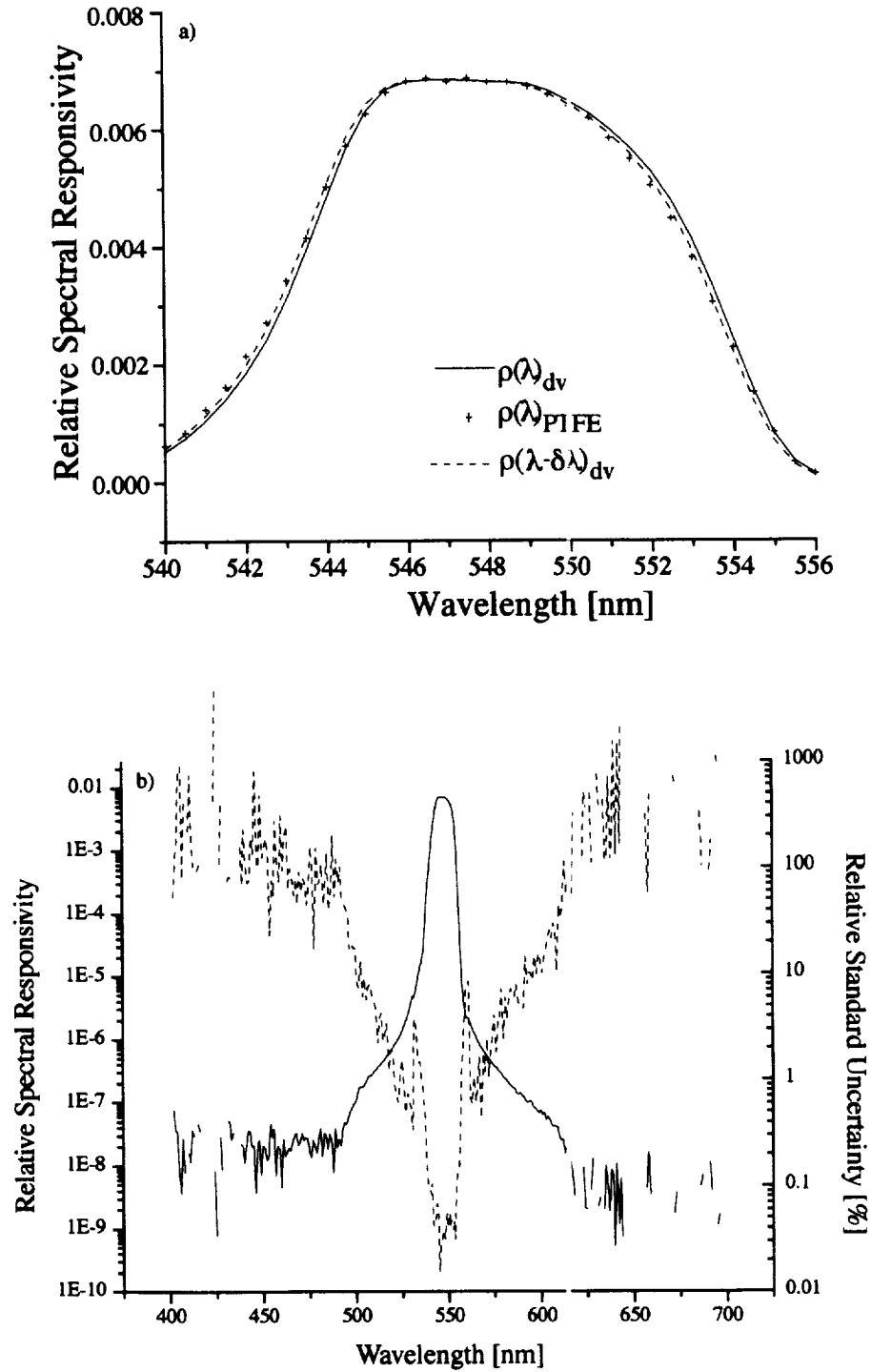


**Fig. 13.** Relative spectral responsivity,  $\rho(\lambda)$ , for channel 4 of the SXR. **a)** For the in-band spectral region,  $\rho(\lambda)_{dv}$  and  $\rho(\lambda)_{PTFE}$  are shown as a solid line and the cross symbol. The dashed line,  $\rho(\lambda - \delta\lambda)_{dv}$ , was used for the final values. **b)** The entire spectral region is shown where  $\rho(\lambda)$ , from 400–700 nm, is depicted with the solid line. Negative values are not plotted and occur at the location of the breaks in the solid line. The relative standard uncertainty,  $u_{\rho(\lambda)}/\rho(\lambda)$ , a Type A value, is shown as the dashed line in units of percent.

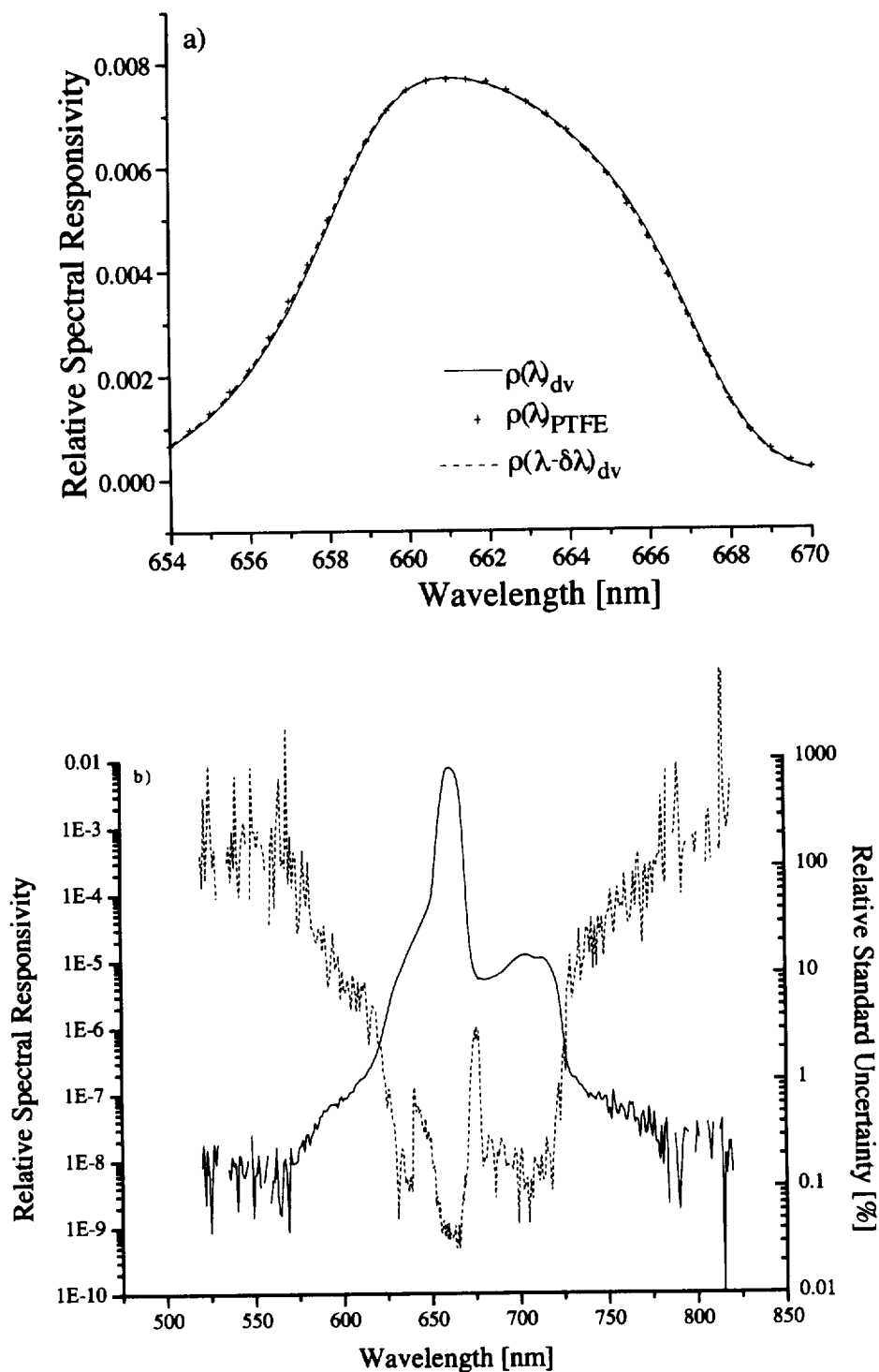


**Fig. 14.** Relative spectral responsivity,  $\rho(\lambda)$ , for channel 5 of the SXR. a) For the in-band spectral region,  $\rho(\lambda)_{dv}$  and  $\rho(\lambda)_{PTFE}$  are shown as a solid line and the cross symbol. The dashed line,  $\rho(\lambda - \delta\lambda)_{dv}$ , was used for the final values. b) The entire spectral region is shown where  $\rho(\lambda)$ , from 520–820 nm, is depicted with the solid line. Negative values are not plotted and occur at the location of the breaks in the solid line. The relative standard uncertainty,  $u_{\rho(\lambda)}/\rho(\lambda)$ , a Type A value, is shown as the dashed line in units of percent. The feature at about 700 nm is 0.16% of the value at 661.72 nm.

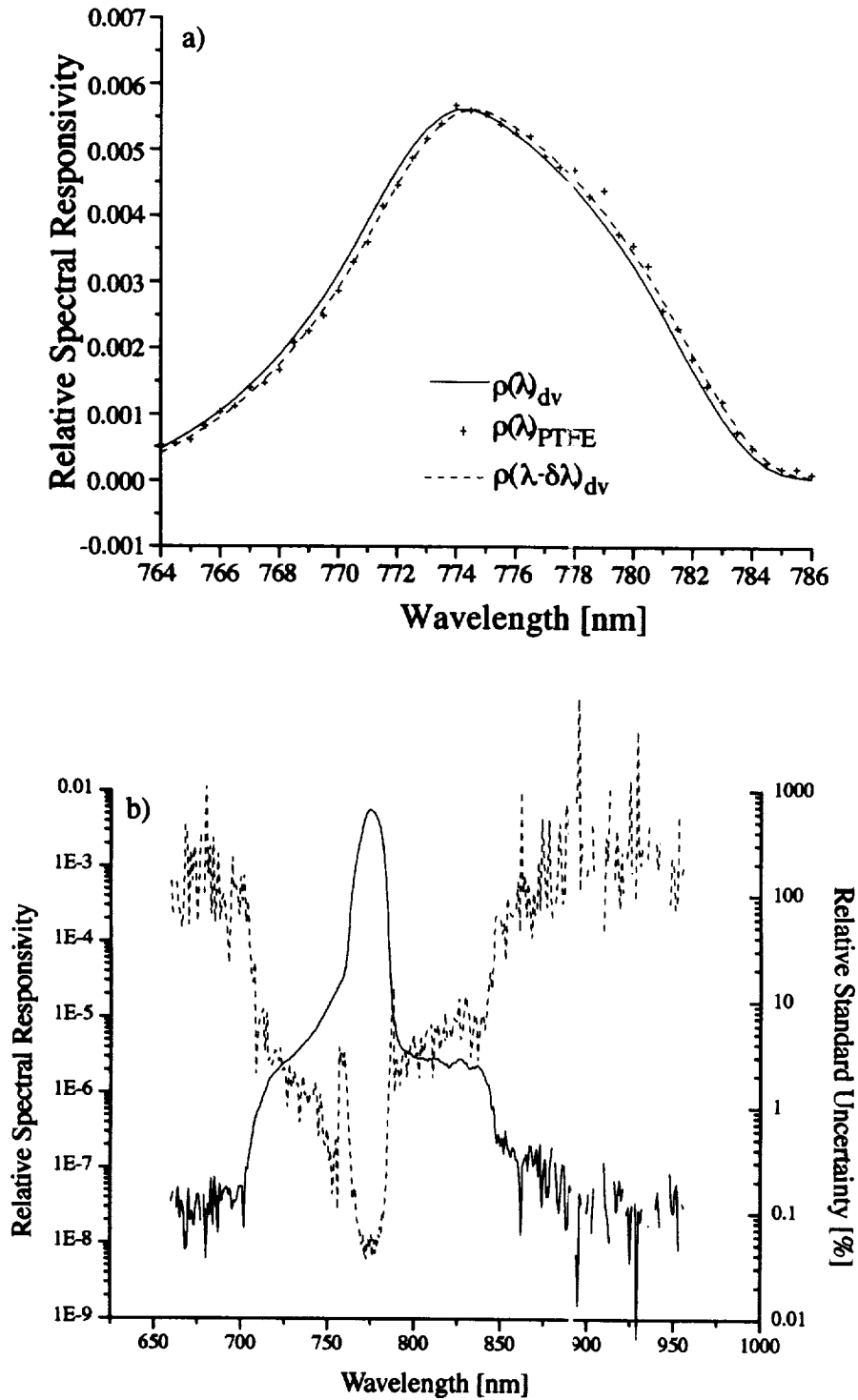


**Fig. 15.** Relative spectral responsivity,  $\rho(\lambda)$ , for channel 6 of the SXR. a) For the in-band spectral region,  $\rho(\lambda)_{dv}$  and  $\rho(\lambda)_{PTFE}$  are shown as a solid line and the cross symbol. The dashed line,  $\rho(\lambda - \delta\lambda)_{dv}$ , was used for the final values. b) The entire spectral region is shown where  $\rho(\lambda)$ , from 660–960 nm, is depicted with the solid line. Negative values are not plotted and occur at the location of the breaks in the solid line. The relative standard uncertainty,  $u_{\rho(\lambda)}/\rho(\lambda)$ , a Type A value, is shown as the dashed line in units of percent. The feature at about 820 nm is 0.05% of the value at 774.77 nm.

**Table 9.** Results (in nanometers) of the analysis of relative spectral responsivity measurements for the SXR.

Channel	$\delta\lambda$	$\lambda_m$	$u_{\lambda_m}$	$\Delta\lambda_s$	$\Delta\lambda_g$
1	0.0867	411.222	0.054	10.718	9.604
2	0.251	441.495	0.054	10.364	10.394
3	0.211	486.938	0.053	10.526	9.148
4	0.133	547.873	0.054	10.359	8.370
5	0.0569	661.718	0.054	9.581	11.451
6	-0.301	774.767	0.053	11.508	12.791

wings by a factor of about 3.7. (For all of the other channels, this ratio for the two methods was between 0.98 and 1.4.)

The standard uncertainties in  $\lambda_m$ ,  $u_{\lambda_m}$ , in Table 9 for each SXR channel are the quadrature sum of two separate components: measurement uncertainty, and uncertainty in the wavelength shift of spectral responsivity, which was estimated to be 0.05 nm. The measurement uncertainty resulted in an uncertainty of about 0.02 nm and was calculated by propagating the standard deviations of the raw data from the VisSCF measurements. The values were determined by approximating the integrals in the equation for  $\lambda_m$  as sums:

$$\lambda_m = \frac{\sum \lambda_i \rho(\lambda_i) (\lambda_{i+1} - \lambda_i)}{\sum \rho(\lambda_i) (\lambda_{i+1} - \lambda_i)}, \quad (17)$$

where  $\lambda_i$  is a discrete wavelength. The combined standard uncertainty, therefore, is

$$u_{\lambda_m}^2 = \sum \left( u_{\lambda}^2 \left( \frac{\partial \lambda_m}{\partial \lambda_i} \right)^2 \right) + \sum \left( u_{\rho(\lambda_i)}^2 \left( \frac{\partial \lambda_m}{\partial \rho(\lambda_i)} \right)^2 \right) + 0.05^2. \quad (18)$$

To evaluate (18), the standard uncertainty in the wavelength accuracy ( $u_{\lambda}$ ) of the Cary-14 monochromator in the VisSCF was taken to be 0.1 nm, independent of wavelength, and the standard uncertainty in the relative spectral responsivity,  $u_{\rho(\lambda)}$ , was calculated using the standard deviation on the measurements (part b of Figs. 10–15). The uncertainty in the wavelength step was assumed to be negligible. For equal steps,  $\lambda_{i+1} - \lambda_i$  equal to a constant, (18) is

$$u_{\lambda_m}^2 = \frac{u_{\lambda}^2 \sum \rho(\lambda_i)^2}{(\sum \rho(\lambda_i))^2} + \frac{\sum u_{\rho(\lambda)}^2 \lambda_i^2 - 2\lambda_m \sum u_{\rho(\lambda)}^2 \lambda_i + \lambda_m^2 \sum u_{\rho(\lambda)}^2}{(\sum \rho(\lambda_i))^2} + 0.05^2. \quad (19)$$

The spectral responsivity functions for the SXR exhibit finite responsivity outside of the bandwidth, with regions of increased responsivity on the long wavelength side of  $\lambda_m$  in most cases. This is because of finite transmittance in the interference filters. From part b of Figs. 10–15, the responsivity at selected spectral intervals is between  $10^{-3}$  and  $10^{-4}$  of the value at  $\lambda_m$ . To quantify this effect, the ratio of in-band spectral responsivity ( $R_{IB}$ ) to total spectral responsivity ( $R_{Tot}$ ) is given as

$$\frac{R_{IB}}{R_{Tot}} = \frac{\int_{\lambda-\Delta\lambda_s}^{\lambda+\Delta\lambda_s} \rho(\lambda) d\lambda}{\int_{\lambda_{min}}^{\lambda_{max}} \rho(\lambda) d\lambda}, \quad (20)$$

where  $\lambda_{min}$  and  $\lambda_{max}$  correspond to the minimum and maximum extremes, respectively, of the measurements in the VisSCF. The value of the ratio is between 0.9963 (channel 3) and 0.9987 (channel 2 and 6).

The spectral correction factor,  $k_{\lambda}$ , cannot be determined in advance of a particular measurement because it depends on the source radiance. However, this factor can be estimated using Planck's law and different radiance temperatures to approximate the spectral shape of a calibration source. The reference source,  $L_{cs}(\lambda)$  in (13), was assumed to have an effective radiance temperature of 2,856 K, and the affect of measuring a source with an effective radiance temperature of 2,000 K and 3,200 K, is shown in Table 10. The channels at the shorter measurement wavelengths are more sensitive to the relative spectral shape of the source, resulting in a correction of up to 0.6% for these examples.

**Table 10.** Values of  $k_{\lambda}$ , for measuring sources with a relative spectral shape (as indicated) if the SXR was calibrated using a source with the same relative spectral shape as a blackbody at 2,856 K.

Channel	$\lambda_m$	$k_{\lambda}(2,000 \text{ K})$	$k_{\lambda}(3,200 \text{ K})$
1	411.222	0.9940	1.0008
2	441.495	0.9951	1.0006
3	486.938	0.9982	1.0003
4	547.873	0.9991	1.0001
5	661.718	0.9994	1.0000
6	774.767	0.9997	1.0000

### 3.2.3 Relative Spatial Response

Assuming that the sources are uniform and lambertian, the spatial portion of the calibration correction factor is

$$k_a = \frac{\int_{A_{cs}} h(x, y) dx dy}{\int_{A_{ms}} h(x, y) dx dy}, \quad (21)$$

where  $A_{cs}$  is the calibration source area, and  $A_{ms}$  is the measured source area; the assumptions are stated in Sect. 3.1.1.

The function  $h(x, y)$  for each channel of the SXR was measured on several occasions with different distances between the entrance window and the entrance pupil (the objective lens was focused at the corresponding distance) using a small lamp, a pair of automated  $x, y$  translation stages, and a computer system for data acquisition and control. The halogen lamps used had a small filament, about 1 mm × 2 mm, and low wattage, less than 10 W. Using two translation stages, the lamp was scanned in the plane containing the entrance window of the SXR and data were recorded at each location using an HP 3457A DMM, the Institute of Electrical and Electronic Engineers (IEEE)-488.2 interface protocol, a PC, and a custom data acquisition program written in Visual Basic.

Some measurements for channel 6 were made by moving the SXR with the lamp in a fixed position. An HP power supply was used to operate the lamp in the constant current mode of operation, but no attempt was made to further stabilize the current in the lamp, i.e., through computer control. Each measurement consisted of visually centering the lamp in the SXR's field of view, noting the position of the translation stages, and then determining the location where the signal was a maximum. The current in the lamp was adjusted so that the amplifier was not saturated; typically, this maximum signal was between 9–12.5 V DC, and then this value, as well as the value at the center location, was recorded. A single gain setting for the voltage amplifier in the SXR was used for the entire scan. The background was recorded at the beginning and the end of the scan, as were the lamp settings and the signal at the central and *maximum* position. Most of the measurements consisted of a square area, 400 mm on a side, with a step size of 3.2 mm. It took about 16 hours to complete the measurements for a single channel, with the DMM integrating over 10 power line cycles for each reading. The SXR was orientated in the E position for these measurements. For channel 6, measurements were also made over a square area 580 mm on a side, with a step size of 4.64 mm, and the SXR was in the W position.

For accurate results for  $h(x, y)$  using this technique, the lamp should behave as a point source, providing uniform irradiance at the entrance pupil of the SXR. The distance between the lamp and the SXR was greater than 100 times the size of the lamp filament, so the point source assumption was valid. The lamp should be stable during the

course of the experiment. As measured before and after the scan, the repeated measurements of the lamp output agreed to better than 0.5%, so it was valid to normalize the final results without correcting for lamp drift.

It is also important to control the amount of scattered light. To meet this condition, the lamp was mounted at the end of a long rod, which was covered with black tape, and the assembly was mounted horizontally onto the translation stage assembly. A uniform, black surface was mounted vertically at the end of the rod to cover the components of the translation stages that were near the lamp. Finally, the amplifier offset voltage, or background signal, must be constant over the entire scan, because a single average value must be subtracted from the raw data to determine  $h(x, y)$ . As measured at a lower corner of the measured area before and after the scan, the repeated measurements of the background signal agreed to about 10%, and the uncertainty in the determination of the background dominates the calculation of the uncertainty in  $k_a$ .

The raw data are presented as contour plots, with emphasis on the out-of-field portions of the SXR's field of view, in part a of Figs. 16–21, and as contour plots of the central portion of the field of view in part b of Figs. 16–21. Note that the shape and orientation of the spatial response function in these figures agree with the description of the mechanical layout in Sect. 2.2 and the discussion of the optical system in Sect. 2.1.1.

For measurements of channel 6, when the SXR was mounted to the translation stage assembly, the horizontal lamp rod was supported by a vertical rod, and this surface is visible in the  $h(x, y)$  data (Fig. 21a).

Visual inspection of each image was used to identify three areas of uniform response which best represented the background signal,  $b$ . The average and the standard deviation of the signal in these areas were determined and used to estimate the lower and upper bounds for the background,  $b_-$  and  $b_+$ , respectively. Then, the average background,  $\langle b \rangle = (b_- + b_+)/2$ , was subtracted from the raw data. These data were summed, beginning with the matrix element that corresponded to the maximum net signal. Except for the center element, the area for each sum was square, with a width and height of  $(2n + 1)P$ , where  $n$  is an integer and  $P$  is the step size in point-spread response measurements of the translation stages (the same step size was used for both the horizontal and vertical directions). The size of the final area was determined by the size of the scan and the location of the center element. Finally, the sums for each area were normalized by the sum for the final area (with a half-width of  $r_{max}$ ) and the results plotted as a function of radius, with  $r = nP$ . This procedure was repeated using  $b_-$  and  $b_+$ . These normalized sums are plotted in part c of Figs. 16–21.

These normalized sums correspond to

$$\frac{\int_A h(x, y) dx dy}{\int_{A_{max}} h(x, y) dx dy} \approx p_0 + p_1 r + p_2 r^2, \quad (22)$$



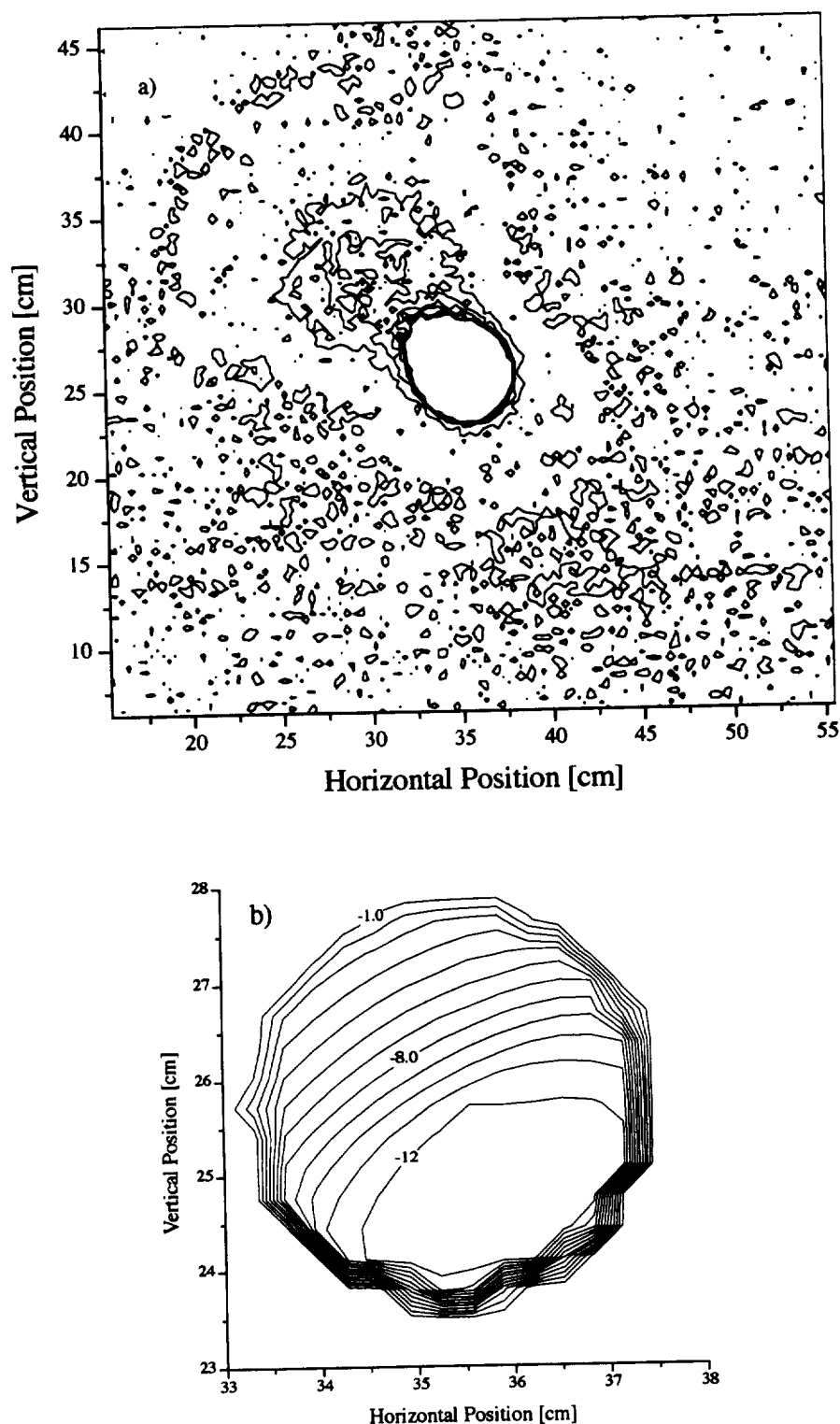


**Fig. 16.** Relative spatial responsivity,  $h(x, y)$ , for channel 1 of the SXR, which was on gain 100. a) A contour plot of data, in non-uniform increments, to emphasize the out-of-field response. The increments between the contours in the out-of-field region are 2.2 mV, 1.5 mV, and 1.1 mV. b) A contour plot of data, in 1 V increments, to illustrate the in-field response. The non-uniformity within the field of view is because of vignetting.

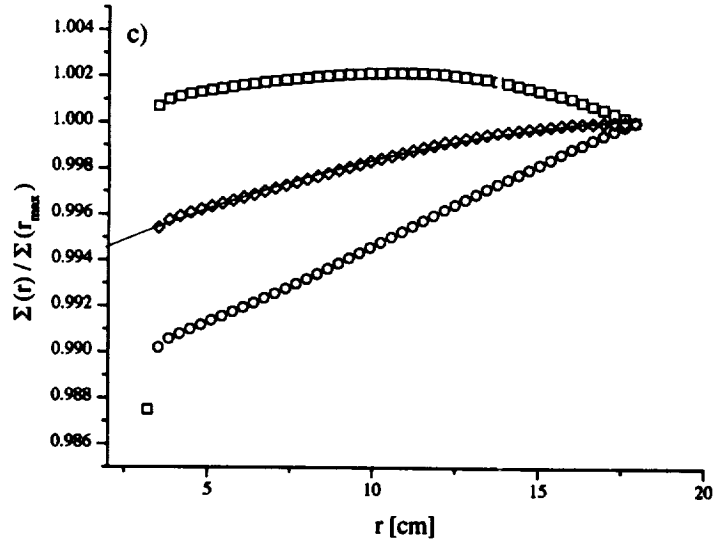


**Fig. 16. (cont.)** Relative spatial responsivity,  $h(x, y)$ , for channel 1 of the SXR, which was on gain 100. c) The normalized and integrated net signals are determined using a background of  $\langle b \rangle = 5.773$  mV. The area used for the normalization was 35.84 cm square. The open diamonds, squares, and circles correspond to  $\langle b \rangle$ ,  $b_-$  (5.268 mV), and  $b_+$  (6.279 mV), respectively. The solid line is a quadratic fit to the normalized sums using  $\langle b \rangle$  for  $r > 4.16$  cm.

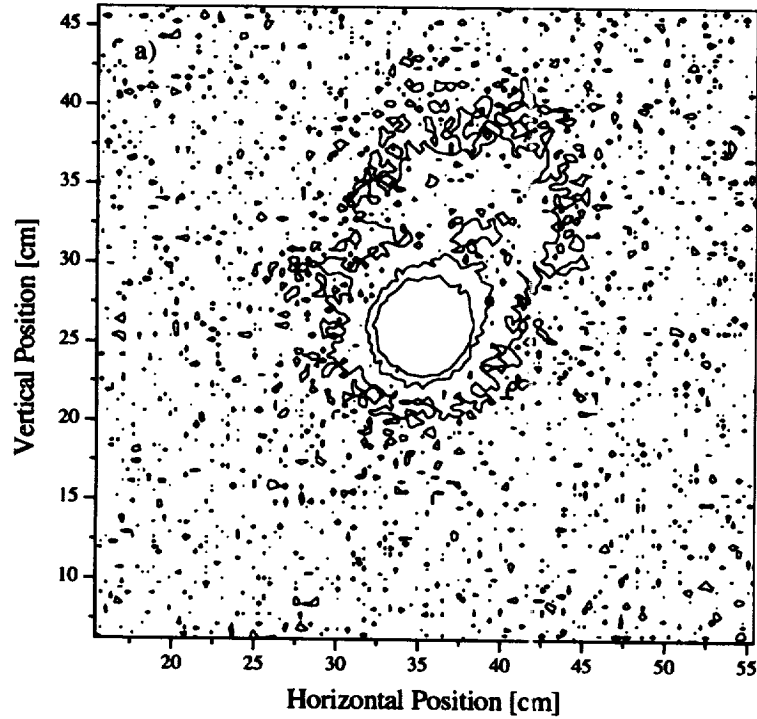


**Fig. 17.** Relative spatial responsivity,  $h(x, y)$ , for channel 2 of the SXR, which was on gain 1,000. a) A contour plot of data, in non-uniform increments, to emphasize the out-of-field response. The increments between the contours in the out-of-field region are 0.80 mV, 0.97 mV, and 1.2 mV.

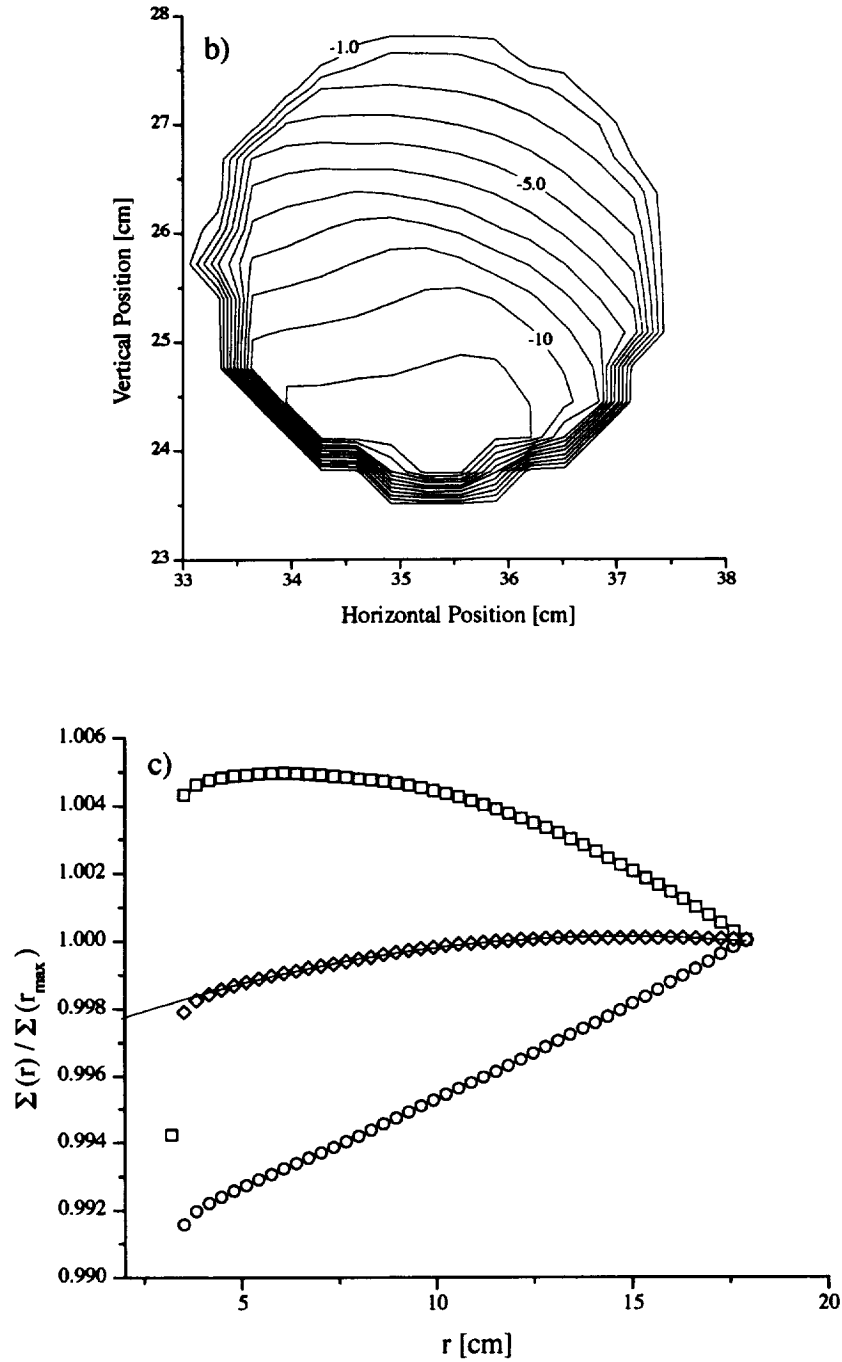


**Fig. 17. (cont.)** Relative spatial responsivity,  $h(x, y)$ , for channel 2 of the SXR, which was on gain 1,000. **b)** A contour plot of data, in 1 V increments, to illustrate the in-field response. The non-uniformity within the field of view is because of vignetting. **c)** The normalized and integrated net signals are determined using a background of  $\langle b \rangle = -6.440$  mV. The area used for the normalization was 35.84 cm square. The open diamonds, squares, and circles correspond to  $\langle b \rangle$ ,  $b_-$  ( $-6.943$  mV), and  $b_+$  ( $-5.398$  mV), respectively. The solid line is a quadratic fit to the normalized sums using  $\langle b \rangle$  for  $r > 4.16$  cm.

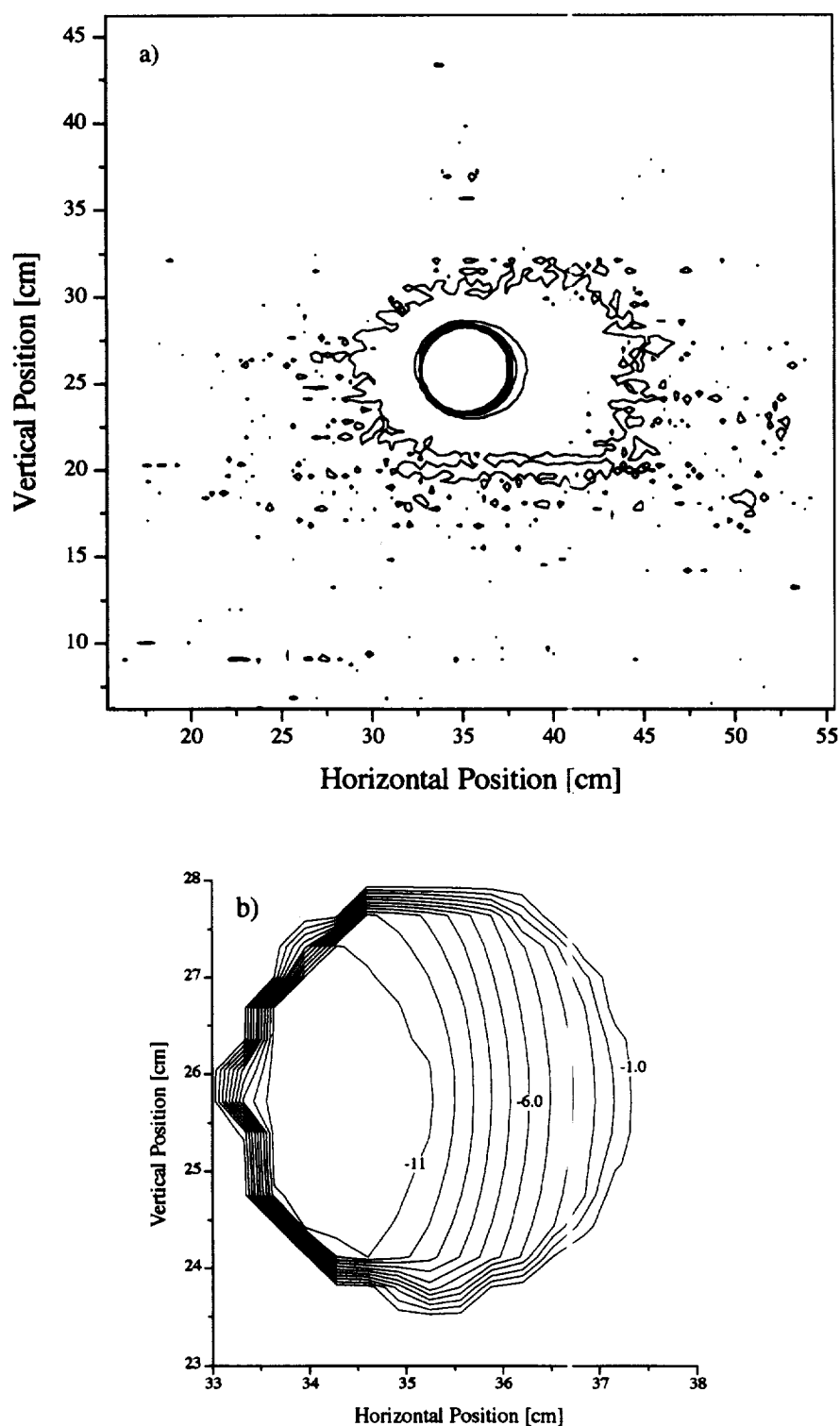


**Fig. 18.** Relative spatial responsivity,  $h(x, y)$ , for channel 3 of the SXR, which was on gain 100. a) A contour plot of data, in non-uniform increments, to emphasize the out-of-field response. The increments between the contours in the out-of-field region are 2.7 mV, 2.8 mV, and 3.0 mV. b) A contour plot of data, in 1 V increments, to illustrate the in-field response. The non-uniformity within the field of view is because of vignetting.

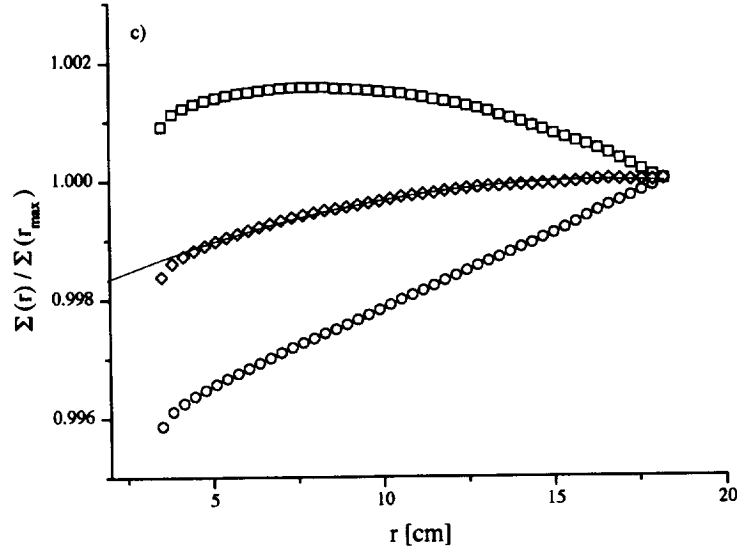


**Fig. 18. (cont.)** Relative spatial responsivity,  $h(x, y)$ , for channel 3 of the SXR, which was on gain 100. **c)** The normalized and integrated net signals are determined using a background of  $\langle b \rangle = -69.036$  mV. The area used for the normalization was 36.48 cm square. The open diamonds, squares, and circles correspond to  $\langle b \rangle$ ,  $b_-$  ( $-69.251$  mV), and  $b_+$  ( $-68.822$  mV), respectively. The solid line is a quadratic fit to the normalized sums using  $\langle b \rangle$  for  $r > 4.16$  cm.

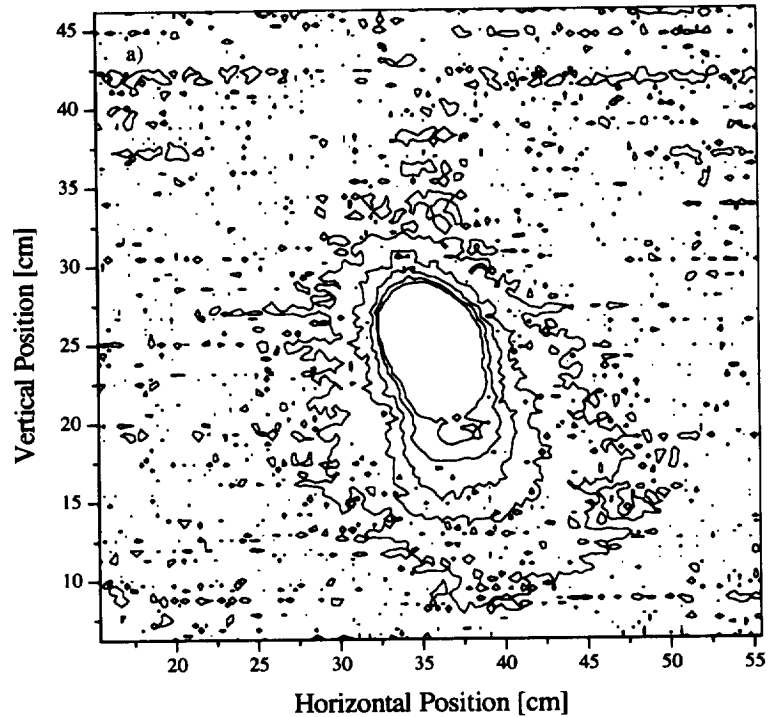


**Fig. 19.** Relative spatial responsivity,  $h(x, y)$ , for channel 4 of the SXR, which was on gain 100. **a)** A contour plot of data, in non-uniform increments, to emphasize the out-of-field response. The increments between the contours in the out-of-field region are 0.44 mV, 0.47 mV, and 0.50 mV.

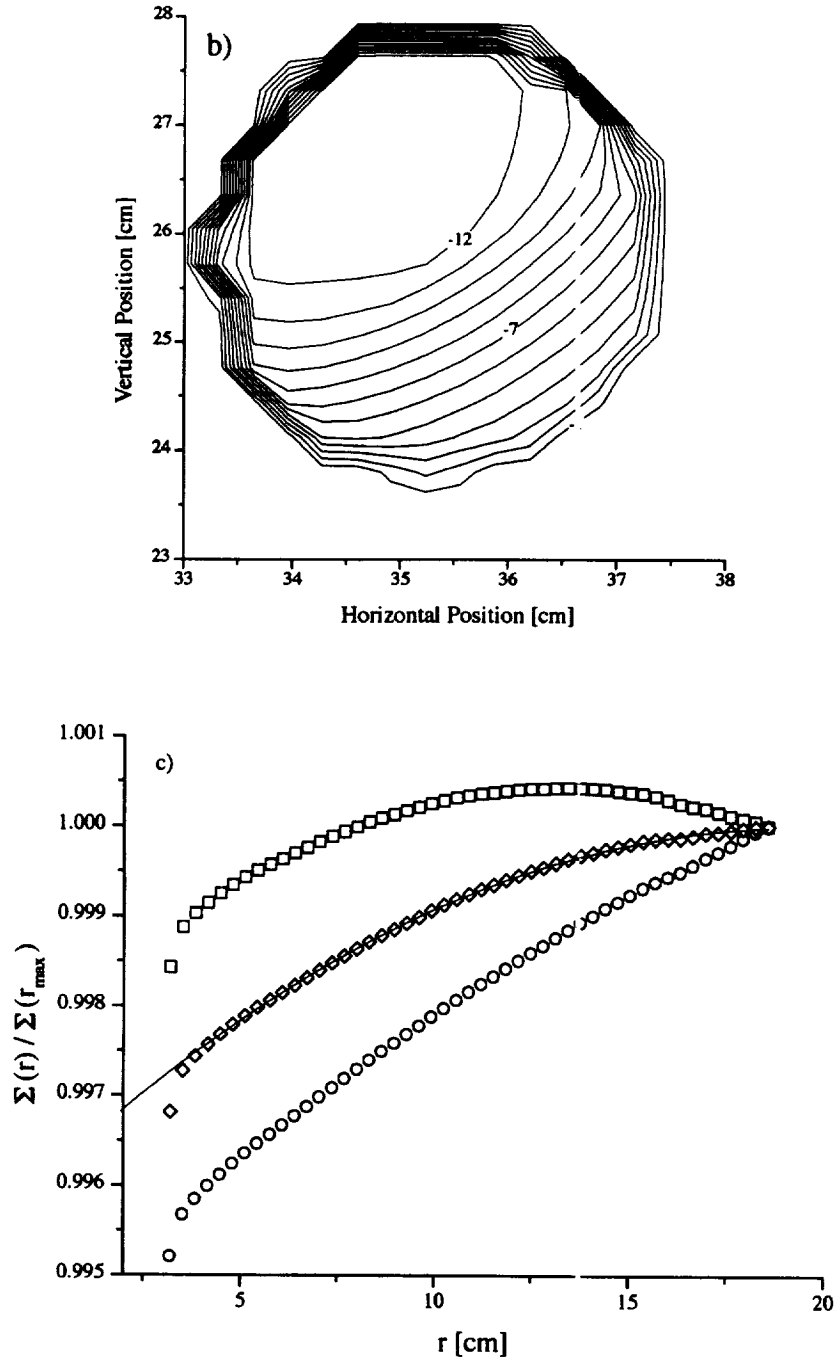


**Fig. 19. (cont.)** Relative spatial responsivity,  $h(x, y)$ , for channel 4 of the SXR, which was on gain 100. b) A contour plot of data, in 1 V increments, to illustrate the in-field response. The non-uniformity within the field of view is because of vignetting. c) The normalized and integrated net signals are determined using a background of  $\langle b \rangle = -7.493$  mV. The area used for the normalization was 37.12 cm square. The open diamonds, squares, and circles correspond to  $\langle b \rangle$ ,  $b_-$  (-7.344 mV), and  $b_+$  (-7.642 mV), respectively. The solid line is a quadratic fit to the normalized sums using  $\langle b \rangle$  for  $r > 4.16$  cm.

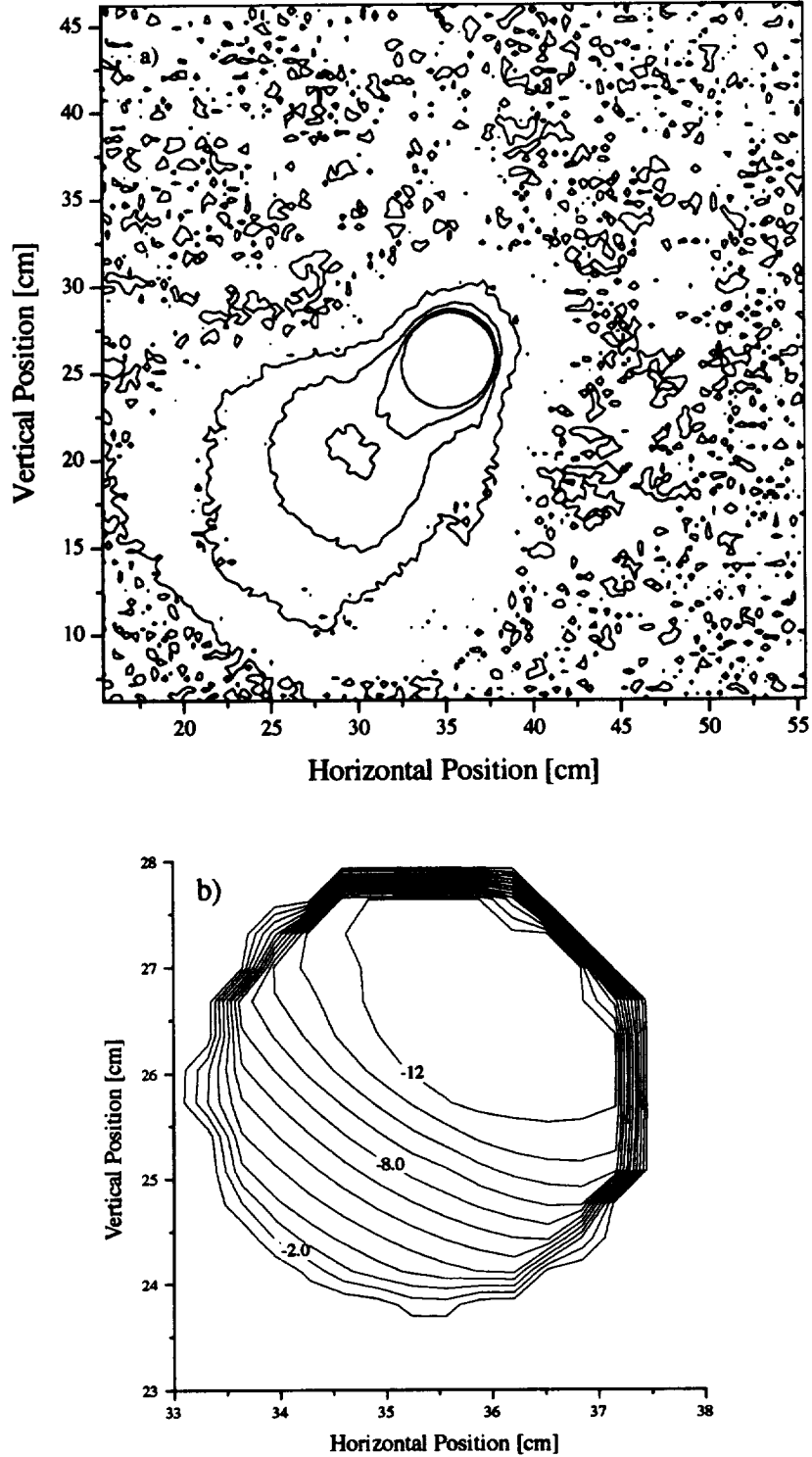


**Fig. 20.** Relative spatial responsivity,  $h(x, y)$ , for channel 5 of the SXR, which was on gain 100. a) A contour plot of data, in non-uniform increments, to emphasize the out-of-field response. The increments between the contours in the out-of-field region are 0.53 mV, 0.87 mV, and 1.4 mV. b) A contour plot of data, in 1 V increments, to illustrate the in-field response. The non-uniformity within the field of view is because of vignetting.

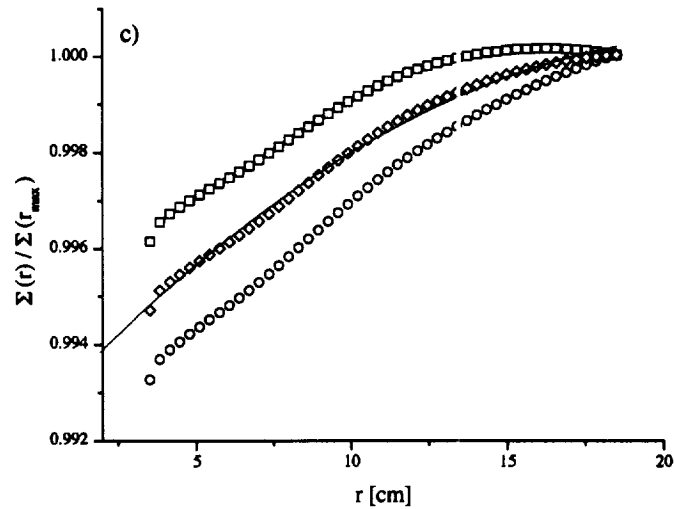


**Fig. 20. (cont.)** Relative spatial responsivity,  $h(x, y)$ , for channel 5 of the SXR, which was on gain 100. c) The normalized and integrated net signals are determined using a background of  $\langle b \rangle = -1.2402$  mV. The area used for the normalization was 37.12 cm square. The open diamonds, squares, and circles correspond to  $\langle b \rangle$ ,  $b_-$  ( $-1.3724$  mV), and  $b_+$  ( $-1.1081$  mV), respectively. The solid line is a quadratic fit to the normalized sums using  $\langle b \rangle$  for  $r > 3.52$  cm.

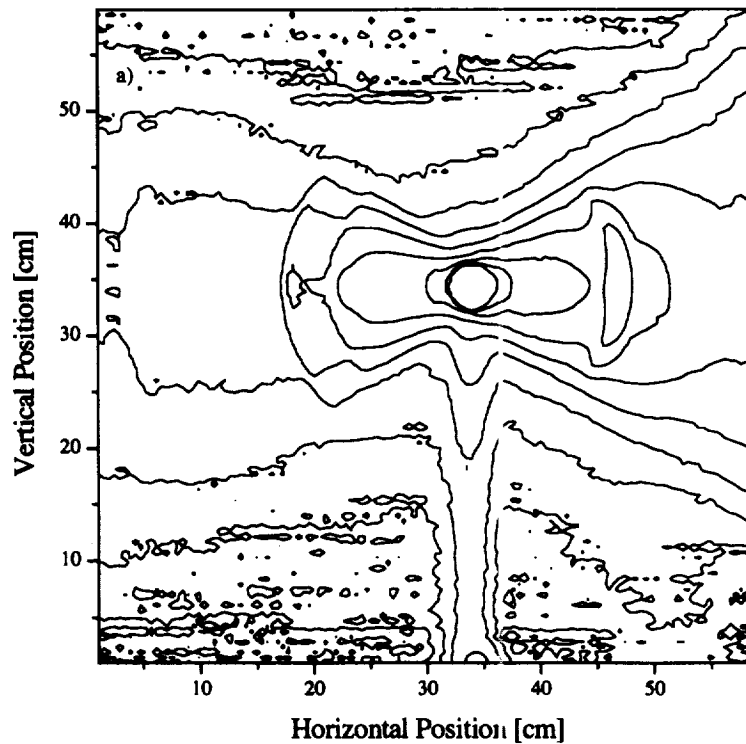


**Fig. 21.** Relative spatial responsivity,  $h(x, y)$ , for channel 6 of the SXR, which was on gain 10. a) A contour plot of data, in non-uniform increments, to emphasize the out-of-field response. The increments between the contours double with each step, beginning with 0.01 mV: 0.01 mV, 0.02 mV, 0.04 mV, ..., to 5.0 mV.



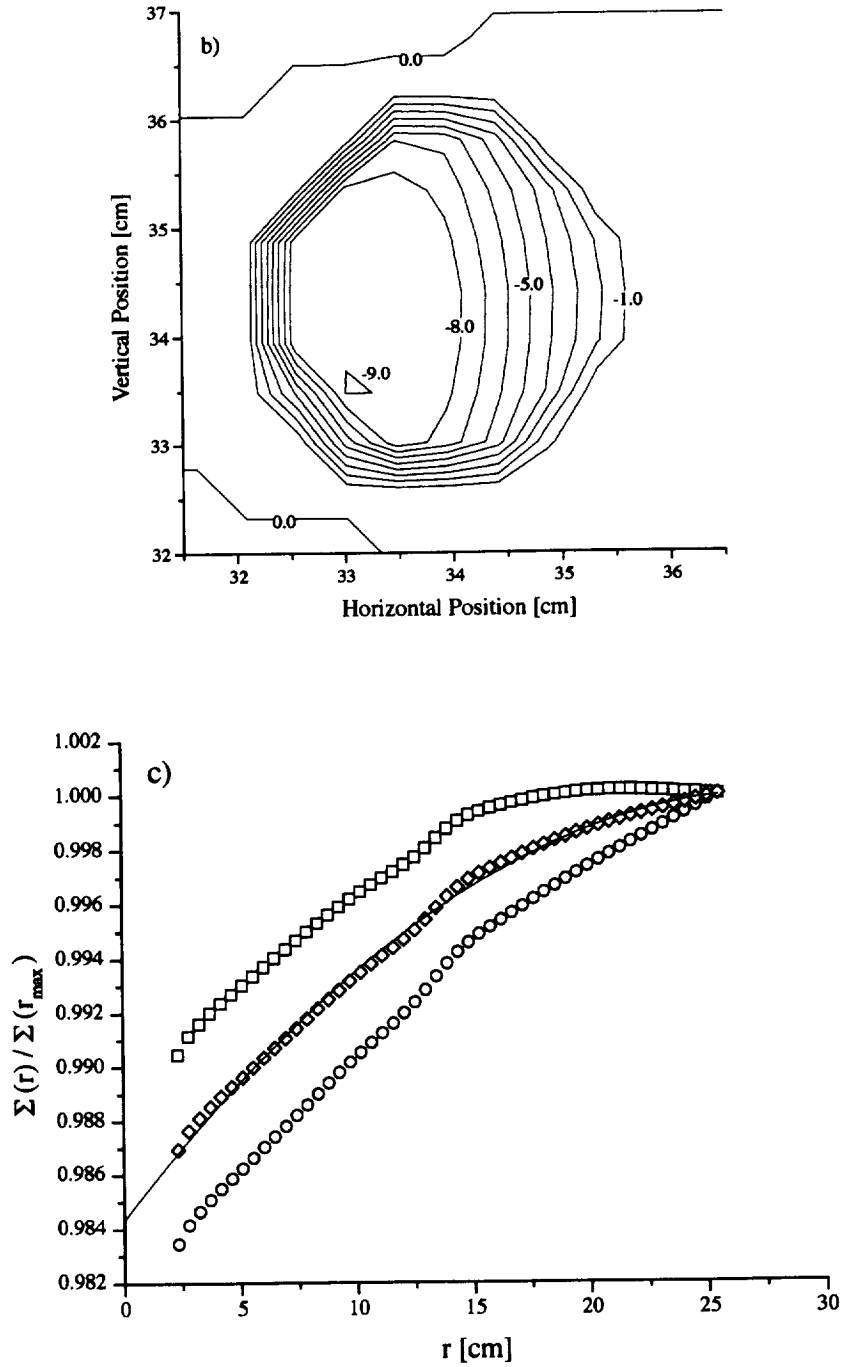


**Fig. 21. (cont.)** Relative spatial responsivity,  $h(x, y)$ , for channel 6 of the SXR, which was on gain 10. **b)** A contour plot of data, in 1 V increments, to illustrate the in-field response. The non-uniformity within the field of view is because of vignetting. **c)** The normalized and integrated net signals are determined using a background of  $\langle b \rangle = 2.933$  mV. The area used for the normalization was 51.04 cm square. The open diamonds, squares, and circles correspond to  $\langle b \rangle$ ,  $b_-$  (2.855 mV), and  $b_+$  (3.011 mV), respectively. The solid line is a quadratic fit to the normalized sums using  $\langle b \rangle$  for  $r > 3.712$  cm.

**Table 11.** Coefficients for the quadratic model of the normalized sums describing the spatial responsivity of the SXR.

Channel	$p_0$	$p_1$ [cm <sup>-1</sup> ]	$p_2$ [cm <sup>-2</sup> ]
1	0.993328	$6.61411 \times 10^{-4}$	$-1.57740 \times 10^{-5}$
2	0.996941	$4.32709 \times 10^{-4}$	$-1.47561 \times 10^{-5}$
3	0.997857	$2.59628 \times 10^{-4}$	$-7.92546 \times 10^{-6}$
4	0.996082	$4.03990 \times 10^{-4}$	$-1.04407 \times 10^{-5}$
5	0.992566	$6.95291 \times 10^{-4}$	$-1.53879 \times 10^{-5}$
6	0.984308	$1.12093 \times 10^{-4}$	$-1.99181 \times 10^{-5}$

where  $p_0$ ,  $p_1$ , and  $p_2$  are polynomial coefficients for normalized sums, and the source area,  $A$ , is smaller than the maximum source area,  $A_{\max}$ . The quotient of two such factors, one with  $A$  equal to  $A_{cs}$  and the other with  $A$  equal to  $A_{ms}$ , is the spatial correction factor  $k_a$ , as long as  $A_{\max}$  is larger than the measured source. To facilitate evaluating  $k_a$ , the normalized sums were fit to a second order polynomial as indicated in (22). The fit was limited to the area outside the entrance window of the SXR. The coefficients for the polynomials corresponding to (b) for the six channels of the SXR are given in Table 11.

The overall analysis is complicated by the fact that the SXR is a variable focus instrument. The diameter of the entrance window scales as

$$\frac{\Phi_{EW}}{\Phi'_{EW}} = \frac{\frac{d}{fl} - 1}{\frac{d'}{fl} - 1}, \quad (23)$$

where  $\Phi_{EW}$  and  $\Phi'_{EW}$  are the diameters of the entrance windows,  $d$  and  $d'$  are the lens focal settings, and  $fl$  is the focal length of the lens. Measurements of the point-spread response for channels 1–5 were made with the lamp about 1.1 m from the faceplate of the SXR, and a lens focal setting of 1.2 m. For channel 6, these parameters were 0.91 m and 0.85 m, respectively. Measurements of the calibration source were made with the lens focal setting of 0.85 m, and measurements of test sources correspond to a range of lens focal settings. To determine  $k_a$ , therefore, the radial coordinate in the polynomial expression must first be scaled according to (23) to correspond to the lens focal setting of the point-spread response measurements. For large sources, the extent of the point-spread measurements may not correspond to the full diameter of the source, and care must be taken not to extrapolate (22) past the region of measurement. If the properly scaled radii for the calibrated and measured sources are  $r_{cs}$  and  $r_{ms}$ , respectively, then the spatial correction factor is

$$k_a = \frac{p_0 + p_1 r_{cs} + p_2 r_{cs}^2}{p_0 + p_1 r_{ms} + p_2 r_{ms}^2}, \quad (24)$$

The above, (24), gives the magnitude of the correction for the non-ideal point-spread response of the SXR. For

the calculation to be correct, both the calibration source and the measured source must be spatially uniform. To estimate the uncertainty of the correction, the normalized sums generated using  $b_-$  and  $b_+$  were also fit to a quadratic function and the upper and lower limit for  $k_a$  was determined. Assuming a uniform distribution for  $k_a$ , bounded by these limits, the standard uncertainty in  $k_a$  is  $u_a = [k_a(b_+) - k_a(b_-)]/3.46$ , (Taylor and Kuyatt 1994).†

An example calculation is given in Table 12 for a 1.07 m diameter integrating sphere from GSFC, which has an exit diameter of 39.5 cm (Johnson et al. 1996). The correction factor  $k_a$  is largest for channels 5 and 6, up to 1.1%, and is calculable with reasonable accuracy, about 0.1%. For the other channels, the correction is smaller in magnitude, but the uncertainty is greater because of the increased uncertainty in the measurements and the determination of the background.

### 3.2.4 Linearity of Radiometric Response

The dependence of the spectral-ray flux responsivity on the magnitude of the spectral radiance was found to be negligible for all six channels of the SXR. This was accomplished using an optical beamconjoiner that operates using the principle of superposition (Saunders and Shumaker 1984, and Thompson and Chen 1994). The instrument, Beamcon III, consists of a source; optics for separating the flux into two beams, and then recombining the flux into a single output beam; and filter wheels, containing neutral density filters and opaque positions. Three filter wheels are used, one in each beam path and one after the two beams have been recombined. The output of Beamcon III, which was slightly polarized, filled the aperture stop of the SXR, but underfilled the field of view.

Because signals from the SXR are the independent variable and not the flux, it is easier to discuss the method in terms of a function that is the inverse to the function described in Sect. 3.1.2, or  $\Phi(\lambda) \propto Y(S)$ . Here,  $Y$  is an

† Uncertainties evaluated using any technique other than determining the standard deviation from a series of measurements, are Type B uncertainties. The method of using an estimate for the upper and lower values with the assumption of a uniform probability distribution function, is used to estimate other Type B uncertainty components in this document.

**Table 12.** Example spatial correction factors,  $k_a$ , for the SXR and the GSFC integrating sphere, for two choices of the distance between the SXR and the sphere aperture.

Channel	LENS FOCAL SETTING			
	0.85 m		1.13 m	
	$k_a$	$u_a$ [%]	$k_a$	$u_a$ [%]
1	0.9957	0.30	0.9957	0.30
2	0.9985	0.36	0.9985	0.36
3	0.9988	0.14	0.9988	0.14
4	0.9976	0.09	0.9976	0.09
5	0.9950	0.08	0.9950	0.08
6	0.9887	0.12	0.9910	0.06

arbitrary, nonlinear function and  $S$  is the net signal, with the average background determined before each series of measurements using the opaque position in the filter wheel in the recombined beam (denoted the third filter wheel). With the third filter wheel set on one of up to five possible neutral density filters (denoted  $K$ ), measurements are made for all possible combinations of the two filter wheels that are in the separate beams, including measurements with each wheel on the opaque position.

The two beams are denoted 1 and 2; beam 1 has four filters denoted  $I$  while beam 2 has four filters denoted  $J$ . Given this, the flux in beam 1 when the filter wheel in beam 2 is in the opaque position ( $J = 0$ ) is  $\Phi_{I,0,K}$  and the flux for the inverse situation is  $\Phi_{0,J,K}$ . According to the principle of superposition, the individual beam fluxes sum to the flux when the three filter wheels are set to the corresponding positions:

$$\Phi_{I,J,K} = \Phi_{I,0,K} + \Phi_{0,J,K}. \quad (25)$$

The net signals measured by the SXR are given by  $S_{I,0,K}$  for the signal from beam 1 with no flux from beam 2,  $S_{0,J,K}$  for the signal from beam 2 with no flux from beam 1, and  $S_{I,J,K}$  for the combined flux when the filters correspond to the ones used in each beam for  $S_{0,J,K}$  and  $S_{I,0,K}$ . The results were analyzed by assuming a polynomial to approximate the fluxes in terms of the net signals,

$$\begin{aligned} \Upsilon(S_{I,J,K}) &= r_0 + S_{I,J,K} + r_2 S_{I,J,K}^2 + r_3 S_{I,J,K}^3 \\ &\approx \Phi'_{I,J,K}. \end{aligned} \quad (26)$$

The unknowns in this system of equations are the normalized fluxes  $\Phi'_{I,J,K}$  and the polynomial coefficients of linearity response  $r_0$ ,  $r_2$ , and  $r_3$ . The coefficient  $r_0$  is small and accounts for imperfections in determining the net signals for low fluxes. Because there are more equations than unknowns, a least-squares technique was used. The normalized residuals,  $r_{I,J,K}$ , are given by

$$r_{I,J,K} = 1 - \frac{\Upsilon(S_{0,J,K}) + \Upsilon(S_{I,0,K})}{\Upsilon(S_{I,J,K})}, \quad (27)$$

and they should be close to zero according to the principle of superposition if the model function  $\Upsilon(S)$  is a good representation of the data. The normalized residuals in (27) were squared, summed, and normalized by the number of degrees of freedom, resulting in a  $\chi^2$  variable. The values for  $r_0$ ,  $r_2$ , and  $r_3$  were found by minimizing  $\chi^2$ . Using these values, the normalized fluxes were then determined from (26).

**Table 13.** The relative standard uncertainties in the SXR linearity analysis for the relative flux responsivity data,  $u_{flux}$ , expressed in units of percent.

Channel	Photocurrents	$u_{flux}$ [%]
1	10 pA to 10 nA	0.11
2	10 pA to 10 nA	0.11
3	100 pA to 100 nA	0.10
4	100 pA to 100 nA	0.09
5	100 pA to 100 nA	0.11
6	100 pA to 1 $\mu$ A	0.09

The quantity that demonstrates the degree of nonlinearity is the relative flux responsivity,  $S/\Phi(\lambda)$ . From (26) and (27), the values given by

$$\frac{S_{I,J,K}}{\Phi'_{I,J,K}} = \frac{S_{I,J,K}}{\Upsilon(S_{0,J,K}) + \Upsilon(S_{I,0,K})}, \quad (28)$$

are plotted in Fig. 22 to illustrate the level of agreement of the signal for the combined beam with the polynomials. The polynomial model for the normalized flux in terms of the net signal, (26), could be used with the measurement equation to correct for nonlinearity. Because the SXR data do not depend on the photocurrent (Fig. 22), treatment of the SXR as a linear instrument is valid. The uncertainty associated with this statement of linearity is less than 0.1%. This value was determined using a uniform distribution function and estimating the extreme values for  $S_{I,J,K}/\Phi'_{I,J,K}$  for photocurrents where the noise in the beamconjoiner data was not significant. The summary of the results, including the uncertainties, is in Table 13. The

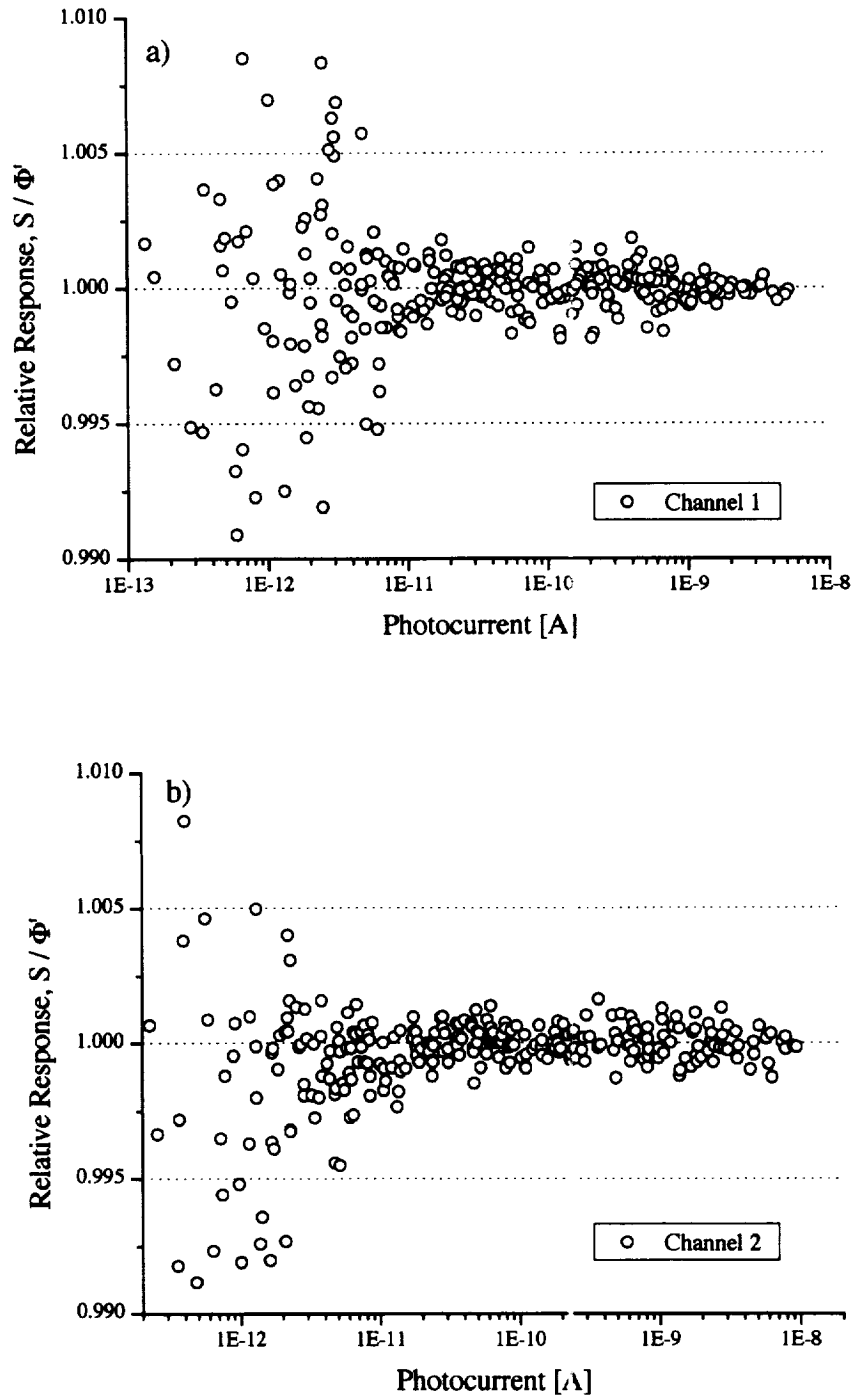


**Fig. 22.** Relative flux responsivity data for each channel of the SXR as measured with the Beamcon III. In panels a) to d), channels 1–4 were measured for all four values of the SXR voltage gain, but only data acquired with gains 1, 10, and 100 were used for the analysis. The output of Beamcon III was too low to give the maximum output at gain 1 except for channel 2. For channels 1, 3, and 4, the maximum voltage was 5.2 V, 2.4 V, and 4.2 V, respectively.

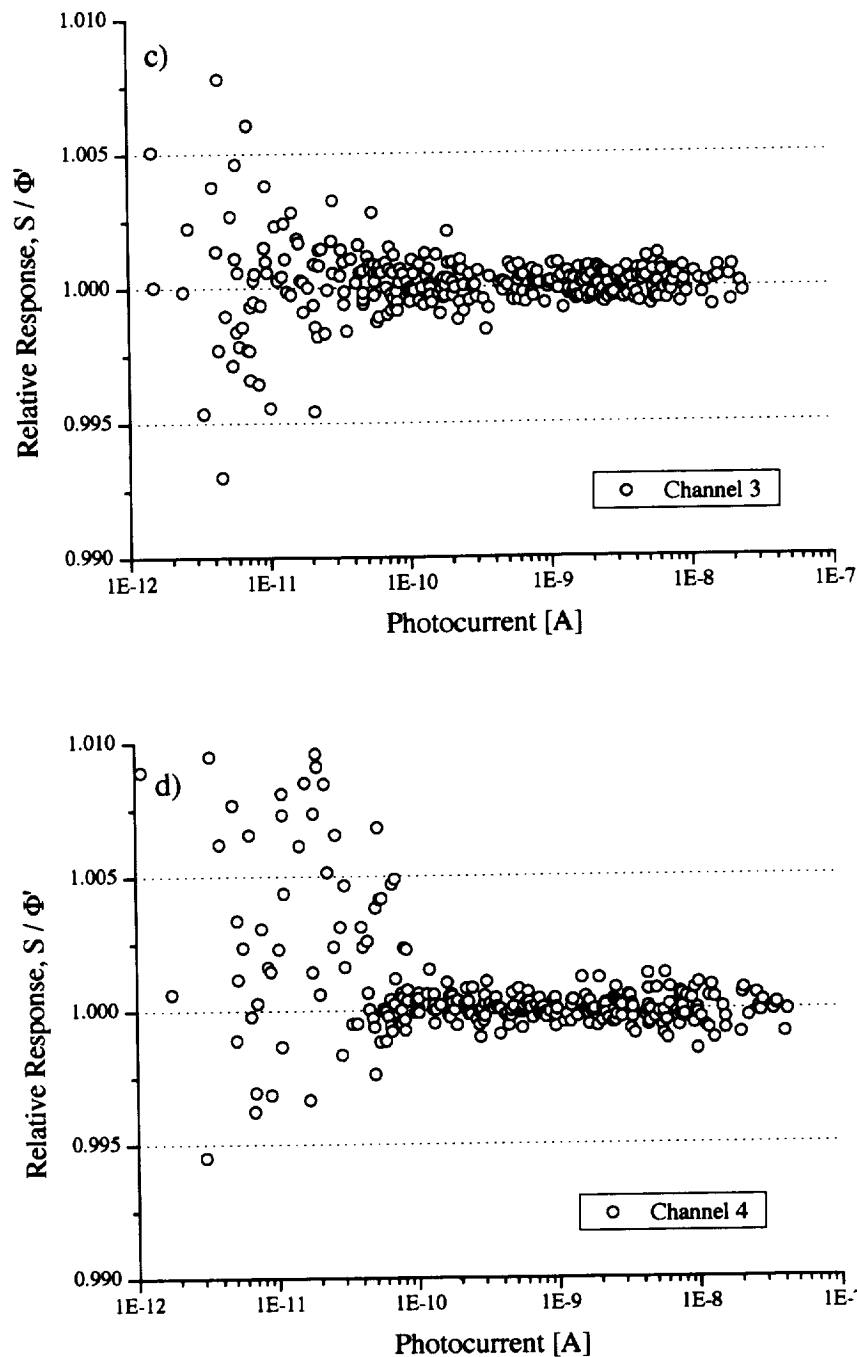


**Fig. 22. (cont.)** Relative flux responsivity data for each channel of the SXR as measured with the Beamcon III. In panels a) to d), channels 1–4 were measured for all four values of the SXR voltage gain, but only data acquired with gains 1, 10, and 100 were used for the analysis. The output of Beamcon III was too low to give the maximum output at gain 1 except for channel 2. For channels 1, 3, and 4, the maximum voltage was 5.2 V, 2.4 V, and 4.2 V, respectively.

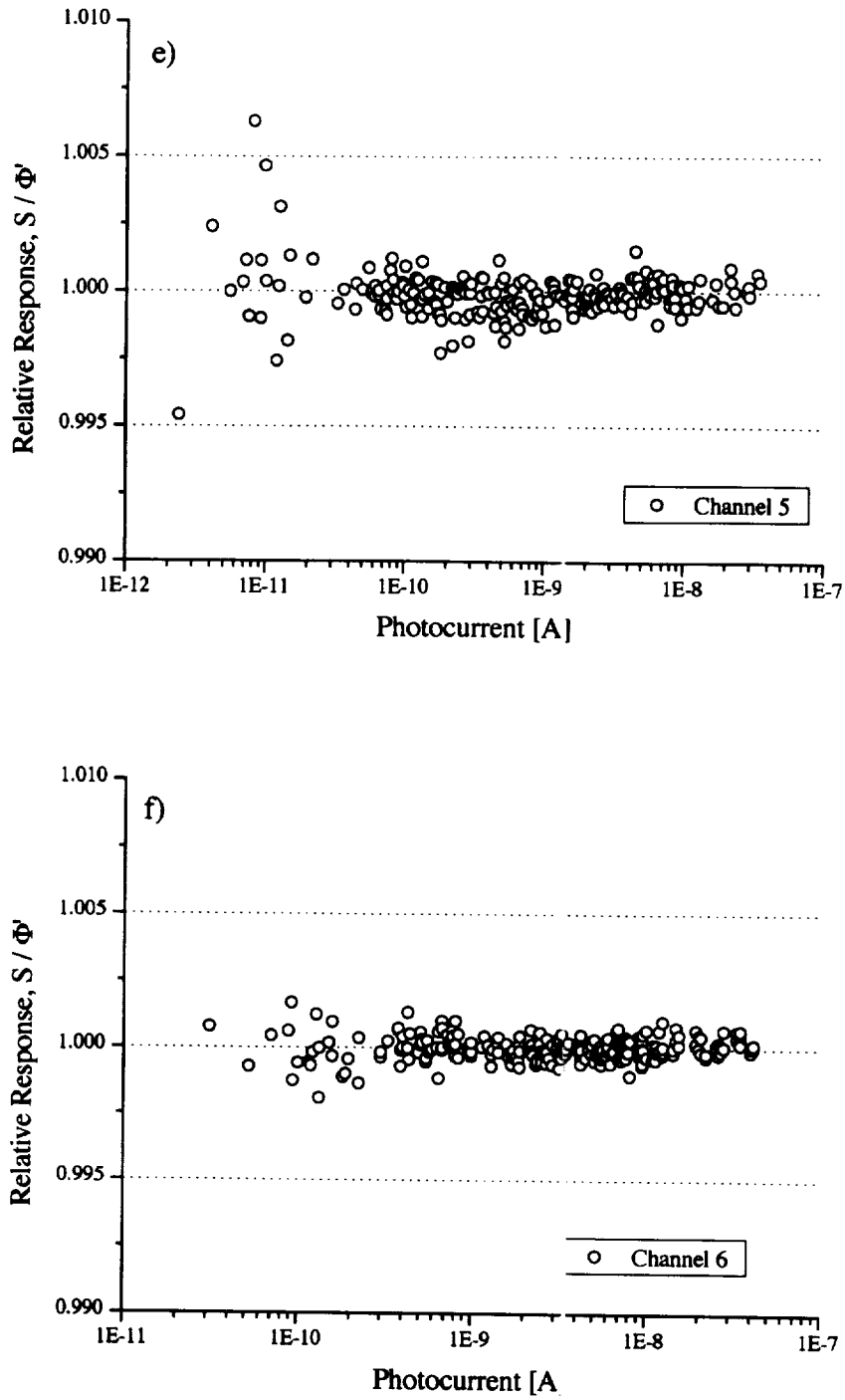


**Fig. 22. (cont.)** Relative flux responsivity data for each channel of the SXR as measured with the Beamcon III. In panels e) and f), channels 5 and 6 were measured for SXR voltage gains, 1, 10, and 100, and these data were used in the analysis. The maximum signal for unity gain and channel 5 was 3.5 V, but for channel 6, the value was only 0.41 V.

photocurrent is fixed by  $R_F$ , and the upper value in the table corresponds to 10 V at  $G = 1$ . In some cases, the output of Beamcon III was not sufficient to produce this value (Fig. 22). The minimum photocurrent was determined by examining the values in Fig. 22 to determine where the noise in the measurements would affect the estimate of the uncertainty in the linearity.

### 3.2.5 Temporal Response

There are several concepts related to temporal response that are important. One is the time required for the photodiode and amplifier to stabilize after a large change in magnitude of the incident flux, i.e., from full flux to no flux or vice versa. The SXR was not characterized for this response time, which could have been done using a stable source, a shutter, and a fast data acquisition system. Instead, an estimate is used. The response time, which is 10 ms for any channel in the SXR, is given by the  $R_F C_F$  time constant of the transimpedance amplifier (Fig. 9), where  $C_F$  is the damping capacitor. Therefore, the delay between measurements of flux of different magnitude should be at least 50 ms. For the measurements reported here, this delay was at least 500 ms.

The warm-up time for the SXR was not studied in detail, although there are standard procedures written by the American Society for Testing and Materials (ASTM) for quantifying this parameter (ASTM Test E1256—95 [ASTM 1997]). Time is required for the filters and photodiodes to reach the operating temperature of 26°C after the TEC control system is initiated. The operation of the DPA at 26°C may affect the temperature of other components in the SXR, particularly the amplifier circuit board, whose performance may depend on temperature. To ensure there is no effect related to the warm-up interval, the SXR should be turned on, and the DPA controlled to 26°C, for at least 4 h before measurements.

The ASTM Test E1256—95 also identifies long-term drift and repeatability as measures of the temporal behavior of a radiometer. Both involve measurements of the same source under the same conditions, but with different time scales and different modes of operation. Long-term drift involves continuous measurement of the same source for at least one month, without turning off the radiometer. Repeatability is defined in terms of consecutive measurements, once a day, for 12 working days, with the radiometer turned off between measurements. In the context of E1256—95, the long-term drift of the SXR was studied at some of the SIRREX activities. For example, at SIRREX-3, the SXR was turned on and stabilized to 26°C for the entire experiment, about 12 days, except for brief intervals when it had to be moved from one lab to another.

For measurements of a GSFC integrating sphere over a 9-day interval, the measurements agreed to within 0.3% (Mueller et al. 1996). In the context of ASTM Test E1256—95, the repeatability was evaluated by viewing the same

source before and after some other event. Before and after the SXR was deployed to Japan in February 1995, it measured the low level radiance (LLR) source at NIST. The repeated measurements agreed to within 0.05% on average, except for channel 1, which changed by 0.3% (Johnson et al. 1997). Finally, for recent measurements of the same GSFC integrating sphere at Orbital Sciences Corporation (OSC) for the recalibration of SeaWiFS, the SXR measured the sphere in January, March, and April 1997. The standard deviation of the results at the highest radiance level for channel 1 is 0.5%. Because measurements of long-term drift and repeatability are convolved with the stability and repeatability of the source of radiant flux, it is only possible to estimate upper limits for the SXR. Based on experience with the SXR, the estimated values for the repeatability and long-term drift are 0.1% and 0.3%, respectively.

### 3.2.6 Absolute Calibration

The calibration factor ( $D_{cs}$ ), defined in (5), was determined for each channel of the SXR using a uniform and lambertian calibration source, the LLR source, on 8–9 September 1994. The absolute spectral radiance of the LLR source was determined at the NIST FASCAL facility for 13 wavelengths on 16 September 1994. The spectral radiance was evaluated at the SXR wavelengths [(14) and Table 2) to determine  $L_{cs}(\lambda_m)$ ].

The LLR source is a model OL420 from Optronic Laboratories. The source consists of an externally-illuminated sphere, with the exit aperture 90° offset from the entrance aperture. Quartz windows on each aperture keep the sphere clean. The sphere is 20.32 cm in diameter and is coated with barium sulfate; the exit window is 5.72 cm in diameter. A 45 W lamp, located in a baffled chamber mounted to the top of the sphere, is translated using a precision lead screw to create a continuously variable radiance source. A mechanical slide is used to control the state of the output. The slide, which contains one opaque and two open positions (one of which can hold a filter), is located between the lamp and the entrance aperture of the sphere. For the SXR calibration, the fully open position was used. The opaque position allows for background measurements while the LLR lamp is on. The LLR source also contains an aperture wheel located between the lamp and the sphere as an additional control on the output radiance. For the SXR calibration, the aperture wheel and lamp distance were set for maximum output.

At the time of purchase, the sphere was modified by adding a monitor radiometer, according to NIST's request. The radiometer, which is composed of a silicon photodiode and a photometric filter, is mounted in the wall of the sphere and views a portion of the rear and side of the sphere interior. The temperature of the monitor radiometer is not stabilized. The exit aperture views the back of the sphere, and the lamp directly illuminates the bottom of the sphere. During the SXR calibration, the signal

from the monitor photodiode was recorded manually, but during the calibration of the LLR source at FASCAL, it was recorded automatically. The current to the lamp was supplied by a precision current source, model HP 6030A from Hewlett-Packard. Also during the SXR calibration, the current was measured using a standard resistor and the values were recorded using a program in Visual Basic. To ensure the most stable operation, the program should operate in a closed-loop mode of operation (Walker and Thompson 1994), but for the SXR calibration, the current was updated manually every few minutes. The same resistor, a 0.1  $\Omega$ , 15 A standard resistor from Leeds and Northrup (serial number 1126259), was used for the calibration of the LLR source at FASCAL. The standard resistor was calibrated by the NIST Electricity Division on 31 January 1994.

The uniformity of the spectral radiance across the center of the LLR exit aperture was measured at FASCAL during the radiometric calibration. At 487 nm, the Type B uncertainty was  $\pm 0.17\%$  in the spectral radiance because of variability in the radiance within the aperture. This value is consistent with that determined from a full spatial map, which was done during the commissioning of the LLR source (A. Thompson, pers. comm.).

The FASCAL facility is used primarily for standard lamp irradiance calibrations (Walker et al. 1987b), and the working standard for spectral irradiance and radiance calibrations is a variable temperature blackbody source. The temperature of the blackbody is determined by comparing it, at 654.6 nm, to standard tungsten strip lamps, which are calibrated periodically using a gold-point blackbody. The spectral radiance of the LLR source was determined at each wavelength by comparing the flux from the blackbody to the flux from the integrating sphere. The temperature of the blackbody was adjusted throughout the wavelength interval, which was 350–900 nm for the LLR source, so the flux ratio was as close to unity as was reasonable. In the case of spectral irradiance calibrations, a FASCAL integrating sphere source is calibrated for spectral radiance in the same manner as was used for the LLR source. This source is then used as a standard of spectral irradiance for the calibrations of the standard 1,000 W irradiance lamps. There are, therefore, fewer measurement procedures in determining the spectral radiance responsivity calibration of the SXR compared to a radiometer calibrated using a standard lamp of spectral irradiance. The SXR measurements should be consistent, within the uncertainties, of a spectral radiance scale derived using a NIST-calibrated standard irradiance lamp.

The spectral radiance of the LLR source determined at FASCAL is given in Table 14 at the 13 measured wavelengths from 350–900 nm. The relative standard uncertainties,  $u_{LLR}$ , are also indicated, although they were only provided at six wavelengths. The uncertainties at the remaining wavelengths,  $u'_{LLR}$ , were estimated using a smoothing

interpolation routine in a standard analysis package (KaleidaGraph from Synergy Software). The uncertainty is the smallest at the wavelength where the calibration chain involves measuring the reference source: a stable tungsten strip lamp. In order to determine the spectral radiance at the SXR wavelengths, and to estimate the uncertainty in the interpolation methods, the FASCAL spectral radiance data were fit to a model that describes the radiance from a blackbody, modified by a fourth-order polynomial:

$$L_{cs}(\lambda) = \left( c_0 + c_1\lambda + c_2\lambda^2 + c_3\lambda^3 + c_4\lambda^4 \right) \frac{e^{\beta + \frac{\alpha}{\lambda}}}{\lambda^5}, \quad (29)$$

where  $c_0$ – $c_4$  are coefficients,  $e$  is the base of the natural logarithms, and  $\alpha$  and  $\beta$  are parameters in a modified blackbody model of spectral radiance; they are determined by a nonlinear least squares fit to the FASCAL spectral radiance values.

**Table 14.** Results of the calibration of the LLR by FASCAL on 16 September 1994.

Wavelength [nm]	Spectral Radiance [ $\mu\text{W cm}^{-2} \text{sr}^{-1} \text{nm}^{-1}$ ]	$u_{LLR}$ [%]	$u'_{LLR}$ [%]
350	0.01317	0.70	
360	0.01832		0.62
380	0.03393		0.50
400	0.05842	0.40	
450	0.1572	0.40	
500	0.2972		0.37
550	0.4607		0.33
600	0.6279		0.28
654.6	0.8009	0.25	
700	0.9254		0.27
750	1.060		0.30
800	1.152	0.40	
900	1.235	1.50	

Three results, of order  $\lambda^4$ , calculated using a Basic program from FASCAL are shown in Fig. 23. One fit was performed using the data from 380–900 nm, the second using the data from 350–900 nm, and the third using the data from 400–800 nm. For comparison, a fit of order  $\lambda^2$  using the solver feature in a spreadsheet package (Excel from Microsoft Corporation) was also performed. In all four cases, the results were normalized by the FASCAL values for presentation in Fig. 23. A cubic spline fit was also performed on the FASCAL data using KaleidaGraph, and the values were interpolated on a 2 nm grid (Fig. 23). The results of the cubic spline fit were normalized by the fourth-order blackbody fit that used the data from 400–800 nm. This ratio is identical to the modified blackbody fit normalized by the FASCAL data at the FASCAL wavelengths, because the cubic spline method reproduces the known values.

The blackbody fits from 400–800 nm are in better agreement with the FASCAL values for the wavelength interval



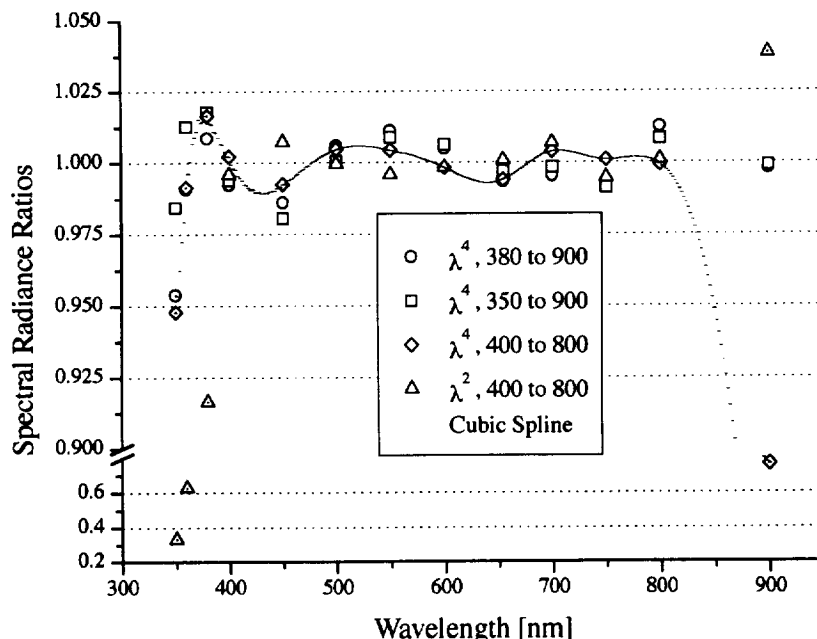


**Fig. 23.** Comparison of the interpolation methods used to determine the spectral radiance of the LLR source at the SXR measurement wavelengths. The values plotted using the circle, square, diamond, and triangle symbols are evaluations of the modified blackbody model normalized by the FASCAL calibration values. The range of wavelengths used to determine the parameters of the fit are given in the legend. Symbols with the central dot are extrapolations of the model with respect to the wavelength interval used in the fit. Values plotted using the short dash symbols are the result of a cubic spline fit to the 13 FASCAL values, interpolated onto a 2 nm grid and normalized by the fourth-order fit from 400–800 nm.

that overlaps the SXR wavelengths. The spectral radiance at the SXR wavelengths was determined using this fourth-order fit. The relative standard uncertainty in the sphere radiance,  $u_{\text{LLR}}$ , was determined from the FASCAL uncertainties. The Type B uncertainty,  $u_{\text{Fit}}$  associated with the method of interpolation was determined by evaluating the SXR radiances using the range of values from second order and the fourth order modified blackbody fit and the cubic spline method and assuming a uniform probability distribution function. The results are given in Table 15.

**Table 15.** Spectral radiance of the LLR source at the SXR measurement wavelengths.

$\lambda_m$ [nm]	Spectral Radiance [ $\mu\text{W cm}^{-2} \text{sr}^{-1} \text{nm}^{-1}$ ]	$u_{\text{LLR}}$ [%]	$u_{\text{Fit}}$ [%]
411.222	0.075763	0.42	0.71
441.495	0.13577	0.40	1.03
486.938	0.25819	0.38	0.13
547.873	0.45560	0.33	0.51
661.718	0.81740	0.25	0.39
774.767	1.1137	0.34	0.39

The SXR was calibrated using the LLR source on 8–9 September 1994. The SXR was 85.5 cm from the sphere, and the lens focus setting was at the minimum value of 0.85 m. The LLR source was translated in the horizontal

and vertical directions until the SXR viewed the center of the source. The sphere was allowed to stabilize before proceeding with the SXR measurements.

Ten readings of the DMM were taken, with a delay of 1 s between readings, and the average and standard deviation stored in a data file. The DMM was set to average over 10 power line cycles. With the LLR source at  $6.5000 \text{ A} \pm 0.0001 \text{ A}$ , the signals were recorded sequentially from channels 1–6, forming a set of SXR data.

Two gain ranges and four orientations of the SXR were used. On the first day, with the SXR gain equal to 10 and the orientation in the E position, four data sets were recorded. The SXR was then rotated about the optical axis to the N, W, and S positions successively; four sets of data were recorded for each orientation. When the SXR was rotated, it had to be re-aligned on the LLR source aperture using the optical alignment system. The E position was then repeated, acquiring four more sets; the gain was changed to unity and four additional sets were recorded. On the second day, the SXR was fixed in the E position and two sets were recorded using unity gain and four sets using a gain of 10. The background signal was recorded with the lamp off and the lens cap of the SXR off before and after the sphere data were recorded.

Interspersed with the signal measurements, the lens cap was put on and the background signal recorded. Because

there were no extraneous sources of optical radiation, these two methods to measure the background resulted in the same value, and both were used in the analysis.

The relative standard deviation of the signal for one channel in one set of SXR data was typically about 0.003%, with some values as large as 0.015%. For the background, the relative standard deviation was typically about 0.5%, with some values as large as 3%. The background signal, of about 3 mV, was nearly the same value for all six channels. This offset voltage does not vary substantially between gains 1 and 10. The voltages measured for the LLR source varied between -31 mV for channel 6 on unity gain, and -2.13 V on channel 5 for a gain of 10.

Statistical analysis would imply that the average net signal for these SXR data should be determined by calculating the average net signals at both gain settings, multiplying the values at gain 10 by  $k_{10}$  (Table 8), estimating the uncertainties for each gain setting, and forming a weighted average of the results. This assumes that all the experimental configurations (day, time, orientation of SXR, and gain) are drawn from the same population; however, the results depend on some of the experimental parameters, such as the SXR orientation. In addition, the sphere appeared to drift with time at the shorter SXR wavelengths; therefore, it is not correct to calculate average net signals from all of the data because the different experimental parameters were not uniformly represented, especially with respect to the SXR orientation.

For each channel, the SXR data were analyzed by first determining the average background and the uncertainty in the background for each gain setting,  $b_G$ :

$$b_G = \frac{1}{N_G} \sum b_G^j, \quad (30)$$

and

$$\sigma_{b_G}^2 = \frac{1}{N_G - 1} \sum (b_G^j - b_G)^2, \quad (31)$$

where  $N$  is the number of samples, the subscript  $G$  refers to the gain setting, the index  $j$  is one result for the average of the 10 readings of the DMM, and  $\sigma^2$  is the statistical variance; there are six equations of this form, one for each channel. The net signal for each of the average DMM readings is

$$S_1^j = v_1^j - b_1, \quad (32)$$

and

$$S_{10}^j = (v_{10}^j - b_{10})k_{10}, \quad (33)$$

where the symbol  $v$  is used for the total signal and  $k_{10}$  is 0.1000351 according to Table 8. The standard uncertainties in the net signals were determined from propagation of errors, using the standard deviation of the DMM readings, the standard deviation from (30) and (31) for the average background, and the standard uncertainty from Table 8 for the gain factor. The net signals, multiplied by -1, corresponding to each result from the DMM are plotted in

Fig. 24, where the solid vertical lines represent the combined standard uncertainties. The larger uncertainties at gain 10 result from the uncertainty in  $k_{10}$ .

The net signal for channel 1, Fig. 24a, increased continuously during the 1.5 h experiment on the evening of 8 September, and continued to increase during the 30 min experiment on the morning of 9 September, even though the LLR source was turned off overnight. The total change is about 0.5%. Aside from the drift, there is no dependence on gain, measurement day, or SXR orientation. The value for the average net signal, and therefore,  $\langle D_{cs} \rangle$ , for channel 1 was calculated from the average of all of the measurements. Because of the drift, an estimate of the relative standard uncertainty using statistical methods,  $u_{stat}$  is not valid. Instead, a Type B standard uncertainty, assuming a uniform distribution, was calculated using the minimum and maximum values for the net signal. The results are given in Table 16.

**Table 16.** SXR average net signal voltages, from  $S_1^j$  and  $S_{10}^j$ , for the calibration experiment using the LLR source in September 1994.

Channel	$\lambda_m$ [nm]	Net Signal [V]	$u_{stat}$ [%]
1	411.222	-0.0834293	0.28
2	441.495	-0.199313	0.17
3	486.938	-0.0630667	0.35
4	547.873	-0.110517	0.16
5	661.718	-0.212909	0.15
6	774.767	-0.0335576	0.37

The net signal for channel 2, Fig. 24b, in the E orientation also increased continuously over the course of the experiment, with a total change of about 0.29%. There is also a dependence on orientation, with the N and W data higher than the E and S data, but there is no dependence on gain or measurement day. The value for the average net signal for channel 2 was calculated from the average of the 16 measurements at gain 10 in the E, N, W, and S orientation. The Type B standard uncertainty was estimated using the same method as for channel 1, using the maximum and minimum values for the net signal. This same analysis (below) was also used on channels 3-6.

The net signal for channel 3, Fig. 24c, in the E orientation increased slightly, about 0.1%, over the course of the experiment. There is a dependence on orientation, with a variation of about 0.6% between the W and E values. For channel 4, the temporal dependence in the E orientation was at most 0.05%, and the variability because of orientation was about 0.28%. For channel 5, the temporal dependence was at most 0.03%, and the variability because of orientation was about 0.27%. For channel 6, there was no time dependence in the net signal for the E orientation, and the variability because of orientation was 0.6%.

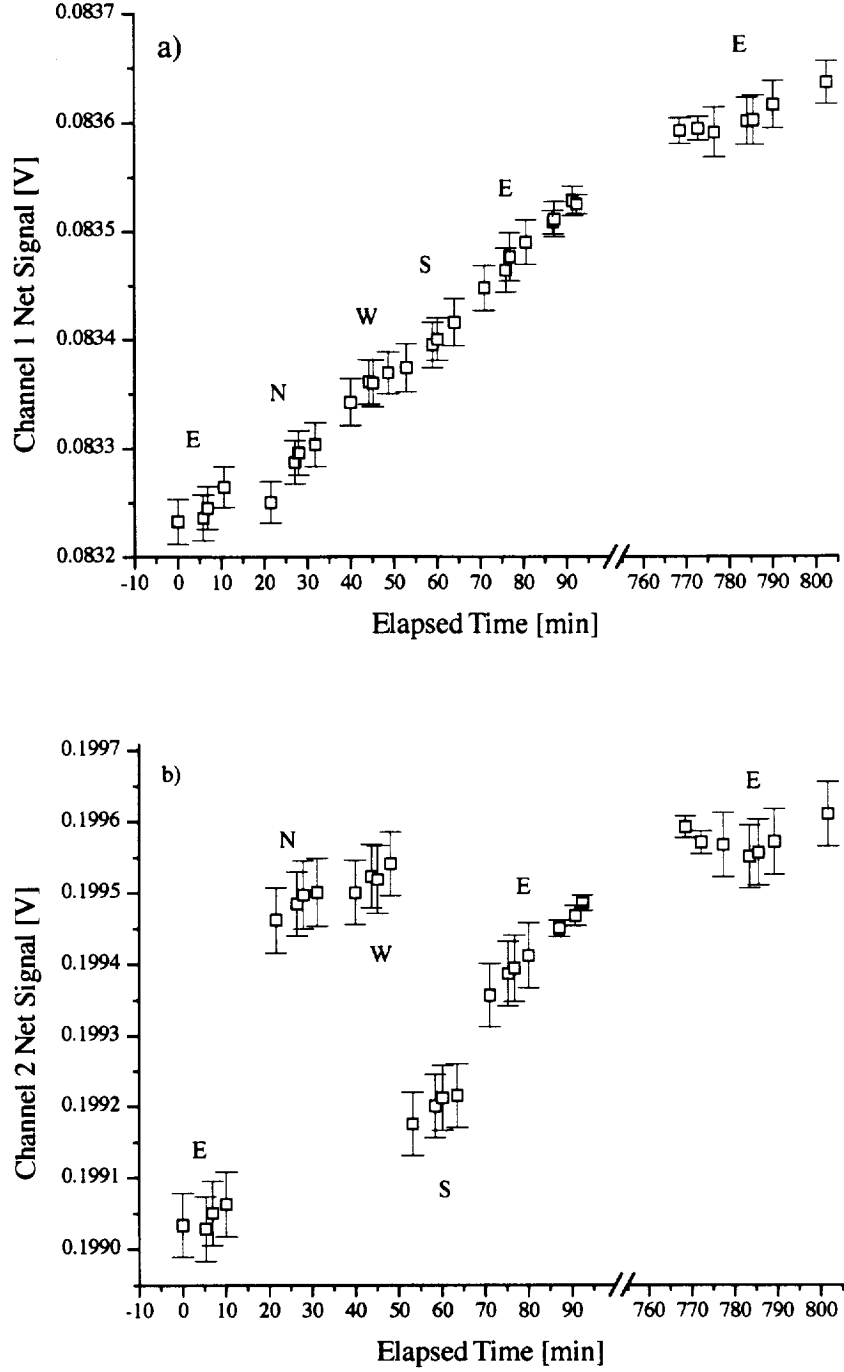


**Fig. 24.** Net signals for the SXR and unity gain during calibration using the LLR source, on 8 and 9 September 1994, plotted as a function of elapsed time. The axis break occurs between the two days of measurements. The LLR source was turned off at the end of the measurements on 8 September and turned on again on 9 September. The vertical bars correspond to the SXR measurement uncertainty. The results for channel 1 (panel a) are dominated by the drift in the signal, which is attributed to the LLR source, not the SXR. The results at the other five channels (panels b–f) exhibit a combination of temporal and spatial variability.

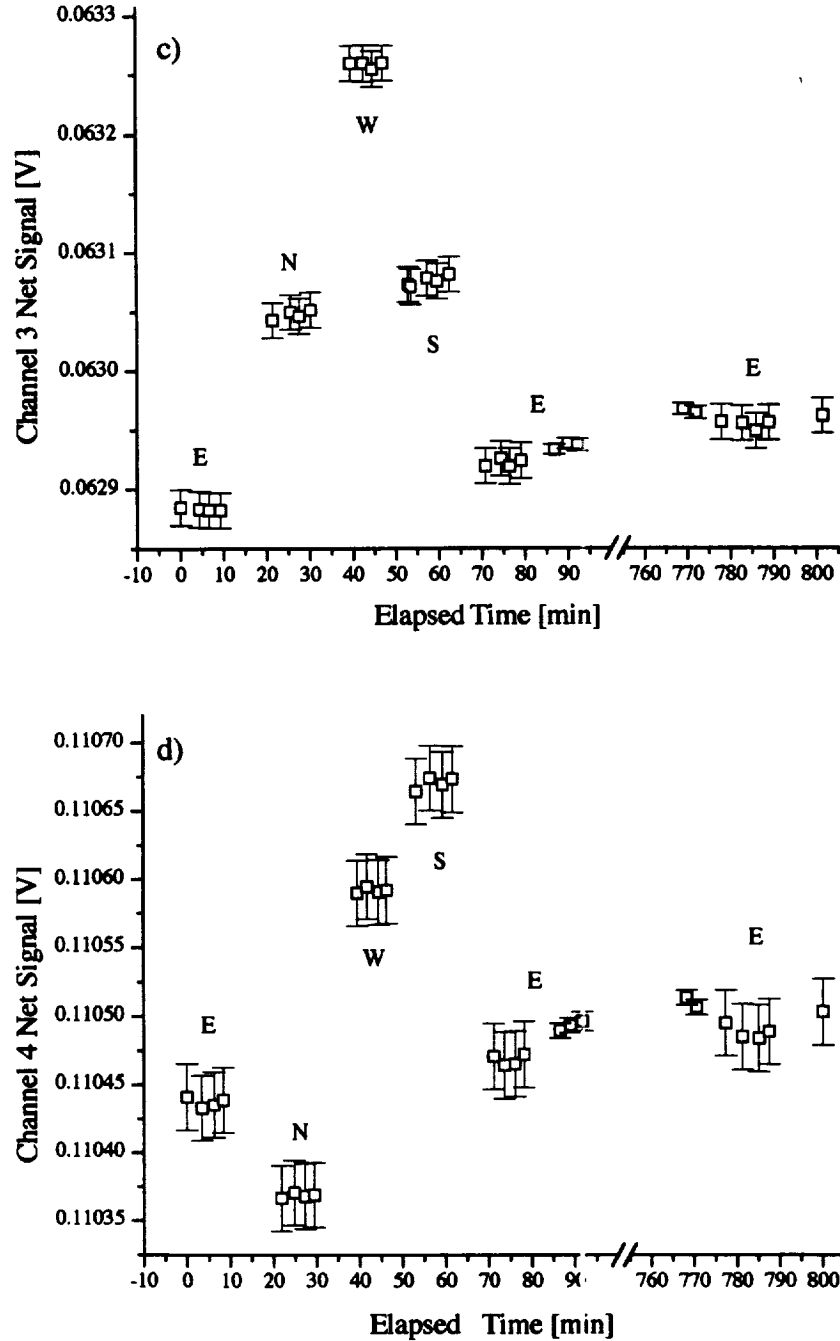


**Fig. 24. (cont.)** Net signals for the SXR and unity gain during calibration using the LLR source, on 8 and 9 September 1994, plotted as a function of elapsed time. The axis break occurs between the two days of measurements. The LLR source was turned off at the end of the measurements on 8 September and turned on again on 9 September. The vertical bars correspond to the SXR measurement uncertainty. The results for channel 1 (panel a) are dominated by the drift in the signal, which is attributed to the LLR source, not the SXR. The results at the other five channels (panels b–f) exhibit a combination of temporal and spatial variability.

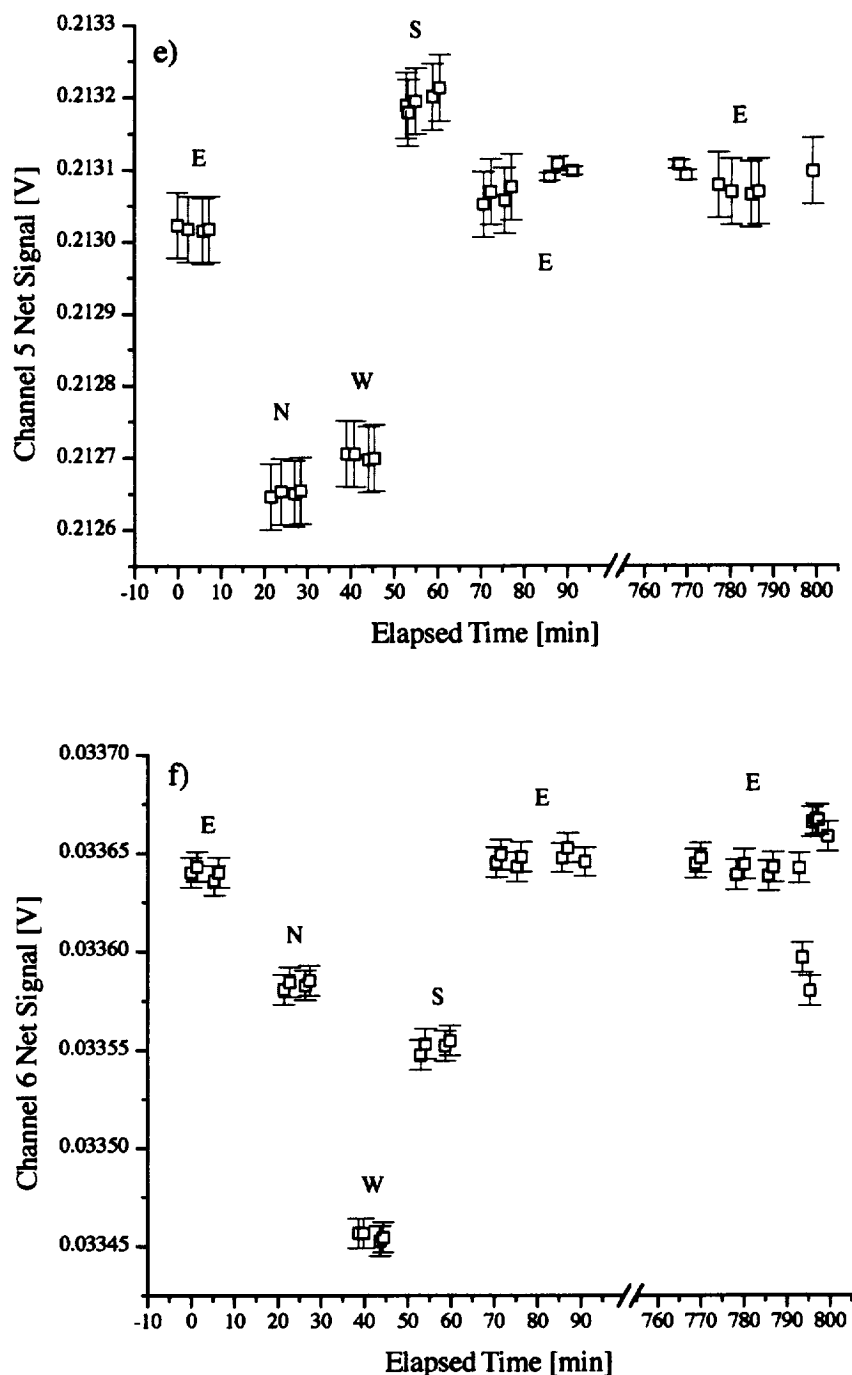


**Fig. 24. (cont.)** Net signals for the SXR and unity gain during calibration using the LLR source, on 8 and 9 September 1994, plotted as a function of elapsed time. The axis break occurs between the two days of measurements. The LLR source was turned off at the end of the measurements on 8 September and turned on again on 9 September. The vertical bars correspond to the SXR measurement uncertainty. The results for channel 1 (panel a) are dominated by the drift in the signal, which is attributed to the LLR source, not the SXR. The results at the other five channels (panels b–f) exhibit a combination of temporal and spatial variability.

The monitor radiometer in the LLR source during the calibration of the SXR indicated that the sphere output increased slightly, about 0.2%, then decreased to about -0.5% of the initial value. The SXR data, however, indicate that the LLR source increased with time as a function of wavelength, with the largest change at 411.2 nm, and no change at 774.8 nm. The spectral dependence of the temporal variability, combined with ancillary SXR measurements, support the conclusion that the LLR source was responsible for the temporal variability, not the SXR. The monitor radiometer is only sensitive to radiation at about 555 nm, with a full-width at half-maximum of about 100 nm. Therefore, it cannot measure the stability of the LLR source as a function of wavelength, and is insensitive to spectral regions where the SXR observed the greatest drift. The instability of the monitor radiometer during the SXR calibration is not understood; during the calibration of the LLR source at FASCAL, the signal was constant.

The dependence of the SXR data on orientation could be caused by alignment errors or by a gradient in the spatial uniformity of the radiance in the exit aperture of the LLR source. Alignment errors are unlikely because the point-spread response data indicate that the area measured was about 3.6 cm in diameter, where the diameter of the LLR exit aperture was 5.72 cm. Comparison of the orientation results for each channel, combined with the relationship between SXR orientation and the location of the channels (Sect. 2.2) supports the conclusion that the sphere radiance in the exit aperture is non-uniform, with the greatest magnitude in the lower left quadrant, and lowest magnitude in the upper right quadrant. Because of the vignetting in the SXR's field of view (part b of Figs. 16–21), spatial variability in the radiance is convolved with the non-uniform field of view, resulting in an orientation-dependent result.

## 4. SXR MEASUREMENTS

Restating the measurement equation, (5),

$$L_{ms}(\lambda_m) = \frac{S_{ms}}{\langle D_{cs} \rangle} k(\lambda_m) = \frac{S_{ms}}{\langle D_{cs} \rangle} k_G k_\lambda k_a, \quad (34)$$

it is clear that when the SXR is used to measure a source of unknown radiance, components of uncertainty are attributed to the measured signal,  $S_{ms}$ , the calibration coefficient,  $\langle D_{cs} \rangle$ , the gain coefficient,  $k_G$ , and the uncertainty in the correction for the size-of-source effect,  $k_a$ . Without knowledge of the relative spectral shape of the test source, it is not possible to estimate the bias (denoted  $k_\lambda$ ), or the uncertainty associated with this factor, but the example calculations in Table 10 can be used to estimate this uncertainty. In addition, there are components of uncertainty that arise from the linearity, stability, and repeatability of the SXR, and well as an uncertainty caused by the uncertainty in  $\lambda_m$ .

## 4.1 Calibration Coefficient Uncertainty

The uncertainty in  $\langle D_{cs} \rangle$  arises from the uncertainty in the

- 1) Average net signals for the LLR source during the calibration of the SXR,
- 2) Spectral radiance of the LLR source at  $\lambda_m$ ,
- 3) Spectral radiance because of the method of interpolation, and
- 4) Spectral radiance because of the uncertainty in  $\lambda_m$ .

The first three of these values are given in Tables 15 and 16 as relative standard uncertainties  $u$ , in units of percent: from measurement statistics,  $u_{stat}$ ; in the spectral radiance of the LLR source,  $u_{LLR}$ ; and that associated with interpolation in  $L(\lambda)$ ,  $u_{fit}$ . The fourth relative uncertainty depends on the relative spectral shape of the LLR source according to

$$u(L, \lambda) = \frac{dL}{L} \frac{d\lambda}{\lambda} = \frac{u_{\lambda_m}}{L} \frac{dL}{d\lambda}, \quad (35)$$

where  $u(L, \lambda)$  is the relative standard uncertainty caused by the uncertainty in  $\lambda_m$ . Equation (29) was used to evaluate the derivative in (35), with the same parameters as were used for the interpolation to the SXR wavelengths. For channels 1–6 and the LLR source, the values for  $u(L, \lambda)$  are 0.12%, 0.09%, 0.06%, 0.04%, 0.02%, and 0.01%, respectively. The decreased sensitivity to the uncertainty in  $\lambda_m$  at the longer wavelengths is because the spectral radiance changes slowly with wavelength in this region. These four components of uncertainty were combined in quadrature to determine the relative combined uncertainty in  $\langle D_{cs} \rangle$  and the values are given in Table 2.

## 4.2 Uncertainty Evaluation

In this section, examples are given of the uncertainty evaluation using the GSFC sphere with both an unknown and known source.

### 4.2.1 Unknown Source

The SXR was used to measure the GSFC integrating sphere source on several occasions. At SIRREX-2 (Mueller et al. 1994), a preliminary version of the SXR was used; at SIRREX-3 (Mueller et al. 1996) and SIRREX-4 (Johnson et al. 1996) the final configuration was fully implemented. The SXR was used in conjunction with a prism-grating monochromator, which was calibrated using a standard lamp of spectral radiance during the NIST calibration and characterization of the GSFC sphere prior to SIRREX-4 (Early and Johnson 1997). Finally, the SXR was used in conjunction with the SeaWiFS instrument and a single-grating monochromator, which was calibrated using a standard lamp of spectral irradiance during the postthermal vacuum calibration of SeaWiFS. Because preliminary estimates of the SXR uncertainties were used in the SIRREX

and GSFC sphere calibration documents, it is appropriate to use the GSFC sphere source as an example of calculating combined standard uncertainties. The SXR data in this example correspond to the 16-lamp configuration at OSC in January 1997. For this sample calculation, it is assumed that no information on the spectral radiance of the GSFC sphere source is available (i.e., data on the relative spectral shape of the radiant flux or actual values for  $L(\lambda)$ ).

The individual components of relative uncertainty, in units of percent, are given in Table 17. The first four columns of uncertainties arise from properties of the SXR. The uncertainty in the SXR calibration,  $u_D$ , is given in the second column (Sect. 4.1 and Table 2). The contribution from any nonlinearity in the SXR is given in the third column (Sect. 3.2.4 and Table 13). The contribution from the repeatability,  $u_{rep}$ , and long-term drift,  $u_d$ , of the SXR is given in the fourth and fifth columns (Sect. 3.2.5).

The next five columns of uncertainties arise from the combined properties of the SXR and the GSFC sphere source. The Type A uncertainty for the measurements of the GSFC source,  $u_{stat}$ , in the 16-lamp configuration are given in the sixth column. These values are negligible, and even at the lowest radiance levels measured for the GSFC sphere (single lamp), are less than 0.02%. The component of uncertainty associated with the gain correction factor,  $k_G$ , is zero because all measurements of the GSFC sphere source were made with  $G = 1$ . For the GSFC sphere measurements at OSC, the SXR was about 1.35 m from the aperture of the sphere, and the lens focal setting was about 1.13 m. The values for the uncertainty in the spatial correction factor,  $u_a$  are given in the eighth column (Sect. 3.2.3 and Table 12).

A conservative estimate of the uncertainty in the spectral correction factor,  $u_{k_\lambda}$ , can be derived using the results presented in Table 10. The assumptions are that the relative spectral shape of the LLR source and the GSFC sphere source agree with the modified blackbody model representation, (29); and the parameter  $\alpha$  corresponds to a blackbody temperature of 2,856 K for the LLR source, and between 2,000 K and 3,200 K for the GSFC sphere source. The range of spectral calibration factors ( $k_\lambda$ ) in Table 10 was then used to derive the Type B uncertainties which are given in the ninth column. The final component of uncertainty for measurements of the GSFC sphere source with the SXR arises from the effect of the uncertainty in  $\lambda_m$  and the relative spectral shape of the GSFC sphere source. Without information on the spectral shape, the analysis presented in Sect. 4.1 cannot be performed. Instead, the results for the LLR source are used as a conservative estimate.

All nine sources of uncertainty, expressed in percent, were combined in quadrature to determine the combined standard uncertainty,  $u_c$ , for SXR measurements of the GSFC integrating sphere source in the 16 lamp configuration. Depending on the measurement channel, these relative uncertainties vary from 1.3–0.6%. These values are

representative of SXR measurements of other integrating sphere sources, since the contributions from using other values of the voltage gain are not significant.

#### 4.2.2 Known Source

The results for the SXR measurements of the GSFC sphere during the NIST calibration, using a prism-grating monochromator and a standard lamp of spectral radiance, were analyzed assuming the spectral radiance was unknown (Early and Johnson 1997). This work, therefore, was a confirmation of the SXR in the measurement mode. The spectral radiance determined using the standard lamp and the spectroradiometer in that work is used here as an example of using the SXR to verify the spectral radiance of a known source. A combination of the measurement equation, (5), and (9)–(11) results in a verification measurement equation,

$$\int L_{ms}(\lambda) \rho(\lambda) d\lambda = \frac{S_{ms}}{S_{cs}} k_G k_a \int L_{cs}(\lambda) \rho(\lambda) d\lambda, \quad (36)$$

which should be true within the combined uncertainties. Note that (36) does not require identification of a measurement wavelength. The uncertainty components associated with the measured signals, the SXR gain, and spatial correction factor were calculated as described above. The uncertainties associated with the integrals were evaluated as in Sect. 3.2.2 by approximating the integrals as sums and propagating the uncertainties as before:

$$u_{int}^2 = \sum u_{sr}^2(\lambda_i) \left( \rho(\lambda_i) (\lambda_{i+1} - \lambda_i) \right)^2 + \sum u_{\rho(\lambda)}^2 \left( L(\lambda_i) (\lambda_{i+1} - \lambda_i) \right)^2, \quad (37)$$

where  $u_{int}$  is the standard uncertainty of an integral of the form given in (36),  $u_{sr}$  is the standard uncertainty in the  $L_{ms}(\lambda)$  or  $L_{cs}(\lambda)$  values, and  $u_{\rho(\lambda)}$  is the standard uncertainty in the relative spectral response data for the SXR. As in Sect. 3.2.2, the uncertainty in the wavelength step was taken to be negligible.

For the LLR source,  $u_{int}$  was evaluated with the limits of the integral from 400–800 nm using the same modified blackbody model that was used to represent the FASCAL calibration values in Sect. 3.2.6. The standard uncertainty in the LLR spectral radiance was determined at each wavelength required for (37) using the same smoothing interpolation routine as described earlier. The result was combined in quadrature with an average estimate of the uncertainty of the blackbody fit to the FASCAL data, which was estimated to be 0.43%, independent of wavelength. For the GSFC sphere source, which was measured every 10 nm from 380–1,100 nm using the calibrated spectroradiometer (Early and Johnson 1997), a cubic spline fit was used to interpolate the spectral radiance and standard uncertainties at the wavelengths required for (36).

**Table 17.** Determination of combined standard uncertainties, expressed in units of percent, for SXR measurements of the GSFC sphere source in the 16 lamp configuration.

Channel	$u_D$	$u_{flux}$	$u_{rep}$	$u_d$	$u_{stat}$	$u_G$	$u_a$	$u_{k_\lambda}$	$u_{\lambda_m}$	$u_c$
1	0.88	0.11	0.1	0.3	0.012	0.00	0.30	0.39	0.12	1.07
2	1.12	0.11	0.1	0.3	0.011	0.00	0.36	0.32	0.09	1.27
3	0.54	0.10	0.1	0.3	0.010	0.00	0.14	0.12	0.06	0.66
4	0.63	0.09	0.1	0.3	0.007	0.00	0.09	0.06	0.04	0.72
5	0.49	0.11	0.1	0.3	0.007	0.00	0.08	0.03	0.02	0.60
6	0.64	0.09	0.1	0.3	0.005	0.00	0.06	0.02	0.01	0.72

**Table 18.** Determination of combined standard uncertainties, expressed in units of percent, for the verification mode using the SXR measurements and the NIST determination of the spectral radiance of the GSFC sphere source in the 16 lamp configuration.

Channel	LLR Source		$u_{flux}$ $u_{rep}$ $u_d$			GSFC Sphere		$u_a$ $u_c$	
	$u_{int}$	$u_{stat}$				$u_{int}$	$u_{stat}$		
1	0.12	0.28	0.11	0.1	0.3	0.110	0.012	0.30	0.55
2	0.12	0.17	0.11	0.1	0.3	0.096	0.011	0.36	0.54
3	0.11	0.35	0.10	0.1	0.3	0.083	0.010	0.14	0.52
4	0.11	0.16	0.09	0.1	0.3	0.076	0.007	0.09	0.40
5	0.10	0.15	0.11	0.1	0.3	0.066	0.007	0.08	0.40
6	0.10	0.37	0.09	0.1	0.3	0.056	0.005	0.06	0.51

The results, expressed as relative standard uncertainties, are given in Table 18.

## 5. DISCUSSION

A detailed and comprehensive description of the design, characterization, and calibration of a multichannel, portable, filter radiometer, the SXR, was given in Sects. 2 and 3. In Sect. 3, the measurement equation was separated into independent expressions relating the measured signal to the radiant flux in terms of the key parameters using the assumption that these variables are separable. These expressions were related to the measurement procedures used for the characterization of the SXR and methods were developed to use the results for correction and uncertainty estimation of measurements of radiant sources with the SXR.

The results represent a consistent analysis, and in some cases, a re-analysis of the SXR characterization and calibration data, producing revised values for  $\lambda_m$ ,  $\Delta\lambda_s$ , and  $\langle D_{cs} \rangle$  when compared to earlier publications (Mueller et al. 1994, Mueller et al. 1996, Johnson et al. 1996, Sakuma et al. 1996, Johnson et al. 1997, and Early and Johnson 1997). Compared to the original values, the revised values for  $\lambda_m$  reported here changed by about 0.3 nm for channel 1, 0.1 nm for channels 2–5, and by a negligible amount for channel 6. The calibration coefficients changed by between 0.2% and –1%, primarily because in the preliminary analysis, different parameters for the modified blackbody model of the LLR spectral radiance, as measured by FASCAL, were used—the  $\lambda^4$  fit from 350–900 nm. Because the revised results are consistent with the previous results

within the combined uncertainties, the earlier work does not need to be revised. Results, which are being prepared for publication, include three sphere measurements at two facilities for the Earth Observing System (EOS) program of calibration (Butler and Johnson 1996), measurements of diffuse plaques at SIRREX-5, and measurements of the GSFC integrating sphere at OSC during the postthermal-vacuum calibration of SeaWiFS.

In Sect. 4, the uncertainties were evaluated for two modes of operation, the measurement mode and the verification mode. In the measurement mode, the combined standard uncertainty was shown to be 0.6% and 1.3% for the GSFC sphere in the 16 lamp configuration. This meets the goals of the SeaWiFS Project. These uncertainties (Table 17) should not increase substantially for dimmer sources, which are often used in the Project. Because the SXR is linear, the uncertainty that arises from using increased gain is small, and the measurement standard deviation does not increase substantially with decreased spectral radiance. In the GSFC example, the components of uncertainty that dominate the combined uncertainty were the uncertainty in the SXR measurements of the LLR calibration source and the uncertainty in the FASCAL spectral radiance values (Sects. 3.2.6 and 4.1, Tables 15–16, and Figs. 23–24); the long-term drift of the overall responsivity of the SXR (Sect. 3.2.5); and, at the shorter measurement wavelengths, uncertainties associated with corrections relating to the size and relative spectral shape of the test source and the uncertainty in the value of  $\lambda_m$ .

In the verification mode, the combined standard uncertainty for the same example was reduced to between 0.4%



and 0.6%. The uncertainties in the spectral radiance of the sources, and the interpolation of these values, are components of the uncertainties in the integral of the spectral radiance and the relative spectral response of the SXR. There are no components associated with  $\lambda_m$ .

For either method, obvious areas of improvement include:

- 1) Eliminating the non-uniform field-of-view response of the SXR which is caused by vignetting (this requires a new optical and mechanical design);
- 2) Improving the point-spread response of the SXR or the characterization procedure to reduce the uncertainties associated with this correction;
- 3) Improving the methods used to measure the relative spectral response by developing monochromatic sources with increased radiance;
- 4) Increasing the stability of the LLR source, particularly in the blue spectral region; and
- 5) Adding calibration values of the spectral radiance of the LLR source at selected wavelengths to reduce the effects associated with interpolation in these values.

## 6. CONCLUSIONS

The SXR was built for the SeaWiFS Project by NIST to establish traceability from the primary NIST facility, FASCAL, to standards of spectral radiance—integrating sphere sources and diffuse plaques illuminated by standard irradiance lamps. The critical requirements were stability, accuracy, portability, and compatibility with the SeaWiFS measurement requirements. Results with the SXR, over four years of operation, demonstrate that the instrument has fully satisfied these requirements. Satisfactory results, however, would not be possible without detailed, thorough, and accurate characterization and calibration of the radiometer. A consistent theme emphasized in this work is the interdependence of sources and radiometers—the radiometric properties of the sources used to calibrate a radiometer, such as the SXR, must be characterized to ensure they are commensurate with the underlying assumptions in the measurement equation (temporal stability, polarization, spatial and angular uniformity, spectral characteristics, magnitude of flux, and aperture size). Otherwise, the results will be limited by these source properties.

At the SIRREX activities, the SXR was used to measure integrating sphere sources and illuminated plaques, quantifying these radiance values and providing the opportunity to compare spectral radiance sources using standard irradiance lamps as the calibration source. This was a key requirement in the SeaWiFS Calibration and Validation Program (McClain et al. 1992), and the SXR was used to investigate the accuracy of integrating sphere sources calibrated by Optronic Laboratories, Inc.; Biospherical Instruments, Inc.; Gamma Scientific; Labsphere, Inc.; and

GSFC. Also at the SIRREXs, the SXR helped to identify problems with radiance sources—such as temporal drift, spatial and angular nonuniformity in integrating sphere sources, and issues related to bidirectional reflectance and scattered flux for the illuminated plaque.

On several occasions other than the SIRREXs, the SXR was used to measure the GSFC integrating sphere. Studies of the spatial uniformity led to the recommendation that the sphere be recoated before further use (Mueller et al. 1994). During the NIST calibration of the sphere, simultaneous measurements with the SXR and the NIST prism-grating spectroradiometer (Early and Johnson 1997), provided a means to track the performance of the sphere, both at SIRREX-4 and nearly two years later during the postthermal-vacuum calibration of the SeaWiFS instrument. The coating had aged, causing the radiance to decrease by as much as 6% at 411 nm, but because the SXR was stable, it was possible to use the sphere with SeaWiFS without repeating the lengthy and difficult calibration procedures.

The SXR was used twice at the field calibration site for the Marine Optical Buoy (MOBY) program in Honolulu, establishing the utility of portable instruments, such as the SXR. The SXR was used to measure the MOBY radiance calibration devices, integrating sphere sources from Optronic Laboratories and Gamma Scientific, once in February 1994 (Mueller et al. 1996) and again in September 1996. The SXR was used at the MOBY site in 1994 and at SIRREX-3 to verify the performance of a new calibration source from Gamma Scientific; this work resulted in modifications to the system (Mueller et al. 1996).

In February 1995, the SXR was used at NEC Corporation in Yokohama, Japan, to measure the spectral radiance of the integrating sphere used to calibrate the visible and near-infrared radiometer for the EOS Advanced Spaceborne Thermal Emission and Reflection radiometer (ASTER) (Sakuma et al. 1996). During the same experiment, the sphere source that was used to calibrate the Ocean Color Temperature Scanner (OCTS) was measured (Johnson et al. 1997). Both sphere sources were calibrated by NEC Corporation using a double-grating monochromator and a variable temperature blackbody; a blackbody at the freezing point of copper was the primary standard. The participants included calibration experts from the University of Arizona, GSFC, and the National Research Laboratory of Metrology in Tsukuba, Japan. Consequently, these sphere measurements were a verification of radiance scales which were directly traceable to a fixed-point blackbody from a different national standards laboratory, as well as an intercomparison of four types of portable radiometers. In both cases, the agreement with NEC and the participants was within the combined measurement uncertainties.

In August 1996, the SXR was used at Hughes Santa Barbara Remote Sensing (SBRS) to measure the integrating spheres used for the Moderate Resolution Imaging

Spectroradiometer (MODIS) and the Land Satellite (Landsat) with the same group of participants that were at NEC Corporation in 1995, with the addition of a short-wave infrared radiometer from the University of Arizona and two versions of a second generation SXR. The Visible Transfer Radiometer (VXR) was built for the EOS Project and the Landsat Transfer Radiometer (LXR), was built for the Landsat calibration program (B. Markham, pers. comm.). The preliminary results (Butler and Johnson 1996) appear satisfactory, and the final results are in preparation. Immediately after this experiment, the group of participants traveled to the Jet Propulsion Laboratory and measured the integrating sphere in the Multiangle Imaging Spectroradiometer (MISR) program. ASTER, MODIS, and MISR are scheduled for launch on the EOS AM-1 platform, along with two other instruments.

Finally, during development of the SeaWiFS Quality Monitor (SQM) as a portable field source (Johnson et al. 1998), the SXR was used to map the spatial uniformity of this type of field source. Future use of the SXR could include periodic recalibration at NIST, studies of the SQM, and measurements at other institutions involved in ocean color measurements.

Improvements and recommendations to the SXR include an improved mechanical housing (i.e., the addition of a handle for ease of use), the reduction or elimination of the vignetting, and improvements to the point-spread response. Because the SXR can be used to establish a detector-based scale of spectral radiance, it would be useful to have additional measurement channels so that a suitable interpolation model could be developed. The success of the SXR led to the development of the VXR for the EOS program, and the LXR for Landsat. The VXR has the same measurement wavelengths as the SXR, except that a channel at 870 nm was substituted for the one at 441 nm. Four channels in the LXR correspond to the Landsat filters, and the other two were selected from the SXR channels. For both instruments, an improved mechanical package was implemented, and the field-of-view response is more uniform, but for the VXR, problems remain with the point-spread response for channels at 775 nm and 870 nm. Substituting a custom reflective or refractive objective lens for the commercial camera lens is probably the best solution to this problem. Finally, it would be difficult to add more than six channels to an SXR-like design, and future spectroradiometers for the EOS program may use gratings instead of interference filters.

#### ACKNOWLEDGMENTS

The SXR project would not have been successful without the contribution of many individuals. Tom Gentile assisted with the point-spread response measurements and preliminary analysis of these data. Sally Bruce performed the linearity measurements and reduction of these data, and she and Tom Larson assisted with the relative spectral response measurements. Yvonne Barnes provided the pressed PTFE plaque. Ben Tsai

and Mark Levenson provided insight into the uncertainty analysis. Todd Westphal, Stan Hooker, and Jim Brown provided the SXR LabVIEW data acquisition program. NIST was supported in part with funding from the SeaWiFS Project Office, through Interagency Agreement Number S-64-96-E.

#### APPENDICES

##### Appendix A

##### *Parts Used in the Amplifier and Control Circuit*

The parts used in the amplifier and control circuit are given in Table A1.

#### GLOSSARY

AC	Alternating Current
AMT-5	The Fifth Atlantic Meridional Transect
ASTER	Advanced Spaceborne Thermal Emission and Reflection Radiometer
ASTM	American Society for Testing and Materials
ATA	Ambient Temperature Plate Assembly
BCD	Binary Coded Decimal
BNC	Bayonet Nut Connector
BPA	Back Plate Assembly
C-mount	Not an acronym, but a mounting system for camera lenses.
CT	Cylindrical Tube
DC	Direct Current
DIO	Digital Input-Output
DMM	Digital Multimeter
DPA	Detector Plate Assembly
E	East
EOS	Earth Observing System
EP	Entrance Pupil
FASCAL	Facility for Automated Spectroradiometric Calibrations
FET	Field-Effect Transistor
F-mount	Not an acronym, but a mounting system for camera lenses.
FS	Field Stop
GPIB	General Purpose Interface Bus
GSFC	Goddard Space Flight Center
HACR	High-Accuracy Cryogenic Radiometer
HP	Hewlett-Packard
IAD	Ion-Assisted Beam Deposition
IC	Integrated Circuit
ID	Inside Diameter
IEEE	Institute of Electrical and Electronic Engineers
IF	Interference Filter
ILX	Not an acronym.
Landsat	Land Satellite
LLR	Low Level Radiance
LSB	Least Significant Bit
LXR	LANDSAT Transfer Radiometer
MISR	Multiangle Imaging Spectroradiometer
MOBY	Marine Optical Buoy
MODIS	Moderate Resolution Imaging Spectroradiometer
MMA	Mirror Mount Assembly
MSB	Most Significant Bit

**Table A1.** The parts used in the circuit diagram for the amplifier and control circuit in the SXR (in Fig. 9)

Part Label Number	Part Description
A1–A6	Burr Brown OPA138LM operational amplifier
A7	Precision Monolithics Inc. OP27EJ operational amplifier
RY1–RY10	Gordos reed relays 4705D
C1 and C2	Philips 10 pF capacitor C40C100JNP
C3–C5	Philips 100 pF capacitor C40C101JNP
C6	Philips 1,000 pF capacitor C40C102JNP
C7–C11	Kemet 0.1 $\mu$ F ceramic 50 V DC capacitor C322C104K5R5CA
C12	Kemet 4.7 $\mu$ F tantalum 35 V DC capacitor T352E475K035AS
D1–D5	Hamamatsu Photonics silicon photodiode S1227-66BQ
D6	Hamamatsu Photonics silicon photodiode S1337-66BQ
D7 and D8	Diode 1N914
PN1–PN12	Samtech photodiode socket pin SC-1P1-GG (not shown)
PS1	MultiProducts $\pm 15$ V DC 290 mA and +5 V DC 750 mA 30 W power supply T515750/1 (not shown)
R1 and R2	Victoreen 1,000 M $\Omega$ 0.5% resistor 400-23
R3–R5	Victoreen 100 M $\Omega$ 0.5% resistor 400-23
R6	Victoreen 10 M $\Omega$ 0.5% resistor 400-23
R7–R9	1 k $\Omega$ 0.1% resistor
R10	10 k $\Omega$ 0.1% resistor
R11	100 k $\Omega$ 0.1% resistor
R12	1 M $\Omega$ 0.1% resistor
R13	3.3 k $\Omega$ resistor
RT1–RT7	Bourns trimpot resistor 3266W (not shown)
RN1 and RN2	Dale “pull-up” resistor network 4.7 k $\Omega$ CSC-06A-01
SO1	9-pin Amphenol connector DE9S-F179
SO2	Amphenol BNC-type connector 31-10
SO3	Power supply connector WMPLMB (not shown)
SO4	Cable (not a connector) for the ILX 5910B (not shown)
SW1	Alco rotary switch MRJE-26
SW2	Alco rotary switch MRJE-34
SW3	Alco toggle switch single pole double throw (SPDT) MTA-106D-PC
U1 and U4	Texas Instruments IC demultiplexer SN74HC137N
U2 and U6	IC inverter and buffer SN74LS04N
U3 and U5	IC buffer/driver SN7407

## N North

NASA National Aeronautics and Space Administration  
 NEC Not an acronym, but the present name for the Nippon Electric Company (Japan)  
 NIST National Institute of Standards and Technology

OCTS Ocean Color Temperature Scanner  
 OD Outside Diameter  
 OSC Orbital Sciences Corporation

PC Personal Computer  
 PID Proportional, Integral, Differential  
 PTFE Polytetrafluoroethylene

RE Ramsden Eyepiece  
 RL Relay Lens  
 RTV Room Temperature Vulcanizing

## S South

SBRs Santa Barbara Remote Sensing  
 SeaWiFS Sea-viewing Wide Field-of-view Sensor  
 SIMBIOS Sensor Intercomparison and Merger for Biological and Interdisciplinary Ocean Studies  
 SIRREX SeaWiFS Intercalibration Round-Robin Experiment  
 SIRREX-1 The First SIRREX (July 1992)  
 SIRREX-2 The Second SIRREX (June 1993)  
 SIRREX-3 The Third SIRREX (September 1994)  
 SIRREX-4 The Fourth SIRREX (May 1995)  
 SIRREX-5 The Fifth SIRREX (July 1996)  
 SQM SeaWiFS Quality Monitor  
 SXR SeaWiFS Transfer Radiometer

TEC Thermoelectric Cooler  
 TTL Transistor–Transistor Logic

UNC Unified Course

VisSCF Visible Spectral Comparator Facility (NIST)

VXR Visible Transfer Radiometer

W West

WM Spherical Mirror Wedge Section

# SYMBOLS

$A$  Source area.

$A_{cs}$  Calibration source area.

$A_{max}$  Maximum source area based on point-spread response measurements.

$A_{ms}$  Measured source area.

$b$  Background signal.

$\langle b \rangle$  Average background signal.

$b_G$  Background signal on gain  $G$ .

$b_G^j$  Background signal on gain  $G$  for the  $j$ th set of SXR data.

$b_-$  Lower limit for the background.

$b_+$  Upper limit for the background.

$c_0, c_1, c_2, c_3, c_4$  Polynomial coefficients in a modified blackbody model of spectral radiance.

$C_1, C_2, C_3$  Thermistor parameters.

$C_F$  Damping capacitor.

$d$  Lens focal setting.

$d'$  Lens focal setting.

$\langle D \rangle$  Average spectral radiance calibration factor.

$\langle D_{cs} \rangle$  Average spectral radiance calibration factor for a calibration source.

$\langle D_{ms} \rangle$  Average spectral radiance calibration factor for a measured source.

$D(x, y, \theta, \phi, \lambda)$  Spectral-ray flux responsivity function.

$e$  Base of the natural logarithms.

$f$  F-stop.

$fl$  Focal length of lens.

$G$  Gain of voltage amplifier.

$G_{cs}$  Gain of voltage amplifier during SXR calibration.

$G_{ms}$  Gain of voltage amplifier during SXR measurements.

$h(x, y)$  Relative spatial response function.

$I$  Filter designation.

$j$  An iteration factor.

$J$  Filter designation.

$k$  Calibration correction factor.

$k(\lambda_m)$  Calibration correction factor for calibration and measured sources.

$k_a$  Spatial calibration correction factor.

$k_G$  Gain calibration correction factor.

$k_\lambda$  Spectral calibration correction factor.

$K$  Filter designation.

$l(x, y, \theta, \phi)$  Relative spatial and angular distribution function.

$L(x, y, \theta, \phi, \lambda)$  Spectral radiance as a function of measurement geometry.

$L(\lambda)$  Spectral radiance.

$L_{cs}(\lambda)$  Spectral radiance of the calibration source.

$L_{ms}(\lambda)$  Spectral radiance of the measured source.

$n$  Integer.

$N$  Number of samples.

$N_G$  Number of samples on gain  $G$ .

$p_0, p_1, p_2$  Polynomial coefficients for normalized sums.

$P$  Step size in point-spread response measurements.

$r$  Radial coordinate.

$r_{cs}$  Radius of the calibration source area.

$r_{I,J,K}$  Normalized residuals of linearity response.

$r_{max}$  One-half of the width or height of the area used to normalize the point spread response measurement.

$r_{ms}$  Radius of the measured source area.

$r_0, r_2, r_3$  Polynomial coefficients for linearity response.

$R(\lambda)$  Absolute spectral responsivity function.

$R_F$  Resistance of feedback resistor.

$R_{IB}$  In-band spectral responsivity.

$R_{Tot}$  Total spectral responsivity.

$\mathcal{R}$  Thermistor resistance.

$S$  Net signal.

$S_{cs}$  Net signal for the calibration source.

$S_G^j$  Net signal on gain  $G$  for the  $j$ th reading of the DMM.

$S_{I,J,K}$  Net signal using the Beamcon III for the filter combination denoted I, J, K.

$S_{ms}$  Net signal for the measured source.

$T$  DPA temperature.

$u$  Relative standard uncertainty.

$u(L, \lambda)$  Relative standard uncertainty caused by uncertainty in  $\lambda_m$ .

$u_a$  Standard uncertainty in  $k_a$ .

$u_c$  Combined relative standard uncertainty.

$u_d$  Relative standard uncertainty caused by temporal drift.

$u_D$  Relative standard uncertainty in  $\langle D_{cs} \rangle$ .

$u_{Fit}$  Relative standard uncertainty associated with interpolation in  $L(\lambda)$ .

$u_{flux}$  Relative standard uncertainty from SXR nonlinearity.

$u_G$  Relative standard uncertainty in  $k_G$ .

$u_{int}$  Relative standard uncertainty of an integral.

$u_{k_\lambda}$  Relative standard uncertainty in the spectral calibration correction factor.

$u_{LLR}$  Relative standard uncertainty in the spectral radiance of the LLR source.

$u'_{LLR}$  Relative standard uncertainty using a smoothing curve fit procedure.

$u_{rep}$  Relative standard uncertainty associated with the repeatability of the SXR.

$u_{st}$  Relative standard uncertainty in the sphere radiance.

$u_{stat}$  Relative standard uncertainty from measurement statistics.

$u_\lambda$  Relative standard uncertainty in VisSCF wavelength calibration.

$u_{\lambda_m}$  Standard uncertainty in  $\lambda_m$ .

$u_{\rho(\lambda)}$  Standard uncertainty in  $\rho(\lambda)$ .

$v$  Total signal.

$v_G^j$  Total signal on gain  $G$  for the  $j$ th reading of the DMM.

$x$  Horizontal spatial coordinate.

$x_{m1}$  Measured horizontal spatial coordinate.

$y$  Vertical spatial coordinate.

$y_{m1}$  Measured vertical spatial coordinate.

- $\alpha$  Parameter in modified blackbody model of spectral radiance.
- $\beta$  Parameter in modified blackbody model of spectral radiance.
- $\delta(x - x_m)$  Dirac delta-function for the variable  $x$ .
- $\delta(y - y_m)$  Dirac delta-function for the variable  $y$ .
- $\delta\lambda$  Wavelength shift of spectral responsivity.
- $\delta(\lambda - \lambda_m)$  Dirac delta-function for the variable  $\lambda$ .
- $\delta(\theta - \theta_m)$  Dirac delta-function for the variable  $\theta$ .
- $\delta(\phi - \phi_m)$  Dirac delta-function for the variable  $\phi$ .
- $\Delta\lambda_g$  Bandwidth of SXR channel assuming a Gaussian band shape.
- $\Delta\lambda_s$  Bandwidth of SXR channel assuming a square band shape.
- $\eta(\theta, \phi)$  Relative angular response function.
- $\theta$  Polar angular coordinate.
- $\theta_m$  Measured polar angular coordinate.
- $\lambda$  Wavelength (continuous variable).
- $\lambda_i$  Wavelength (discrete variable).
- $\lambda_m$  Measurement wavelength of one SXR channel.
- $\lambda_{\max}$  Maximum wavelength for  $\rho(\lambda)$  measurements at the VisSCF.
- $\lambda_{\min}$  Minimum wavelength for  $\rho(\lambda)$  measurements at the VisSCF.
- $\Xi(\Phi(\lambda))$  Nonlinear function relating flux to signal.
- $\rho(\lambda)$  Relative spectral response function.
- $\rho(\lambda)_{dv}$   $\rho(\lambda)$  measured with the field of view underfilled.
- $\rho(\lambda)_{PTFE}$   $\rho(\lambda)$  measured using a diffuse plaque.
- $\sigma^2$  Statistical variance.
- $\Upsilon$  Nonlinear function.
- $\Upsilon(S)$  Nonlinear function relating signal to flux.
- $\phi$  Azimuthal angular coordinate.
- $\phi_m$  Measured azimuthal angular coordinate.
- $\Phi(\lambda)$  Radiant flux per unit wavelength.
- $\Phi_{EW}$  Diameter of an entrance window.
- $\Phi'_{EW}$  Diameter of an entrance window.
- $\Phi_{I,J,K}$  Flux for the Beamcon III for the filter combination denoted I, J, K.
- $\Phi'_{I,J,K}$  Normalized flux for the Beamcon III for the filter combination denoted I, J, and K.
- $\chi^2$  Normalized sum of the square of the differences between a model for a set of values and the measured values.
- $\psi$  Detector responsivity constant.
- $\omega$  Solid angle.
- ASTM, 1997: "E1256—95, standard test methods for radiation thermometers (single waveband type)." Temperature Measurement, Vol. 14.03, Sect. 14, General Methods and Instrumentation, *Annual Book of ASTM Standards*, Amer. Soc. Testing and Materials, Philadelphia, Pennsylvania, 437–443.
- Barnes, R.A., A.W. Holmes, W.L. Barnes, W.E. Esaias, C.R. McClain, and T. Svitek, 1994: SeaWiFS Prelaunch Radiometric Calibration and Spectral Characterization. *NASA Tech. Memo. 104566*, Vol. 29, S.B. Hooker and E.R. Firestone, Eds., NASA Goddard Space Flight Center, Greenbelt, Maryland, 55 pp.
- Butler, J.J., and B.C. Johnson, 1996: EOS radiometric measurement comparisons at Hughes Santa Barbara Remote Sensing and NASA's Jet Propulsion Laboratory. *The Earth Observer*, 8(5), 17–19.
- Early, E.A., and B.C. Johnson, 1997: "Calibration and characterization of the GSFC Sphere." In: Yeh, E.-n., R.A. Barnes, M. Darzi, L. Kumar, E.A. Early, B.C. Johnson, and J.L. Mueller, 1997: Case Studies for SeaWiFS Calibration and Validation, Part 4. *NASA Tech. Memo. 104566*, Vol. 41, S.B. Hooker and E.R. Firestone, Eds., NASA Goddard Space Flight Center, Greenbelt, Maryland, 3–17.
- Eppeldauer, G., 1991: Temperature monitored/controlled silicon photodiodes for standardization. *SPIE*, 1479, 71–77.
- , and J.E. Hardis, 1991: Fourteen decade photocurrent measurements with large area silicon photodiodes at room temperature. *Appl. Opt.*, 30, 3,091–3,099.
- Fowler, J.B., 1977: The electronic aspects of the NBS detector response and intercomparison package and laser stabilization facility. *Electro-Optics/Laser 77 Conference and Exposition*, Industrial and Scientific Conference Management, Chicago, Illinois, 689–695.
- Gentile, T.R., and J.M. Houston, J.E. Hardis, C.L. Cromer, and A.C. Parr, 1996: National Institute of Standards and Technology High-accuracy Cryogenic Radiometer. *Appl. Opt.*, 35, 1,056–1,068.
- Graeme, J.G., 1995: *Photodiode Amplifiers: Operational Amplifier Solutions*, McGraw-Hill, New York, 252 pp.
- Hooker, S.B., C.R. McClain, and A. Holmes, 1993: Ocean color imaging: CZCS to SeaWiFS. *Mar. Tech. Soc. J.*, 27, 3–15.
- , T.L. Westphal, and Y. Ge, 1994: "The SIRREX database." In: Hooker, S.B., C.R. McClain, J.K. Firestone, T.L. Westphal, E. Yeh, and Y. Ge, 1994: The SeaWiFS Bio-Optical Archive and Storage System (SeaBASS), Part 1. *NASA Tech. Memo. 104566*, Vol. 20, S.B. Hooker and E.R. Firestone, Eds., NASA Goddard Space Flight Center, Greenbelt, Maryland, 23–30.
- Johnson, B.C., S.S. Bruce, E.A. Early, J.M. Houston, T.R. O'Brian, A. Thompson, S.B. Hooker, and J.L. Mueller, 1996: The Fourth SeaWiFS Intercalibration Round-Robin Experiment, SIRREX-4, May 1995. *NASA Tech. Memo. 104566*, Vol. 37, S.B. Hooker and E.R. Firestone, Eds., NASA Goddard Space Flight Center, Greenbelt, Maryland, 66 pp.

- , F. Sakuma, J.J. Butler, S.F. Biggar, J.W. Cooper, J. Ishida, and K. Suzuki, 1997: Radiometric measurement comparison using the Ocean Color Temperature Scanner (OCTS) visible and near infrared integrating sphere. *J. Res. NIST*, **102**, 627–646.
- , P.-S. Shaw, S.B. Hooker, and D. Lynch, 1998: Radiometric and engineering performance of the SeaWiFS Quality Monitor (SQM): A portable light source for field radiometers. *J. Atmos. Oceanic Tech.*, **15**, 1,008–1,022.
- Kostkowski, H.J., and F.E. Nicodemus, 1978: "An introduction to the measurement equation." In: F.E. Nicodemus, Ed., 1978: Self-Study Manual on Optical Radiation Measurements, Part 1–Concepts, *NBS Tech. Note 910-2*, U.S. Department of Commerce, National Institute of Standards and Technology, Washington, DC, 58–104.
- Larason, T.C., S.B. Bruce, and C.L. Cromer, 1996: The NIST high accuracy scale for absolute spectral response from 406 nm to 920 nm. *J. Res. NIST*, **101**, 133–140.
- McClain, C.R., W.E. Esaias, W. Barnes, B. Guenther, D. Endres, S.B. Hooker, B.G. Mitchell, and R. Barnes, 1992: SeaWiFS Calibration and Validation Plan. *NASA Tech. Memo. 104566, Vol. 3*, S.B. Hooker and E.R. Firestone, Eds., NASA Goddard Space Flight Center, Greenbelt, Maryland, 41 pp.
- Mueller, J.L., 1993: The First SeaWiFS Intercalibration Round-Robin Experiment, SIRREX-1, July 1992. *NASA Tech. Memo. 104566, Vol. 14*, S.B. Hooker and E.R. Firestone, Eds., NASA Goddard Space Flight Center, Greenbelt, Maryland, 60 pp.
- , and R.W. Austin, 1992: Ocean Optics Protocols. *NASA Tech. Memo. 104566, Vol. 5*, S.B. Hooker and E.R. Firestone, Eds., NASA Goddard Space Flight Center, Greenbelt, Maryland, 43 pp.
- , B.C. Johnson, C.L. Cromer, J.W. Cooper, J.T. McLean, S.B. Hooker, and T.L. Westphal, 1994: The Second SeaWiFS Intercalibration Round-Robin Experiment, SIRREX-2, June 1993. *NASA Tech. Memo. 104566, Vol. 16*, S.B. Hooker and E.R. Firestone, Eds., NASA Goddard Space Flight Center, Greenbelt, Maryland, 121 pp.
- , and R.W. Austin, 1995: Ocean Optics Protocols for SeaWiFS Validation, Revision 1. *NASA Tech. Memo. 104566, Vol. 25*, S.B. Hooker, E.R. Firestone, and J.G. Acker, Eds., NASA Goddard Space Flight Center, Greenbelt, Maryland, 67 pp.
- , B.C. Johnson, C.L. Cromer, S.B. Hooker, J.T. McLean, and S. Biggar, 1996: The Third SeaWiFS Intercalibration Round-Robin Experiment, SIRREX-3, September 1994. *NASA Tech. Memo. 104566, Vol. 34*, S.B. Hooker, E.R. Firestone, and J.G. Acker, Eds., NASA Goddard Space Flight Center, Greenbelt, Maryland, 78 pp.
- Nicodemus, F.E., 1978: "More on the distribution of optical radiation with respect to position and direction." In: F.E. Nicodemus, Ed., 1978: Self-Study Manual on Optical Radiation Measurements, Part 1–Concepts, *NBS Tech. Note 910-2*, U.S. Department of Commerce, National Institute of Standards and Technology, Washington, DC, 1–57.
- O'Shea, D.C., 1985: *Elements of Modern Optical Design*, John Wiley and Sons, New York, 402 pp.
- Sakuma, F., B.C. Johnson, S.F. Biggar, J.J. Butler, J.W. Cooper, M. Hiramatsu, and K. Suzuki, 1996: EOS AM-1 pre-flight radiometric measurement comparison using the Advanced Spaceborne Thermal Emission and Reflection radiometer (ASTER) visible/near-infrared integrating sphere. *SPIE*, **2820**, 184–196.
- Saunders, R.D., and J.B. Shumaker, 1984: Automated radiometric linearity tester. *Appl. Opt.*, **23**, 3,504–3,506.
- Stout, D.F., 1976: *Handbook of Operational Amplifier Design*, M. Kaufman, Ed., McGraw-Hill, New York, 317 pp.
- Taylor, B.N., and C.E. Kuyatt, 1994: Guidelines for Evaluating and Expressing the Uncertainty of NIST Measurement Results. *NIST Tech. Note 1297*, U.S. Department of Commerce, National Institute of Standards and Technology, Washington, DC, 20 pp.
- Thompson, A., and H.-M. Chen, 1994: Beamcon III, a linearity measurement instrument for optical detectors. *J. Res. NIST*, **99**, 751–755.
- Walker, J.H., R.D. Saunders, and A.T. Hattenburg, 1987a: Spectral Radiance Calibrations. *NBS Special Publication 250-1*, U.S. Department of Commerce, National Institute of Standards and Technology, Washington, DC, 68 pp.
- , R.D. Saunders, J.K. Jackson, and D.A. McSparron, 1987b: Spectral Irradiance Calibrations. *NBS Special Publication 250-20*, U.S. Department of Commerce, National Institute of Standards and Technology, Washington, DC, 37 pp., plus Appendices.
- , and A. Thompson, 1994: Improved automated current control for standard lamps. *J. Res. NIST*, **99**, 255–261.
- Wyatt, C.L., 1978: *Radiometric Calibration: Theory and Methods*, Academic Press, New York, 200 pp.
- , 1987: *Radiometric System Design*, Macmillan Publishing Company, New York, 315 pp.
- Yeh, E.-n., R.A. Barnes, M. Darzi, L. Kumar, E.A. Early, B.C. Johnson, J.L. Mueller, and C.C. Trees, 1997: Case Studies for SeaWiFS Calibration and Validation, Part 4. *NASA Tech. Memo. 104566, Vol. 41*, S.B. Hooker and E.R. Firestone, Eds., NASA Goddard Space Flight Center, Greenbelt, Maryland, 35 pp.

## THE SEAWIFS POSTLAUNCH TECHNICAL REPORT SERIES

### Vol. 1

Johnson, B.C., J.B. Fowler, and C.L. Cromer, 1998: The SeaWiFS Transfer Radiometer (SXR). *NASA Tech. Memo. 1998-206892, Vol. 1*, S.B. Hooker and E.R. Firestone, Eds., NASA Goddard Space Flight Center, Greenbelt, Maryland, 58 pp.

**REPORT DOCUMENTATION PAGE**

Form Approved

OMB No. 0704-0188

Public reporting burden for this collection of information is estimated to average 1 hour per response, including the time for reviewing instructions, searching existing data sources, gathering and maintaining the data needed, and completing and reviewing the collection of information. Send comments regarding this burden estimate or any other aspect of this collection of information, including suggestions for reducing this burden, to Washington Headquarters Services, Directorate for Information Operations and Reports, 1215 Jefferson Davis Highway, Suite 1204, Arlington, VA 22202-4302, and to the Office of Management and Budget, Paperwork Reduction Project (0704-0188), Washington, DC 20503.

<b>1. AGENCY USE ONLY (Leave blank)</b>		<b>2. REPORT DATE</b> September 1998	<b>3. REPORT TYPE AND DATES COVERED</b> Technical Memorandum	
<b>4. TITLE AND SUBTITLE</b> SeaWiFS Postlaunch Technical Report Series Volume 1: The SeaWiFS Transfer Radiometer (SXR)			<b>5. FUNDING NUMBERS</b>  Code 970.2	
<b>6. AUTHOR(S)</b> B. Carol Johnson, J.B. Fowler, and Christopher L. Cromer  Series Editors: Stanford B. Hooker and Elaine R. Firestone				
<b>7. PERFORMING ORGANIZATION NAME(S) AND ADDRESS (ES)</b>  Laboratory for Hydrospheric Processes Goddard Space Flight Center Greenbelt, Maryland 20771			<b>8. PERFORMING ORGANIZATION REPORT NUMBER</b>  98B00075	
<b>9. SPONSORING / MONITORING AGENCY NAME(S) AND ADDRESS (ES)</b>  National Aeronautics and Space Administration Washington, DC 20546-0001			<b>10. SPONSORING / MONITORING AGENCY REPORT NUMBER</b>  TM—1998—206892, Vol. 1	
<b>11. SUPPLEMENTARY NOTES</b>  E.R. Firestone: SAIC General Sciences Corporation, Laurel, Maryland; B.C. Johnson and J.B. Fowler: National Institute of Standards and Technology, Gaithersburg, Maryland; and C.L. Cromer: National Institute of Standards and Technology, Boulder, Colorado				
<b>12a. DISTRIBUTION / AVAILABILITY STATEMENT</b>  Unclassified—Unlimited Subject Category: 48 Report available from the NASA Center for AeroSpace Information, 7121 Standard Drive, Hanover, MD 21076-1320. (301) 621-0390.			<b>12b. DISTRIBUTION CODE</b>	
<b>13. ABSTRACT (Maximum 200 words)</b> <p>The SeaWiFS Transfer Radiometer (SXR) was built for the Sea-viewing Wide Field-of-view Sensor (SeaWiFS) Project as part of an Interagency Agreement with the National Aeronautics and Space Administration (NASA). The SXR is a multichannel radiometer designed to verify and compare measurements of spectral radiance at six discrete wavelengths in the visible and near infrared for various calibration sources in the SeaWiFS Project. In addition, the SXR is used to compare these sources to standards of spectral radiance maintained at the National Institute of Standards and Technology (NIST). The SXR was designed, built, and thoroughly characterized in the Optical Technology Division at NIST. A unique optical design provides six independent optical paths, each equipped with a temperature stabilized interference filter and silicon photodiode. A separate beam path through the input lens is used to visually align the SXR. The entrance windows for each channel overlap at the source, with each channel sampling a unique solid angle within the field of view of the SXR; this allows for simultaneous sampling of all channels. The combined standard relative uncertainty of spectral radiance measurements with the SXR is estimated to be between 0.6% and 1.3%. This report describes the design and construction of the SXR in detail, and gives the results of the optical characterization and calibrations done at NIST. The SXR has been used for several intercomparisons which include several SeaWiFS Intercalibration Round-Robin Experiments (SIRREXs); those done at the Marine Optical Buoy (MOBY) laboratories in Honolulu, Hawaii; at the NEC Corporation in Yokohama, Japan; and Orbital Sciences Corporation (OSC) in Germantown, Maryland. Thorough optical characterization and calibration of the SXR was essential to the successful application of the radiometer for these measurements.</p>				
<b>14. SUBJECT TERMS</b>  SeaWiFS, Oceanography, SXR, Transfer Radiometer, Detector-based Radiometry, Integrating Sphere Sources, Interference Filter, Radiometer, SIRREX,			<b>15. NUMBER OF PAGES</b> 58	
			<b>16. PRICE CODE</b>	
<b>17. SECURITY CLASSIFICATION OF REPORT</b> Unclassified	<b>18. SECURITY CLASSIFICATION OF THIS PAGE</b> Unclassified	<b>19. SECURITY CLASSIFICATION OF ABSTRACT</b> Unclassified	<b>20. LIMITATION OF ABSTRACT</b> UL	

